Scuola Internazionale Superiore di Studi Avanzati - Trieste

Condensed Matter Sector

Seeing Colors with TDDFT

Theoretical modeling of the optical properties of natural dyes

Thesis submitted for the degree of Doctor Philosophiæ

CANDIDATE
Xiao-Chuan Ge

SUPERVISORS
Prof. Stefano Baroni
Dr. Arrigo Calzolari

November 2013

SISSA - Via Bonomea 265 - 34136 TRIESTE - ITALY

非淡泊无以明志，非宁静无以致远。

—— 诸葛亮 《诫子书》

Acknowledgments

First I would like to thank my supervisors Prof. Stefano Baroni and Dr. Arrigo Calzolari for their constant guidance, encouragement and continuous support through the years of my study at SISSA. Prof. Baroni has introduced me the theoretical background of this thesis, and he has inspired me with wonderful ideas in the algorithm development. He has helped me to keep in touch with the international research community by supporting me participating conferences and schools. He has also provided me abundant computer resource, making it possible to perform the large amount of numerical simulation in this thesis. His influence on me is not only limited to the field of physics, but also the way to think, the way to write scientific article, and the way to express ideas to others. My second supervisor Dr. Calzolari has brought me to the research of anthocyanins, and also worked together step-by-step in realizing many details in the study. He has taught me how to organize the huge volume of data which has benefited me a lot during these years, and will still be an important skill in my future career.

I also would like to address my sincere gratitude to my co-workers: Simon Binnie, for his advice in the programming work, Alessadro Biancardi, for his cooperation and discussion in the chemistry-related study, and Iurii Timrov, who has read my thesis and given me many suggestions for the refinement. It has been a real pleasure to work together with them. I would like to give my appreciation to Prof. Ralph Gebauer, Prof. Stefano de Gironcoli, Prof. Andrea Dal Corso, Dr. Carlo Cavazzoni, and Dr. Fabio Affinito for their varied assistance. The work of this thesis would not have been possible without their help.

The time I spent in SISSA and in Trieste would not have been so lovely and unforgettable without my dear friends here. It was rather difficult to start living in a country where the people, the language, the food, and the culture are all distinct from where I had come from, but their support and friendship have accompanied me through all these years, turning the difficulties and loneliness into laughs, happiness and wonderful memories.

I have a very special thanks to my girlfriend. It has been the most beau-

tiful thing to meet, know and stay together with her. She has been standing by my side to support my research all the time, cheering me up when I am sad, encouraging me when I am desperate, and showing me appreciation for my every tiny success. She has used her patience, tenderness, understanding, and the fascinating smile to help me pass through all the ups and downs of my research. She has shared me her laughs and tears, as well as dreams and loves, and most importantly, she has shared her heart with me. This special thanks also extends to her family, who have been treating me like a family member.

Finally, the most heartfelt gratitude goes to my parents. They consistently encouraged me, supported me, and believed in me. They gave me confidence and strength in my hardest time. I would like to dedicate this thesis to them, for the unconditional love they have always been giving to me.

Contents

Chapter 1

Introduction

The use of pigments and colors is pervasive in the civilization of human beings. Far back in the stone age, people had already learnt to paint in the cave, and use camouflage pigments in hunting. Producing and trading pigments became such a prosperous industry in the early fifteenth century in Venice that a new profession called "vendecolori" (means color seller) arised [1, 2]. Nowadays the application and study of pigments have been extended to almost every corner of human life. There are traditional color applications, such as textile and painting, and new industries, such as makeup, agriculture, and food industry. According to a market research report [3], the alone global makeup market will be valued at 42 billion dollars in 2015.

Many traditional pigments are toxic (for instance they may contain heavy metals), hence their use in some cases, such as the food industry, is impossible, or dangerous to the environment. Because of this, natural pigments are attracting an increasing interest due to their non-toxicity, friendliness to the environment, and relatively low price. The most common natural pigments are anthocyanins, carotenoids, porphyrins (including chlorophylls), beta-alanines, and tannings. The purpose of this thesis is to unveil the molecular mechanisms responsible for the optical properties and color of a specific class of natural dyes, namely anthocyanins.

1.1 Anthocyanins

Anthocyanins are natural dyes responsible for the bright and diverse coloration of many flowers, such as pansies, pelargonium, or delphiniums, and fruits, including berries, eggplants, or grapes. Unlike other plant pigments, such as chlorophyll and carotenoids, anthocyanins are water-soluble and they are usually found in an aqueous environment in nature, *e.g.* in the vacuole of plant cells [4].

These molecules have long been used in the food industry as colorants [5] (E163 in EU [6]) or additives [7] and anti-oxidant agents [6, 8, 9]. Their anti-oxidant properties are also responsible for potentially beneficial effects against aging, in the treatment of diabetes, or even in cancer prevention. [10, 11, 12] In recent years anthocyanins have also attracted attention for photo-voltaic applications, as components of dye-sensitized solar cells (DSSC), because of their high light-harvesting power in the UV-VIS range, their natural abundance, and their friendliness to the environment. Unfortunately, the efficiency of photovoltaic devices based on anthocyanins is still very low (at the level of 1% [13, 14], compared to $\gtrsim$ 12% [15] for metal-based sensitizers). Another common drawback that hinder some of the potential applications of anthocyanins is their poor stability [16]. A thorough understanding of the mechanisms that determine the optical properties and the stability of these molecules would therefore be instrumental in explaining the present difficulties and in designing ways to overcome them.

Anthocyanins are polylphenolic derivatives, belonging to the flavonoid family [17, 18]. In particular they are glycosides of polyhydroxyl and polymethoxy derivatives of 2-phenylchromenylum cation, or flavylium salt, whose structure is shown in Fig. (1.1) along with the corresponding aglycone form, known as anthocyanidin. A chromenylium group and a phenyl ring form the backbone of the anthocyanidin cation, which is called flavylium [19]. On this backbone, there are 7 specific positions ($R3' \sim R5'$,$R3$, $R5 \sim R7$) that can bind various side groups [19]. Different anthocyanins differ in: (i) the number of hydroxyl groups present in the molecule; (ii) the degree of metylation of these hydroxyl groups; (iii) the number and the position of attached sugars groups, as well as of aliphatic and/or aromatic acids attached to sugars. For instance, in Fig. (1.1)(b) we show the structure of the 3-O-glucoside anthocyanins studied in this thesis, characterized by a glucose group anchored to the $R3$ site of the cation. Anthocyanidins do not accumulate in nature due to their low stability. Glycosylation considerably enhances the stability of anthocyanins, and that is why these molecules are usually found in their anthocyanin form in nature [20].

Hundreds of anthocyanins have been isolated from flowers, plants, and fruits, and chemically characterized by spectroscopic tools (*e.g.* UV-vis [21], IR [22], mass spectroscopy [23], and high-performance liquid chromatography [24].) Among these anthocyanins the six most common ones occurring in nature are cyanin, peonin, pelargonin, malvin, petunin, and delphinin, whose side groups are listed in Tab. (1.1). Their individual structures are also illustrated in Fig. (1.2). Despite the minor chemical differences among them, these molecules express a large range of colors, providing most of the pink, orange, red, violet, and blue colors of fruits and flowers. The interplay between structure and color is not fully understood and is one of the main

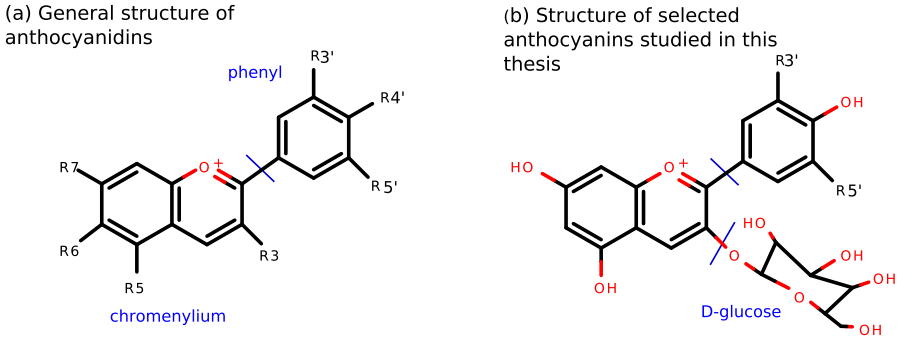

Figure 1.1: Structures of (a) general anthocyanidin [19], and (b) 3-O-glucoside anthocyanins studied in this thesis, in nature sugars can be anchored in different way.

motivations of this thesis.

Group	Anthocyanin	$R3'$	$R5'$	λ_{max} [25]
1	Pelargonin	$-H$	$-H$	510 nm
2	Cyanin	$-OH$	$-H$	528 nm
	Peonin	$-OCH_3$	$-H$	528 nm
3	Malvin	$-OCH_3$	$-OCH_3$	538 nm
	Delphinin	$-OH$	$-OH$	541 nm
	Petunin	$-OH$	$-OCH_3$	540 nm

Table 1.1: Side groups on the phenyl ring of the six most common anthocyanins in nature, see the structure in Fig. (1.1)(b).

The color of anthocyanins shows a strong dependence on the environment, such as the nature and acidity of the solvent [26, 27]. They usually display orange-reddish colors in acidic solutions, purple-bluish colors in neutral solutions, and yellow-greenish in alkaline solutions [28]. In Fig. (1.3) we use the purple carrot extract as an example to illustrate the dependence of anthocyanins' color on the pH value. Since the color of anthocyanins is very sensitive to the pH value, these susstances can be used as a pH indicator [26, 29].

The structure of anthocyanins undergoes significant changes by varying the acidity (see Fig. (1.4)) [30, 31]. The prevalent stable form of anthocyanins at $pH < 2.0$ is the colored flavylium cation ($AH+$). Solvation of the flavylium salt in a slightly acidic or neutral aqueous solution results in the immediate formation of the neutral quinonoidal bases (A). Moreover, at pH values ranging from 4 to 6, the common 3-glycosides and 3,5-diglycosides change rapidly to the more stable carbinol (B) for complete hydratation of the 2-position of the flavilium cation. In this form the anthocyanin has lost its conjugated double bond between the phenyl ring and the chromenylium

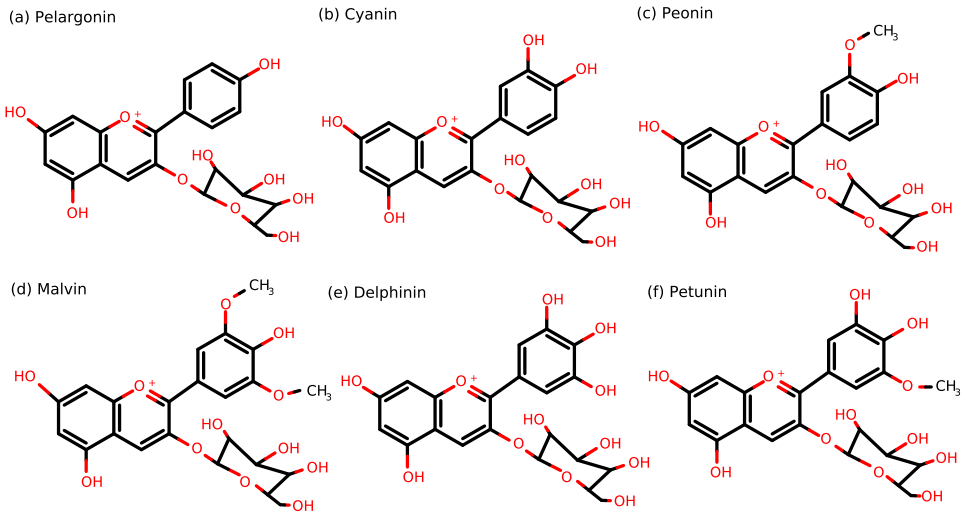

Figure 1.2: Individual structures of six most common anthocyanins in nature.

Figure 1.3: Pictures of purple carrot extract at different pH value [32].

group, therefore it does not absorb visible light [31]. The carbinol in turn can equilibrate, at a slower rate, to an open form, the chalcone pseudobase, which is also colorless. In Fig. (1.5), we display the ratio of these four forms in different pH condition for one selected anthocyanin. In this thesis we focus on the flavylium state only, which is the most stable and studied in most biological systems.

The optical properties of anthocyanins also depend on copigmentation, *i.e.* on the interaction with other, possibly colorless, aromatic molecules whose rings are pi-stacked with the phenyl and chromenylium groups of the anthocaynin. When the copigment is co-soluted with the anthocyanin, the copigmentation is called intermolecular, when it is functionally attached to it the copigmentation is called intramolecular [30]. Intramolecular copigments

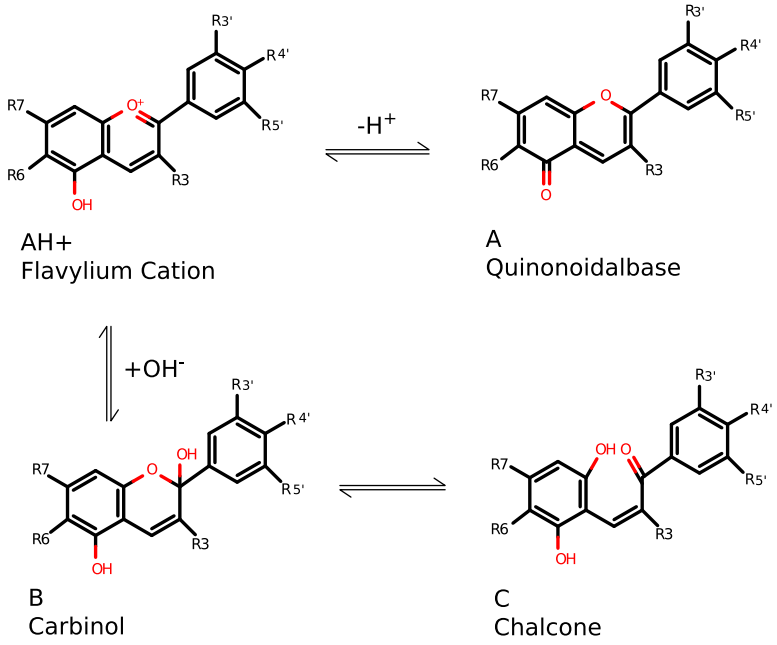

Figure 1.4: The main four equilibrium forms of anthocyanin existing in aqueous media [31].

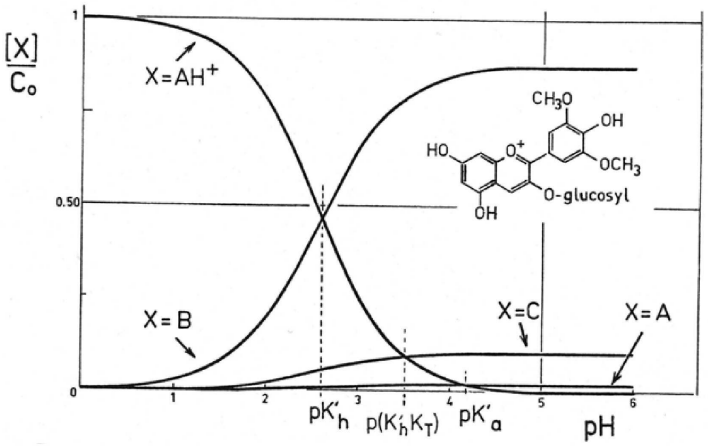

Figure 1.5: The distribution of the different Malvindin-3-glucoside equilibrium forms according to pH [19].

are often organic acids, which can esterify the glycosyl units of anthocyanins. The aromatic ring of the organic acid will then fold to surround the anthocyanin, thus affecting the optical properties of the molecule both directly, and indirectly through the modification of its structure [30, 31]. Due to

the protection of the copigment, the stability of anthoycanins can also be increased [16]. This is another important aspect of copimentation which brings a lot of commercial value to the research of this phenomenon [33]. An example of the copigmentation in nature is the bluish purple flowers of the Japanese garden iris [34]. Even though fundamental for the color expression, we will not consider explicitly copigmentation in the rest of this thesis.

1.2 Simulating molecular colors

When a beam of light impinges on the surface of a material, several different processes occur as illustrated in Fig. (1.6). Part of the light is directly reflected by the surface, while the rest is transmitted into the material. The amount of reflected light depends on the refractive index of the material, the smoothness of the surface and the incidence angle θ. This process gives rise to the so-called `surface gloss` [35]. The surface gloss under a white light source is usually also white, despite the fact that the material itself may have other colors. However materials with a strong optical dispersion (*i.e.* with a refractive index that strongly depends on the wavelength) display a colored gloss, such as metals.

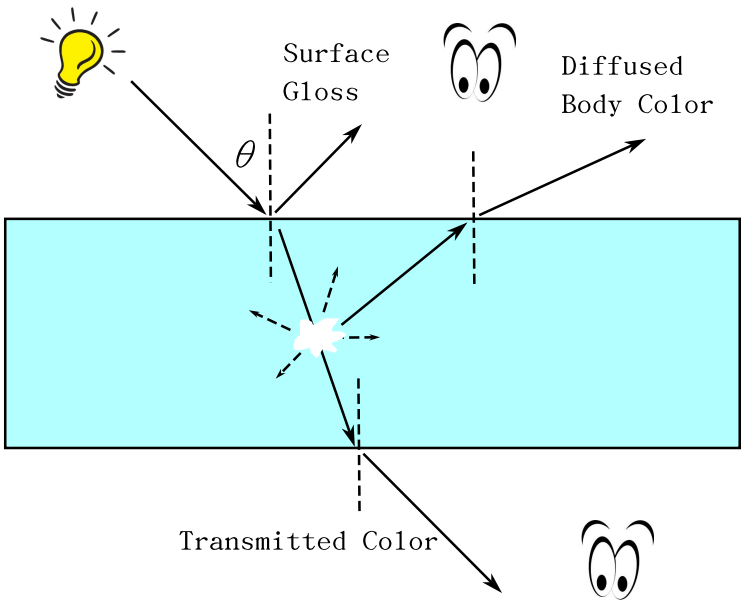

Figure 1.6: Illustration of light interacting with material.

While propagating through the material, the transmitted ray is partially absorbed, partially diffused. Different materials have a different absorption ability at different wavelengths, which is usually represented by a function $\kappa(\lambda)$, the absorption coefficient. Due to the absorption process, the intensity of the light ray at a certain wavelength decreases with the distance traveled within the medium, x, as:

$$I(x,\lambda) = I_0(\lambda) \times e^{-\kappa(\lambda)x}, \tag{1.2.1}$$

where $I_0(\lambda)$ is the intensity of impinging light. In the gas phase or in a dilute molecular solution, the absorption coefficient can be simply expressed in terms of the molecular polarizability, $\alpha(\omega)$:

$$\begin{aligned} \kappa(\lambda) &\propto Im\left[\alpha\left(\frac{2\pi c}{\lambda}\right)\right]/\lambda \\ &\propto \omega Im(\alpha(\omega)). \end{aligned} \tag{1.2.2}$$

The light that is not absorbed nor diffused back, is transmitted to the opposite surface of the material (see Fig. (1.6)). As the diffused and transmitted rays are both attenuated by the same absorption process, the color of these two rays is usually very similar [36].

In order to determine the perceived color, we choose the standard sunlight D65 illuminent [37], which closely matches the natural solar spectrum. The D65 spectrum is illustrated in Fig. (1.7). The maximum power is at wavelengths between 450 nm and 500 nm. According to Eq. (1.2.1), the spectrum of the transmitted or diffused body light is given by:

$$I(\lambda) = D_{65}(\lambda) \times e^{-\kappa(\lambda)x}, \tag{1.2.3}$$

where $D65(\lambda)$ is the spectrum of D65 standard, and x is the typical distance traveled by the ray in the medium. $I(\lambda)$ is the spectrum of the light captured by our eyes.

Our brain interprets as *color* the combination of the neuroelectric signals resulting from the interaction of light with three different cellular photoreceptors,[1] named *cone cells*, that are located at the fovea centralis of the retina [39]. These three types of cone cells are denoted by S, M, and L, according to the wavelength they are sensitive to: **s**hort, **m**iddle and **l**ong. Their response to different wavelengths is described by three functions: $s(\lambda)$, $m(\lambda)$ and $l(\lambda)$ that can be measured by psycho-physical [40] or electrophysiological methods [42]. For a given spectrum $I(\lambda)$, the cone cells give rise to

[1] The most complex eyes in the animal kingdom belong to *odontodactylus scyllarus* who possesses 16 types of photoreceptor cells [38].

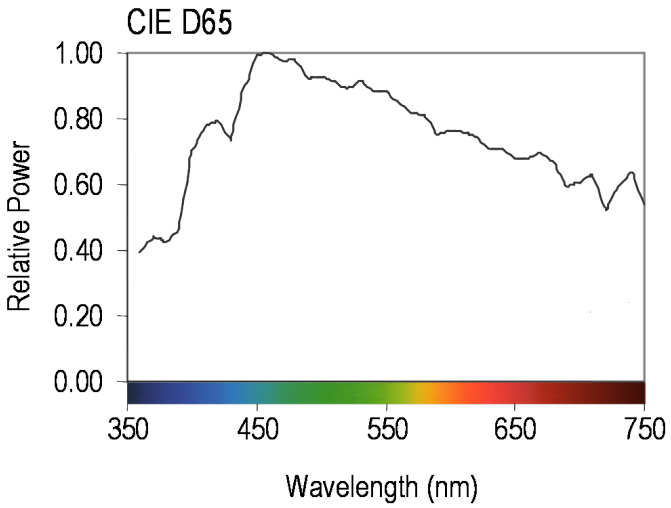

Figure 1.7: Standard illuminant D65 defined by CIE [41].

three neuroelectric signals:

$$\begin{aligned} S &= \int_{380}^{780} I(\lambda)s(\lambda)d\lambda \\ M &= \int_{380}^{780} I(\lambda)m(\lambda)d\lambda \\ L &= \int_{380}^{780} I(\lambda)l(\lambda)d\lambda. \end{aligned} \tag{1.2.4}$$

SML is not a convenient representation of colors, because S, M, and L do not correspond to any monochromatic signal. An alternate representation is to choose three primary colors[2] and measure the human response to them by psycho-physical approaches. Details about this method can be found, e.g., in Ref. [43]. In this approach instead of having SML, one deals with three color matching functions (CMF's): $r(\lambda)$, $g(\lambda)$ and $b(\lambda)$. Integration of the CMF's times the spectrum gives the so-called RGB values:

$$\begin{aligned} R &= \int_{380}^{780} I(\lambda)r(\lambda)d\lambda \\ G &= \int_{380}^{780} I(\lambda)g(\lambda)d\lambda \\ B &= \int_{380}^{780} I(\lambda)b(\lambda)d\lambda. \end{aligned} \tag{1.2.5}$$

R, G and B are usually normalized to a same value, that may be chosen as 1 (or 255 in computer graphic applications), indicating the red, green and

[2] Three primary colors are red(435.8 nm), green(546.1 nm), and blue(700.0 nm)

blue components of a certain color. SML values and the RGB values are related by a simple linear transform:[3]

$$\begin{pmatrix} R \\ G \\ B \end{pmatrix} = T \begin{pmatrix} S \\ M \\ L \end{pmatrix}. \tag{1.2.6}$$

1.3 Quantum mechanical modeling and molecular engineering

Quantum mechanical modeling has become an important tool for molecular engineering, with many applications in different fields, such as the semiconductor industry, drug design, chemical research and catalysis, and nanotechnology. A detailed understanding at the microscopic level of the molecular properties, such as structure, dynamics, and transport, will help us design new materials and devices with custom-tailored properties [44]. To be specific to the research on anthocyanins, our goal is to find systematic patterns that will allow us to design new molecules with desired properties, such as specific color or higher stability. This would require a thorough understanding of the effects of side groups, of glycosilation, copigmentation, temperature, polarity, and acidity of the solution, and so on.

Color and optical properties are related to the excited states of molecule, but they are also strongly affected by its ground-state features, such as the equilibrium molecular structure. In practice, a rough structure of the molecule is first obtained from other, often empirical, sources, and then refined using classical or more accurate quantum-mechenical methods. Among the latter, the most widely used at present is based on density functional theory (DFT). When thermal and dynamical effects on the structure are important, DFT can be combined with classical molecular dynamics, in the nowadays ubiquitous ab-initio molecular dynamics (AIMD) pioneered by Car and Parrnello [45].

As a ground-state theory, DFT gives no access to excited-state properties, such as the optical spectrum, which can instead be described by a dynamical generalization of it, called Time-Dependent Density-Functional Theory (TDDFT) [49]. TDDFT is applicable when the system of interest is subject to a time-dependent perturbation, such as electromagnetic radiation. Similarly to DFT, in this approach the complex many-body time-dependent Schrödinger equation is replaced by a set of time-dependent single-particle

[3] More discussion about the color space can be found in the appendix B.

equations. For this reason this method is computationally much more suitable than cumbersome many-body techniques to calculate optical spectra [50] and, in practice, it is the only possible choice in order to treat nonlinear phenomena in realistic system.

In spite of the plethora of experimental studies on anthocyanins [4, 19, 21, 31, 32], resulting in a wide qualitative description of the chemistry of these substances, a thorough understanding of the structure and of the optical properties of these molecules is still missing [46]. The main difficulties that hinder the theoretical study come from the large number of variables that a realistic model must account for, in order to allow for a detailed comparison with experiment. For instance, the description of the buffer solution and the counter-ions, used to control pH and to neutralize the charged molecular ions, has never been attempted in a theoretical model. A proper model that includes such essential elements as the side groups, sugar moieties, environment conditions, dynamics, and interaction between different molecules, in a unified quantum-mechanical description will be instrumental to control and exploit the properties of these molecules in the food industry, as well as in nanotechnology and bio-medical applications.

1.4 Plan of this thesis

The goal of this thesis is twofold. On one hand, we have developed two new numerical methods to compute the optical spectra of complex molecular systems in complex environments. The first algorithm is a newly proposed Davidson-like approach to Casida's euqation in TDDFT. This method is an extension to the standard Davidson method which was designed for ground-state Hamiltonian problem. The second algorithm is an implementation of a recently proposed pseudo-Hermitian variant of the Liouville-Lanczos approach [51]. In order to correct the well known deficiencies of (semi-) local exchange-correlation (XC) functioanls in reproducing the observed optical gaps, we have implemented hybrid functionals in both of these two algorithms. On the other hand, we have applied these algorithms to perform a systematic study of the optical properties of different anthocyanins. We have calculated the optical spectra of the six most common anthocyanins in the gas phase, with both PBE and hybrid functionals. By analyzing the ground-state and optical properties of different anthocyanins in the gas phase, we have understood the important roles played by different side groups. In order to reproduce the correct color of anthocyanins, we have selected three representative molecule and studied their dynamical and optical properties with an explicit solvent model. The importance of a careful choice of XC functionals in the spectra calculation has been addressed. At the end, we

have developed a *morphing* technique in order to approximate the spectra calculated by precise but costly XC functionals by the less precise but much cheaper calculation.

This thesis is organized in the following way. In chapter 2 the theoretical background of this work is first introduced (Sec. (2.1) and Sec. (2.2)). Then our numerical implementation of two new algorithms is presented (Sec. (2.3)), and their numerical performance is illustrated by numerical experiments (Sec. (2.4)). In chapter 3, these new algorithms are used to study the optical properties of six anthocyanins, first in the gas phase (Sec. (3.1)). Then we analysis the influence of side groups on both the ground-state and the optical properties of anthocyanins (Sec. (3.2)). Finally we study the absorption spectra of anthocyanins in an explicit solvent model (Sec. (3.3)). In the Appendix we also provide a user's guide for the `turbo_davidson.x` executable implemented in the QUANTUM ESPRESSO package.

Chapter 2

Theoretical Background and Numerical Methods

In this chapter we present the theoretical background that underlies the work of this thesis. We start with a brief introduction of ground-state Density Functional Theory (DFT), followed by its extension to time-dependent external potentials, which gives rise to the time-dependent Density Functional Theory (TDDFT). Then two different numerical approaches, turbo-Davidson and turbo-Lanczos, are introduced to solve the TDDFT equations in the linear region, and their respective advantages and disadvantages are discussed in details. At the end, numerical examples are provided to illustrate the performance of our algorithms.

2.1 Density functional theory

Traditional quantum-chemical approaches to molecular structure are based on many-electron wavefunctions. While potentially exact, such approaches are in practice limited to systems of very small size, as their complexity grows very rapidly with the number of electrons in the system. As an alternative one may think to describe the many-body system in terms of its ground-state particle density, which is a function of only three coordinates. This idea has given rise to density functional theory (DFT). The theoretical framework of DFT is based upon two theorems, first proved by Hohenberg and Kohn [52]:[1]

Theorem I: For any system of interacting particles in an external potential $V_{ext}(\mathbf{r})$, the potential $V_{ext}(\mathbf{r})$ is determined uniquely, except for a

[1] The demonstration of these two theorems can be found in many textbooks (*e.g.*, see reference [57], chapter 6).

constant, by the ground-state particle density $n_0(\mathbf{r})$.

Theorem II: An *universal functional* of the electron density $F[n]$ can be defined, such that the ground-state energy, as a functional of the external potential, $E_0[V_{ext}]$, can be derived from the variational principle:

$$E_0[V_{ext}] = \min_n \left(F[n] + \int d\mathbf{r} V_{ext}(\mathbf{r}) n(\mathbf{r}) \right) + E_{ion}, \tag{2.1.1}$$

subject to the constraint that electron density is normalized to the total number of electrons:

$$\int d\mathbf{r} n(\mathbf{r}) = N. \tag{2.1.2}$$

In Eq. (2.1.1) the term E_{ion} denotes the ionic Coulomb energy which reads:[2]

$$E_{ion} = \frac{1}{2} \sum_{I \neq J} \frac{Z_I Z_J}{|\mathbf{R}_I - \mathbf{R}_J|}, \tag{2.1.3}$$

where Z's and R's are respectively the ionic charges and coordinates. The density that minimizes Eq. (2.1.1) is the ground-state density $n_0(\mathbf{r})$. The differential form of this variational problem, Eq. (2.1.1), reads:

$$\frac{\delta F[n]}{\delta n(\mathbf{r})} + V_{ext}(\mathbf{r}) = \mu, \tag{2.1.4}$$

where the Lagrange multiplier μ accounts for the constraint on the total number of electrons, Eq.(2.1.2).

The Hohenberg-Kohn (HK) theorems demonstrate the existence of such a functional, $F[n]$, connecting the ground state of a many-body quantum system to its ground-state particle density, whose explicit form is however unknown. A practical recipe for computing this functional is provided by the Kohn-Sham (KS) *ansatz*, which maps the many-body system onto an *auxiliary system of non-interacting particles*. The ground-state density of N non interacting electrons is defined as:[3]

$$n(\mathbf{r}) = \sum_{v \in occ} 2 \left| \psi_v(\mathbf{r}) \right|^2, \tag{2.1.5}$$

where the summation runs over the occupied states, and $\{\psi_v(\mathbf{r})\}$ are single particle wavefunctions. The kinetic energy of such a system reads :

$$T_0 = -\frac{1}{2} \sum_{v \in occ} \left\langle \psi_v | \nabla^2 | \psi_v \right\rangle. \tag{2.1.6}$$

[2] In this thesis, Hartree atomic unit is used: $\hbar = m = e = 1$.

[3] Here the factor 2 accounts for the double degeneracy of occupied states in the non-spin polarized system.

The Hartree energy, defined as the classical electrostatic energy of a system with electron density $n(\mathbf{r})$, reads:

$$E_H[n] = \frac{1}{2}\int d\mathbf{r}d\mathbf{r}'\frac{n(\mathbf{r})n(\mathbf{r}')}{|\mathbf{r}-\mathbf{r}'|}. \tag{2.1.7}$$

The KS ansatz consists of a splitting of the HK functionals into the sum of T_0, E_H and a third functional called the exchange-correlation (XC) energy:

$$F[n] = T_0[n] + E_H[n] + E_{xc}[n]. \tag{2.1.8}$$

Strictly speaking, Eq. (2.1.8) is only a definition of the XC energy, which is the difference between what we can compute and what we cannot.[4] The actual power of this *ansatz* depends on the possibility that this XC term is small and can be accurately approximated. This issue will be addressed in the following paragraph.

Applying the variational equation of Theorem II, Eq. (2.1.4), we obtain the Euler equation:

$$\frac{\delta T_0[n]}{\delta n(\mathbf{r})} + V_{KS}(\mathbf{r}) = \mu, \tag{2.1.9}$$

where V_{KS} is defined as:

$$\begin{aligned} V_{KS}(\mathbf{r}) &\equiv \frac{\delta E_H[n]}{\delta n(\mathbf{r})} + \frac{\delta E_{xc}[n]}{\delta n(\mathbf{r})} + V_{ext}(\mathbf{r}) \\ &\equiv V_H(\mathbf{r}) + V_{xc}(\mathbf{r}) + V_{ext}(\mathbf{r}). \end{aligned} \tag{2.1.10}$$

Equation (2.1.9) is the same that would hold for a system of non-interacting electrons, subject to an effective potential $V_{KS}(\mathbf{r})$. For this reason we can define the Hamiltonian of an auxiliary non-interacting system as:[5]

$$\hat{H}_{KS} = -\frac{1}{2}\nabla^2 + V_{KS}(\mathbf{r}). \tag{2.1.11}$$

The Schrödinger equation of this non-interacting system reads:

$$\hat{H}_{KS}\psi_i(\mathbf{r}) = \varepsilon_i\psi_i(\mathbf{r}), \tag{2.1.12}$$

which is called KS equation, its eigenfunctions are the KS orbitals, and the corresponding eigenvalues are called KS orbital energies. The N KS orbitals with the lowest energies are used to calculate the density of the auxiliary system, as in Eq. (2.1.5). As V_{KS} is a functional of the density, the KS

[4] It was named *stupidity energy* by R.P. Feynman [53].

[5] In this thesis, when no confusion can arise, quantum-mechanical operators are denoted by a hat, "ˆ", while local operators, such as one-electron potentials, will be indicated by the diagonal of their coordinate representation, $V(\mathbf{r})$.

equation is usually solved self-consistently, otherwise one has to solve a non-linear equation. One should notice that the eigenvalues and eigenfunctions of the KS equations do not have any strict physical meaning. Instead they are just mathematical tools used to obtain the ground-state energy and charge density. Once the KS equation is solved, the total energy can be calculated as:

$$E_0[V_{ext}] = \min_n(E[n, V_{ext}]) = E[n_0, V_{ext}]$$
$$= -\sum_v \int d\mathbf{r}\psi_v^*(\mathbf{r})\frac{\partial^2\psi_v(\mathbf{r})}{\partial\mathbf{r}^2} + \int d\mathbf{r}V_{ext}(\mathbf{r})n_0(\mathbf{r}) + E_H[n_0] + E_{xc}[n_0] + E_{ion}. \tag{2.1.13}$$

Exchange-correlation functionals

Given the exact form of the XC functional, DFT would give the exact ground-state properties of an many-body interacting system. Unfortunately, the exact form of $E_{xc}[n]$ is unknown, therefore in practice different approximations are used to account for this term. The most commonly used approximations are the (semi-) local approximations which assume that the XC energy depends only (semi-) locally on the electron density.[6] The Local Density Approximation (LDA) can be mathematically formulated as:

$$E_{xc}^{LDA}[n] = \int d\mathbf{r}\varepsilon_{xc}^{LDA}\left(n(\mathbf{r})\right)n(\mathbf{r}), \tag{2.1.14}$$

where ε_{xc}^{LDA} is the XC energy per electron of the electron gas with a homogeneous density n. The Generalized Gradient Approximation (GGA), which is a semi-local approximation due to the dependence on the local density gradient, is given as:

$$E_{xc}^{GGA}[n](\mathbf{r}) = \int d\mathbf{r}\varepsilon_{xc}\left(n(\mathbf{r}), \nabla n(\mathbf{r})\right)n(\mathbf{r}). \tag{2.1.15}$$

The three most popular GGA functionals are those of Becke (B88) [54], Perdew and Wang (PW91) [55], and Perdew, Burke, and Enzerhof (PBE) [56].

In general the (semi-) local approximations produce good accuracy in computing molecular and crystal structures, and their vibration properties. However, these approximations fail to capture the very essence of interaction effects in strongly correlated materials and in weakly bound molecular

[6] XC functionals are only briefly introduced in this thesis. For a review of XC functionals see, *e.g.* reference [57], chapter 8.

systems where intrinsically non-local interactions play important roles [118]. One way to take into account the non-local feature of the XC functionals is to adopt hybrid functionals [58], in which the exchange energy is assumed to be a linear combination of a semi-local (GGA-like) and a fully non-local (Fock-like) component. The ground-state Hamiltonian of a N particle system for a hybrid functional takes the form:

$$\begin{aligned}\hat{H}\psi_j(\mathbf{r}) = &\left(-\frac{1}{2}\nabla^2 + V_H(\mathbf{r}) + V_{xc}^{hyb}(\mathbf{r}) + V_{ext}(\mathbf{r})\right)\psi_j(\mathbf{r}) \\ &+ \alpha \int d\mathbf{r}' V_{exx}(\mathbf{r},\mathbf{r}')\psi_j(\mathbf{r}'),\end{aligned} \tag{2.1.16}$$

where V_H and V_{ext} are the same Hartree and external potentials as defined in Eq. (2.1.10), and V_{xc}^{hyb} denotes all the local or semi-local exchange-correlation contributions to the XC potential. For instance, in the case of the PBE0 hybrid functional [59], $V_{xc}^{hyb} = V_C^{PBE} + (1-\alpha)V_X^{PBE}$, where $\alpha = 0.25$ and V_X^{PBE} and V_C^{PBE} are respectively the exchange and correlation part of PBE functional. The Fock-exchange operator in the last term is defined as:

$$\int d\mathbf{r}' V_{exx}(\mathbf{r},\mathbf{r}')\psi_j(\mathbf{r}') = -\sum_{i\in occ}\psi_i(\mathbf{r})\int d\mathbf{r}'\frac{\psi_i(\mathbf{r}')\psi_j(\mathbf{r}')}{|\mathbf{r}-\mathbf{r}'|}. \tag{2.1.17}$$

It should be noticed that the exact exchange is only between orbitals with the same spin. In the following we will use $\hat{V}_{Hxc} = \hat{V}_H + \hat{V}_{xc}^{hyb}$ to indicate the local Hartree and exchange-correlation components.

Atomic forces and molecular dynamics

It is often useful to know the derivative of the ground-state energy with respect to some external parameters. A specific example of this is the energy derivatives with respect to the atomic coordinates, giving rise to the atomic forces:

$$\mathbf{F}_I = -\frac{dE_0[\{\mathbf{R}\}]}{d\mathbf{R}_I}. \tag{2.1.18}$$

Atomic forces are important to find equilibrium molecular geometry and perform molecular dynamics (MD). In principle, the ground-state energy depends on nuclear positions $\{\mathbf{R}_I\}$ both explicitly, because the molecular Hamiltonian does so through the external potential, and implicitly, through the ground-state wavefunctions. The Hellmann-Feynman theorem [60] states that the forces acting on atoms are the expectation values of only the derivatives of the external plus ionic Coulomb potential. Instead the implicit dependence of the energy on the nuclear coordinates through the ground-state wavefunction does not contribute to the forces. This theorem is easily

demonstrated by expanding the derivative in Eq. (2.1.18) with Eq. (2.1.13):

$$\begin{aligned}\mathbf{F}_I &= -\left.\frac{\partial E}{\partial \mathbf{R}_I}\right|_{n=n_0} - \int d\mathbf{r} \left.\frac{\delta E}{\delta n(\mathbf{r})}\right|_{n=n_0} \frac{\partial n_0(\mathbf{r})}{\partial \mathbf{R}_I} \\ &= -\frac{\partial E_0}{\partial \mathbf{R}_I} \\ &= -\int d\mathbf{r} \frac{\partial V_{ext}(\mathbf{r})}{\partial \mathbf{R}_I} n_0(\mathbf{r}) - \frac{\partial E_{ion}}{\partial \mathbf{R}_I},\end{aligned} \tag{2.1.19}$$

where n_0 is the ground-state charge density. The second term in the first line of this equation vanishes due to the variational principle in the HK Theorem II.

Because the mass of electrons is much smaller than that of nuclei, the time evolution of electrons is much more rapid than nuclear motion. In the Born-Oppenheimer (BO) dynamics, these two freedoms of motion are considered separately. In MD simulations, for any molecular configuration occurring at each step, the ground-state density is first calculated by solving KS equations, then the ionic coordinates are updated by integrating the equations of motion:

$$M_I \ddot{\mathbf{R}}_I = \mathbf{F}_I = -\int d\mathbf{r} \frac{\partial V_{ext}(\mathbf{r})}{\partial \mathbf{R}_I} n_0(\mathbf{r}) - \frac{\partial E_{ion}}{\partial \mathbf{R}_I}, \tag{2.1.20}$$

for a small time step. This approach is rather straightforward and usually stable, but its drawback is that the electronic configuration has to be converged for every single ionic step. In the Car-Parrinello (CP) algorithm [45], this problem is avoided by letting both ionic and electronic degrees of freedom evolve under the action of a fictitious Lagrangian:

$$\begin{aligned}L = &\sum_i 2\mu \int d\mathbf{r} \left|\dot{\psi}_i(\mathbf{r})\right|^2 + \sum_I \frac{1}{2} M_I |\dot{\mathbf{R}}_I|^2 - E[\{\psi_i\}, \{\mathbf{R}_I\}] \\ &+ \sum_{ij} \Lambda_{ij} \left[\int d\mathbf{r} \psi_i(\mathbf{r}) \psi_j(\mathbf{r}) - \delta_{ij}\right],\end{aligned} \tag{2.1.21}$$

where μ is the fictitious electronic mass, M_I is the atomic mass, and Λ in the last term is the matrix of Lagrange multipliers used to enforce the orthonormality of the electronic states. The resulting equations of motion are:

$$\begin{aligned}\mu \ddot{\psi}_i(\mathbf{r}, t) &= -\hat{H}_{KS} \psi_i(\mathbf{r}, t) + \sum_j \Lambda_{ij} \psi_j(\mathbf{r}, t), \\ M_I \ddot{\mathbf{R}}_I = \mathbf{F}_I &= -\int d\mathbf{r} \frac{\partial V_{ext}(\mathbf{r})}{\partial \mathbf{R}_I} n(\mathbf{r}) - \frac{\partial E_{ion}}{\partial \mathbf{R}_I}.\end{aligned} \tag{2.1.22}$$

In the presence of a large gap in the electronic spectrum, a wise choice of the fictitious mass μ makes it possible to limit the energy transfer from the nuclear to the electronic degrees of freedom, thus reducing the need of re-optimizing the electronic wavefunctions at each ionic step.

2.2 Time-dependent density functional theory

Strictly speaking, DFT is a ground-state theory and it gives no access to the properties of excited states. In this section, we introduce the theoretical background of a very general and powerful extension of DFT, the Time-Dependent Density Functional Theory (TDDFT), which modifies the standard ground-state DFT to deal with time-dependent external potentials, and can be used to study the excited states.

This section is separated into 6 subsections. We start from the time-dependent Kohn-Sham equation, then derive the density matrix formalism of linear response TDDFT. The TDDFT problem with zero external perturbation leads to the free oscillation modes of the system which can be determined by solving Casida's equation. In the third subsection, the Casida's equation and its connection to problems where perturbations are present, are introduced. In order to solve the equations introduced in the first three subsections, an explicit representation of the response density matrix is required. While the traditional particle-hole representation has severe difficulties for plane-wave method, the so-called batch representation is introduced in the fourth subsection. In the fifth subsection, the linear response TDDFT is extended to work with hybrid functionals. In the last subsection, several approximations are discussed, among which the double-pole approximation is very useful for understanding anthocyanins' optical spectra in the next chapter.

2.2.1 Time-dependent Kohn-Sham equations

The framework of TDDFT is mathematically established by two theorems introduced by Runge and Gross [49], which are similar to their DFT counterparts:

Theorem I: For any system of interacting electrons in an external time-dependent potential $V_{ext}(\mathbf{r}, t)$, which can be expanded in Taylor series with respect to time, and given an initial state $\Psi(t_0) = \Psi_0$, there is a one-to-one correspondence (apart from a trivial function of time only) between $V_{ext}(\mathbf{r}, t)$ and the time-dependent particle density $n(\mathbf{r}, t)$.

Theorem II: If we define the action integral:

$$A = \int_{t_0}^{t_1} dt \left\langle \Psi(t) | i\frac{\partial}{\partial t} - \hat{H}(t) | \Psi(t) \right\rangle, \tag{2.2.1}$$

then A can be expressed as a functional of the density:

$$A[n] = S[n] - \int_{t_0}^{t_1} dt \int d\mathbf{r} n(\mathbf{r}, t) V_{ext}(\mathbf{r}, t), \tag{2.2.2}$$

where $S[n]$ is a universal functional of the time-dependent density (namely it does not depend on the external potential) and $A[n]$ is stationary for variations around the exact time-dependent density of the system.

The first theorem states that, for a given initial state, the time-dependent potential is determined by the time-dependent electron density. The second theorem is a variational principle stating that the exact density of the system minimizes the action integral $A[n]$. In order to perform calculations with TDDFT, a time-dependent version of Kohn-Sham's *ansatz* in DFT is applied for TDDFT:

$$A[n] = S_0[n] + S_H[n] + S_{xc}[n] - \int_{t_0}^{t_1} dt \int d\mathbf{r} n(\mathbf{r}, t) V_{ext}(\mathbf{r}, t), \tag{2.2.3}$$

where S_0 denotes the functional for non-interacting electrons, S_H is defined as:

$$S_H[n] = -\frac{1}{2} \int_{t_0}^{t_1} dt \int \int d\mathbf{r} d\mathbf{r}' \frac{n(\mathbf{r}, t) n(\mathbf{r}', t)}{|\mathbf{r} - \mathbf{r}'|}, \tag{2.2.4}$$

and the term S_{xc}, analogously to ground-state DFT, contains all the missing contributions to the functional $A[n]$. A time-dependent version of KS potential can be defined as:

$$\begin{aligned} V_{KS}[n](\mathbf{r}, t) &\equiv V_H(\mathbf{r}, t) + V_{xc}(\mathbf{r}, t) + V_{ext}(\mathbf{r}, t) \\ &\equiv \int \frac{n(\mathbf{r}', t)}{|\mathbf{r} - \mathbf{r}'|} d\mathbf{r}' - \frac{\delta S_{xc}[n]}{\delta n(\mathbf{r}, t)} + V_{ext}(\mathbf{r}, t). \end{aligned} \tag{2.2.5}$$

The stationary-action principle leads to the equation:

$$\frac{\delta S_0[n]}{\delta n(\mathbf{r}, t)} - V_{KS}[n](\mathbf{r}, t) = 0, \tag{2.2.6}$$

which is equivalent to the Euler equation of a system with independent electrons subject to a time-dependent potential, $V_{KS}(\mathbf{r}, t)$. Therefore, the exact density of the time-dependent many-body system can be obtained from the solution of a fictitious non-interacting time-dependent Kohn-Sham (TDKS) equation:

$$i\frac{\partial}{\partial t}\psi_i(\mathbf{r}) = \left[-\frac{1}{2}\nabla^2 + V_{KS}[n](\mathbf{r}, t) \right] \psi_i(\mathbf{r}) \equiv \hat{H}_{KS}\psi_i(\mathbf{r}). \tag{2.2.7}$$

From the eigenfunctions $\{\psi_i\}$ the time-dependent density can be calculated as:

$$n(\mathbf{r},t) = \sum_{v\in occ} |\psi_v(\mathbf{r},t)|^2 , \tag{2.2.8}$$

where the summation runs over the occupied states.

TDDFT does not give direct access to excited-state energies and properties. However, knowledge of linear response functions, that can be calculated within TDDFT, would allow us to estimate energies and transition matrix elements for electronic excitations. To see this, let us suppose that an otherwise time-independent system is subject to a time-dependent perturbation $V'(r,t) = \lambda(t)B(\mathbf{r})$, the time evolution of a one-body operator $\hat{A}$ is defined as: $\langle A(t)\rangle = \left\langle \Psi(t)|\hat{A}(t)|\Psi(t)\right\rangle$. The generalized susceptibility is defined as:

$$\chi_{AB}(t-t') \equiv \frac{\delta\langle A(t)\rangle}{\delta\lambda(t')}, \tag{2.2.9}$$

According to many-body perturbation theory, in the frequency domain the susceptibility of a many-body system can be written as (Lehmann representation) [61]:

$$\tilde{\chi}_{AB}(\omega) = \sum_n \left[\frac{\left\langle \Psi_0|\hat{A}|\Psi_n\right\rangle \left\langle \Psi_n|\hat{B}|\Psi_0\right\rangle}{\omega - (E_n - E_0) + i\epsilon} - \frac{\left\langle \Psi_0|\hat{B}|\Psi_n\right\rangle \left\langle \Psi_n|\hat{A}|\Psi_0\right\rangle}{\omega + (E_n - E_0) + i\epsilon} \right], \tag{2.2.10}$$

where ϵ is an infinitesimal positive number, Ψ_0 and Ψ_n are the ground-state and excited-state wavefunctions corresponding to the energy E_0 and E_n, respectively. It can be seen that the generalized susceptibility $\tilde{\chi}_{AB}$ has pole at the frequency equals to one of the excitation energies, therefore the exited energies of a many-body system can be obtained by studying its behavior in a time-dependent external potential.

Similarly to DFT, TDDFT is an exact theory, but the exact functional for $V_{xc}[n](\mathbf{r},t)$ is not known. In practice, two levels of approximations are often adopted [62]. The first is called the *adiabatic approximation*, which assumes that the XC potential at a given time depends on the density at the same time alone, and the second approximation says that the dependence is the same as that of the ground-state XC potential on the ground-state electron density. It is not surprising that the same shortcoming of (semi-) local functionals in DFT certainly affects the TDDFT calculation as well. For the photo-absorption spectra of solids or low dimensional extended systems, such as nanostructures or long polymers, the predictive power of TDDFT is not as established. Referring to atoms and molecules, Rydberg series are not reproduced by TDDFT since the corresponding states are usually unbound. Besides, another famous flaw of TDDFT is the failure to describe

charge-transfer excitation [63]. What these seemingly different phenomena have in common is that the energy of the excited states is determined by the long-range, Coulombic, tail of the eh interaction, which can not be correctly described by the (semi-) local potentials. This long-range interaction is specially important in the case of copigmentation in which aromatic rings of copigments are pi-stacked with anthocyanins by non-bonded interaction. This is one of the motivations that we would like to consider hybrid functionals where the non-local Fock operation is taken into account to calculate the XC energy. In Sec. (2.2.5), the formulation to use hybrid functionals in TDDFT will be introduced.

2.2.2 Linear-response TDDFT

Susceptibility is the key to connect time-dependent properties to the excitation energies. It is the first order derivative of the response density respect to the external perturbation (see Eq. (2.2.9)). This allows us to apply linear-response TDDFT, for which we will adopt a slightly different formalism with respect to the previous subsection, in order to have a more elegant expression of formulae.

Density matrix

For the sake of convenience, we use the density matrix defined as:

$$\hat{\rho}(t) = \sum_{v \in occ} |\psi_v(t)\rangle \langle \psi_v(t)|, \tag{2.2.11}$$

instead of KS wavefunctions to describe the quantum system. Here we briefly summarize several properties of the density matrix. The density matrix of a system of non-interacting electrons is idempotent:

$$\hat{\rho}^2 = \hat{\rho}. \tag{2.2.12}$$

The density matrix in the coordinate representation is defined as:[7]

$$\rho(\mathbf{r}, \mathbf{r}', t) = 2 \left\langle \mathbf{r} | \hat{\rho}(t) | \mathbf{r}' \right\rangle, \tag{2.2.13}$$

whose diagonal gives rise to the electron density:

$$n(\mathbf{r}, t) = \rho(\mathbf{r}, \mathbf{r}, t) = 2 \langle \mathbf{r} | \hat{\rho}(t) | \mathbf{r} \rangle \tag{2.2.14}$$

For an operator $\hat{A}$, its expectation value, $\langle A \rangle$, is given by:

$$\langle A \rangle = Tr \left(\hat{A}^\dagger \hat{\rho} \right). \tag{2.2.15}$$

[7] In a non spin-polarized calculation, each orbital has double degeneracy, therefore a factor 2 should be added in this expression.

The trace of the product of two operators can be seen as a scalar product in the linear space of operators. Suppose $\hat{A}$ and $\hat{B}$ are two operators, we can define the *scalar product* of two operators as:

$$\left(\hat{A}, \hat{B}\right) \equiv Tr(\hat{A}^\dagger \hat{B}). \tag{2.2.16}$$

Here we have used $(\cdot, \cdot)$ to indicate the inner product of two operators, in order to distinguish it from the inner product for wavefunctions which is denoted by $\langle \cdot | \cdot \rangle$. Therefore, Eq. (2.2.15) can be rewritten as:

$$\langle A \rangle = \left(\hat{A}, \hat{\rho}\right). \tag{2.2.17}$$

Quantum Liouville equation and linearization

Using density matrices, the TDKS, Eq. (2.2.7), can be written as:

$$i\frac{d\hat{\rho}(t)}{dt} = \left[\hat{H}_{KS}[\hat{\rho}](t), \hat{\rho}(t)\right], \tag{2.2.18}$$

where $[\cdot, \cdot]$ indicates the commutator. In order to linearize this equation, we split the time-dependent density matrix into two parts:

$$\hat{\rho}(t) = \hat{\rho}^\circ + \hat{\rho}'(t), \tag{2.2.19}$$

where $\hat{\rho}^\circ$ denotes the unperturbed density matrix, and $\hat{\rho}'(t)$ is the response caused by the time-dependent external potential. Similarly, all the terms in the definition of $\hat{H}_{KS}$ can also be splitted into a time-independent unperturbed part and the time-dependent response part:[8]

$$\begin{aligned} \hat{H}_{KS}(t) &= \hat{T}_0 + V^\circ_{Hxc}(\mathbf{r}) + V^\circ_{ext}(\mathbf{r}) + V'_{Hxc}[\hat{\rho}'](\mathbf{r}, t) + V'_{ext}(\mathbf{r}, t) \\ &\equiv \hat{H}^\circ_{KS} + V'_{Hxc}[\hat{\rho}'](\mathbf{r}, t) + V'_{ext}(\mathbf{r}, t), \end{aligned} \tag{2.2.20}$$

where $V'_{Hxc}[\hat{\rho}'](\mathbf{r}, t)$ is the linear correction to the Hartree-plus-XC potential, whose coordinate representation reads:

$$V'_{Hxc}[\hat{\rho}'](\mathbf{r}, t) = \int d\mathbf{r}' dt' \left[\frac{1}{|\mathbf{r} - \mathbf{r}'|} + f_{xc}(\mathbf{r}, \mathbf{r}'; t - t')\right] n'(\mathbf{r}', t'), \tag{2.2.21}$$

where f_{xc} is the so-called XC kernel [64] that, according to the adiabatic DFT approximation, is assumed to be local in time. Putting Eqs. (2.2.18),

[8] Here we denote the Hatree term together with the XC term as $V_{Hxc}[\hat{\rho}]$ just for the sake of convenience.

(2.2.19) , and (2.2.20) together and keeping only terms up to first order we get:

$$i\frac{d\hat{\rho}'(t)}{dt} = \left[\hat{H}^{\circ}_{KS}, \hat{\rho}'(t)\right] + \left[\hat{V}'_{Hxc}[\hat{\rho}'(t)], \hat{\rho}^{\circ}\right] + \left[\hat{V}'_{ext}(t), \hat{\rho}^{\circ}\right]. \tag{2.2.22}$$

Since the first two terms in Eq. (2.2.22) are both linear functionals of $\hat{\rho}'$, we can pack them together and define a linear "super-operator" $\mathcal{L}$ as:

$$\mathcal{L}\hat{\rho}' = \left[\hat{H}^{\circ}_{KS}, \hat{\rho}'(t)\right] + \left[\hat{V}'_{Hxc}[\hat{\rho}'(t)], \hat{\rho}^{\circ}\right]. \tag{2.2.23}$$

Hence Eq. (2.2.22) can be rewritten as:

$$i\frac{d\hat{\rho}'(t)}{dt} = \mathcal{L}\hat{\rho}'(t) + \left[\hat{V}'_{ext}(t), \hat{\rho}^{\circ}\right]. \tag{2.2.24}$$

We can transform Eq. (2.2.24) into the frequency domain:

$$(\omega - \mathcal{L})\hat{\rho}'(\omega) = \left[\hat{V}'_{ext}(\omega), \hat{\rho}^{\circ}\right], \tag{2.2.25}$$

One is usually interested in only a few types of perturbations and responses. For instance, when calculating the dynamical polarizability as the response to visible light, if the molecule is much smaller than the wavelength of the light, we can use the dipole approximation, and one has:

$$V'_{ext}(\mathbf{r}, \omega) = -\mathbf{E}(\omega) \cdot \mathbf{r}. \tag{2.2.26}$$

According to Eq. (2.2.17) the dipole induced by the perturbing potential can be expressed as:

$$\mathbf{d}(\omega) = -\left(\hat{\mathbf{r}}, \hat{\rho}'(\omega)\right). \tag{2.2.27}$$

The dipole given by Eq. (2.2.27) being a vector, its Cartesian components can be expressed as:

$$d_{\mu}(\omega) = \sum_{\nu} \alpha_{\mu\nu}(\omega) E_{\nu}(\omega), \tag{2.2.28}$$

where the μ,ν are subscripts indicating the three Cartesian directions, and the dynamical polarizabitliy, $\alpha_{\mu\nu}(\omega)$, is defined as:

$$\alpha_{\mu\nu}(\omega) \equiv \frac{\partial d_{\mu}}{\partial E_{v}} = -\left(\hat{r}_{\mu}, (\omega - \mathcal{L})^{-1} \cdot [\hat{r}_{\nu}, \hat{\rho}^{\circ}]\right), \tag{2.2.29}$$

where $\hat{r}_{\mu}$ is the μ-th component of the dipole operator. According to Eq. (1.2.2), the absorption spectrum can be calculated as:

$$\kappa(\omega) \propto \frac{1}{3}\omega Im[\alpha_{11}(\omega) + \alpha_{22}(\omega) + \alpha_{33}(\omega)], \tag{2.2.30}$$

where the average is taken for three Cartesian directions.

2.2.3 Spectral representation and Casida's equation

The right side of the inner product in Equation(2.2.29) is given by the solution of the linear equation:

$$(\omega - \mathcal{L})\hat{\rho}' = [\hat{r}_\nu, \hat{\rho}^\circ]. \tag{2.2.31}$$

When the external perturbation is absent, this equation is an eigenvalue equation for the free oscillation modes of the electronic system. The oscillation frequencies, *i.e.* the eigenvalues of this equation, are the excitation energies of the system. This is essentially Casida's approach to TDDFT [65, 66].

Since $\mathcal{L}$ is a non-Hermitian operator, we consider both its right and left eigenvectors:

$$\begin{cases} \mathcal{L}\hat{v}_i = \omega_i \hat{v}_i, \\ \mathcal{L}^\dagger \hat{u}_i = \omega_i \hat{u}_i. \end{cases} \tag{2.2.32}$$

In Sec. (2.2.4) it will be shown that a suitable choice of representation allows to put the Liouvillian in the block form as:

$$\mathcal{L} = \begin{pmatrix} 0 & \mathcal{B} \\ \mathcal{A} & 0 \end{pmatrix}. \tag{2.2.33}$$

Although $\mathcal{L}$ is not a Hermitian matrix, both of its block elements $\mathcal{A}$ and $\mathcal{B}$ are. Keeping this in mind, we suppose $\hat{v} = (Q, P)^T$ is the right eigenvector of $\mathcal{L}$ which leads to:

$$\mathcal{L}\begin{pmatrix} Q \\ P \end{pmatrix} = \begin{pmatrix} \mathcal{A}P \\ \mathcal{B}Q \end{pmatrix} = \omega \begin{pmatrix} Q \\ P \end{pmatrix}, \tag{2.2.34}$$

it is easy to verify that $\mathcal{L}$ acting on its conjugated vector $(P, Q)^T$ gives:

$$\mathcal{L}^T\begin{pmatrix} P \\ Q \end{pmatrix} = \begin{pmatrix} \mathcal{B}Q \\ \mathcal{A}P \end{pmatrix} = \omega \begin{pmatrix} P \\ Q \end{pmatrix}. \tag{2.2.35}$$

This exactly means that vector $(P, Q)^T$ is the left eigenvector of $\mathcal{L}$. Conjugated left eigenvector $\hat{u}$ and right eigenvector $\hat{v}$ are connected by the transform:

$$\hat{u} = \begin{pmatrix} 0 & 1 \\ 1 & 0 \end{pmatrix} \hat{v} \tag{2.2.36}$$

Therefore in practice, only the first equation in Eq. (2.2.32) is solved. The left eigenvectors can be easily obtained from their corresponding right eigenvector.

The left and right eigenvectors of a matrix satisfy the bi-orthogonality condition:

$$(\hat{u}_i, \hat{v}_j) = \delta_{ij}. \tag{2.2.37}$$

and a complete set of eigenvectors can be used to construct the identity operator:

$$\hat{I} = \sum_i |\hat{v}_i\rangle \langle\hat{u}_i| . \tag{2.2.38}$$

Inserting this expression into Eq. (2.2.29) leads to:

$$\begin{aligned} \alpha_{\mu\nu}(\omega) = \left(\hat{r}_\mu, (\omega - \mathcal{L})^{-1} \cdot \hat{s}_\nu\right) &= \sum_{lm} (\hat{r}_\mu, \hat{v}_l) \left(\hat{u}_l, (\omega - \mathcal{L})^{-1} \cdot v_m\right) (\hat{u}_m, \hat{s}_\nu) \\ &= \sum_{lm} (\hat{r}_\mu, \hat{v}_l) \frac{\delta_{lm}}{\omega - \omega_m + i\epsilon} (\hat{u}_m, \hat{s}_\nu) \\ &= \sum_{l} \frac{(\hat{r}_\mu, \hat{v}_l) (\hat{u}_l, \hat{s}_\nu)}{\omega - \omega_l + i\epsilon}, \end{aligned} \tag{2.2.39}$$

where

$$\hat{s}_\nu = -[\hat{r}_\nu, \hat{\rho}^\circ], \tag{2.2.40}$$

and ω_l is the eigenvalue corresponding to eigenvectors $\hat{v}_l$ and $\hat{u}_l$. This method to resolve matrix by its eigenstates is often called *spectral representation* [67]. According to Eq. (2.2.30) the absorption coefficient can be calculated from $Im[\alpha_{\mu\mu}(\omega)]$, which reads:

$$Im\left[\alpha_{\mu\mu}(\omega)\right] = -\pi \sum_l \delta(\omega - \omega_l) (\hat{r}_\mu, \hat{v}_l) (\hat{u}_l, \hat{s}_\mu) . \tag{2.2.41}$$

For each eigenvalue, ω_l, we define the oscillator strength as:

$$F_{\mu\mu,l} \equiv - (\hat{r}_\mu, \hat{v}_l) (\hat{u}_l, \hat{s}_\mu) \pi \tag{2.2.42}$$

2.2.4 Batch representation

Io order to calculate the polarizability either by solving Casida's equation, Eq. (2.2.32), or by directly calculating Eq. (2.2.29), it is necessary to have an explicit representation for the response density matrix, for the super operator $\mathcal{L}$, and other operators or vectors that appear in these equations.

From the idempotence of the perturbed and unperturbed density matrices, it follows that:

$$\hat{\rho}' = \hat{\rho}^\circ \hat{\rho}' + \hat{\rho}' \hat{\rho}^\circ + \mathcal{O}(\hat{\rho}'^2). \tag{2.2.43}$$

By braketing both the left and right side of this equation with ground-state orbitals, it can be seen that:

$$\left\langle \psi_c^\circ | \hat{\rho}' | \psi_c'^\circ \right\rangle = \left\langle \psi_v^\circ | \hat{\rho}' | \psi_v'^\circ \right\rangle = 0, \tag{2.2.44}$$

which is to say that the matrix element of $\hat{\rho}'$ linking two occupied states or two empty states vanish. In other terms, the response density matrix can be expressed in the block form:

$$\hat{\rho}' \to \begin{pmatrix} 0 & \rho'_{vc} \\ \rho'_{cv} & 0 \end{pmatrix}, \tag{2.2.45}$$

where ρ'_{cv} and ρ'_{vc} are defined as:

$$\begin{aligned} \rho'_{cv} &= \left\langle \psi_c^\circ | \hat{\rho}' | \psi_v^\circ \right\rangle, \\ \rho'_{vc} &= \left\langle \psi_v^\circ | \hat{\rho}' | \psi_c^\circ \right\rangle. \end{aligned} \tag{2.2.46}$$

For this reason, the response density matrix can be resolved as:

$$\hat{\rho}'(\omega) = \sum_{vc} \left[\rho'_{cv}(\omega) \left| \psi_c^\circ \right\rangle \left\langle \psi_v^\circ \right| + \rho'_{vc}(\omega) \left| \psi_v^\circ \right\rangle \left\langle \psi_c^\circ \right| \right], \tag{2.2.47}$$

where:

$$\rho'_{cv}(\omega) = \rho'^*_{vc}(-\omega). \tag{2.2.48}$$

This is because in the time domain, the response density matrix is Hermitian, *i.e.* $\rho'_{cv}(t) = \rho_{vc}{}'^*(t)$.[9]

It can be seen that the effective dimension of the linear system, Eq. (2.2.25), is $2N_v(N - N_v)$, N being the size of the one-electron basis set. Using $\{\rho'_{vc}, \rho'_{cv}\}$ to represent the density matrix is called 'particle-hole' representation (PHR). The disadvantage of PHR is that a very large number of virtual states have to be explicitly calculated. This is a hard but still feasible task when using localized basis sets, but not affordable in the plane-wave based methods, where the number of basis is much larger. In order to avoid these disadvantages, a so-called *Batch Representation* (BR), borrowed from time-independent density-functional perturbation theory (DFPT) [68, 69], was introduced to represent the response density matrix [70, 71]. In Eq. (2.2.47) it is possible to implicitly sum up all the empty states and define two sets (batches) of orbital response functions:

$$\begin{cases} x_v(\mathbf{r}, \omega) \equiv \sum_c \rho'_{cv}(\omega) \psi_c^\circ(\mathbf{r}), \\ y_v(\mathbf{r}, \omega) \equiv \sum_c \rho'_{vc}(\omega) \psi_c^{\circ *}(\mathbf{r}). \end{cases} \tag{2.2.49}$$

[9] For keeping the neatness of notations, here we indicate the Fourier transform of a function just by the symbol of its argument.

Each of these two orbital sets, $\{x_v\}$ and $\{y_v\}$, has a number of orbitals equal to the number of occupied states. Each batch orbital is orthogonal to the occupied manifold. If we define two projection operators:

$$\begin{aligned} \hat{P} &= \sum_{v \in occ} |\psi_v^\circ\rangle \langle \psi_v^\circ| \\ \hat{Q} &= \hat{I} - \hat{P}, \end{aligned} \tag{2.2.50}$$

as the projectors onto the occupied- and empty-states manifolds, respectively, then the batch orbital $x_v(\mathbf{r})$ satisfies the relation:

$$\begin{aligned} \hat{P}x_v(\mathbf{r}) &= 0, \\ \hat{Q}x_v(\mathbf{r}) &= x_v(\mathbf{r}). \end{aligned} \tag{2.2.51}$$

In real space, the response density matrix reads:

$$\rho'(\mathbf{r}, \mathbf{r}', \omega) = \sum_v 2 \left[x_v(\mathbf{r}, \omega) \psi_v^{\circ *}(\mathbf{r}') + \psi_v^\circ(\mathbf{r}) y_v(\mathbf{r}', \omega) \right], \tag{2.2.52}$$

where factor 2 accounts for the double degeneracy of each occupied state in a non-spin polarized system. We also define a same-spin counterpart of Eq. (2.2.52) as:

$$\rho'_{\parallel}(\mathbf{r}, \mathbf{r}', \omega) = \sum_v \left[x_v(\mathbf{r}, \omega) \psi_v^{\circ *}(\mathbf{r}') + \psi_v^\circ(\mathbf{r}) y_v(\mathbf{r}', \omega) \right]. \tag{2.2.53}$$

It can be seen that $\rho'(\mathbf{r}, \mathbf{r}', \omega)$ is uniquely determined by these two sets of batch orbitals, hence we denote the response density matrix as:

$$\hat{\rho}' \xrightarrow{BR} \begin{pmatrix} \{x_v\} \\ \{y_v\} \end{pmatrix} \equiv \begin{pmatrix} X \\ Y \end{pmatrix}. \tag{2.2.54}$$

Using the batch representation (BR) the effective dimension of the problem grows from $2N_v(N - N_v)$ to $2N_vN$, but one obtains the great advantage of avoiding the need to compute empty states.

In order to express the dynamical polarizability, as in Eq. (2.2.29), in terms of the BR of the response density matrix, one must first give the BR of a general one-body quantum-mechanical operator, $\hat{A}$. To this end, let us consider the *vc* and *cv* components of this operator as: $\hat{A}' = \hat{P}\hat{A}\hat{Q} + \hat{Q}\hat{A}\hat{P}$, then it can be verified that :

$$Tr\left(\hat{A}^\dagger \hat{\rho}'\right) = Tr\left(\hat{A}'^\dagger \hat{\rho}'\right). \tag{2.2.55}$$

This means that for any quantity that can be calculated as Eq. (2.2.55), *e.g.* the molecular polarizability, Eq. (2.2.27), it is sufficient to just calculate the

vc and cv components of $\hat{A}$. Therefore we can define the BR of the operator $\hat{A}$ as [70]:

$$\begin{cases} a_v^x(\mathbf{r}) = \hat{Q}\hat{A}\psi_v^\circ(\mathbf{r}) = \sum_c \psi_c^\circ(\mathbf{r}) A_{cv}, \\ a_v^y(\mathbf{r}) = \left(\hat{Q}\hat{A}^\dagger\psi_v^\circ(\mathbf{r})\right)^* = \sum_c \psi_c^{o*}(\mathbf{r}) A_{vc}, \end{cases} \tag{2.2.56}$$

where A_{cv} and A_{vc} are the matrix elements of operator $\hat{A}$. Let us suppose two operators $\hat{A}$ and $\hat{B}$, if either of the two operators has vanishing vv and cc components, their inner product, defined in Eq. (2.2.16) reads:

$$\begin{aligned} \left(\hat{A}, \hat{B}\right) &= Tr\left(\hat{A}^\dagger \hat{B}\right) \\ &= \sum_{cv} \left(A_{cv}^* B_{cv} + A_{vc}^* B_{vc}\right) \\ &= \left(\langle a_v^x | b_v^x \rangle + \langle a_v^y | b_v^y \rangle\right), \end{aligned} \tag{2.2.57}$$

where $\{a_v^x, a_v^y\}$ and $\{b_v^x, b_v^y\}$ are the batch representation of the operator $\hat{A}$ and $\hat{B}$, respectively.

Within this definition one can give the BR to the Liouvillian operator $\mathcal{L}$, and the term $[\hat{r}, \hat{\rho}^\circ]$ in Eq. (2.2.29), or Eq. (2.2.31). The derivation is presented in Appendix A. Using these results the BR of the Liouvillian can be defined as:

$$\mathcal{L}\begin{pmatrix} X \\ Y \end{pmatrix} = \begin{pmatrix} \mathcal{D}+\mathcal{K} & \mathcal{K} \\ -\mathcal{K} & -\mathcal{D}-\mathcal{K} \end{pmatrix}\begin{pmatrix} X \\ Y \end{pmatrix}, \tag{2.2.58}$$

and Eq. (2.2.31) can be represented as:

$$\begin{pmatrix} \omega-\mathcal{D}-\mathcal{K} & -\mathcal{K} \\ \mathcal{K} & \omega+\mathcal{D}+\mathcal{K} \end{pmatrix}\begin{pmatrix} X \\ Y \end{pmatrix} = \begin{pmatrix} \left\{\hat{Q}\hat{r}\psi_v^\circ(\mathbf{r})\right\} \\ -\left\{\hat{Q}\hat{r}\psi_v^\circ(\mathbf{r})\right\} \end{pmatrix}, \tag{2.2.59}$$

where the action of the $\mathcal{D}$ and $\mathcal{K}$ on BR are defined as:

$$\mathcal{D}X = \left\{(\hat{H}_{KS}^\circ - \varepsilon_v) x_v(\mathbf{r})\right\}, \tag{2.2.60}$$

$$\mathcal{K}X = \left\{\hat{Q}\sum_{v'} \hat{K}_{vv'} x_{v'}(\mathbf{r})\right\}. \tag{2.2.61}$$

Here ε_v is the ground-state KS energy of the v-th orbital, and $\hat{K}_{vv'}$ is the operator whose coordinate representation is:

$$K_{vv'}(\mathbf{r}, \mathbf{r}') = 2\kappa(\mathbf{r}, \mathbf{r}')\psi_v^\circ(\mathbf{r})\psi_{v'}^\circ(\mathbf{r}'), \tag{2.2.62}$$

$\kappa(\mathbf{r}, \mathbf{r}')$ being the kernel of Hartree-plus-XC energy, and factor 2 accounts for the double degeneracy of occupied states.

It is convenient to perform a 45° rotation in the space of batch orbitals which gives us the *standard batch representation* (SBR) for the response orbitals [70]:

$$\begin{aligned} q_v(\mathbf{r}) &= \frac{1}{2}\left(x_v(\mathbf{r}) + y_v(\mathbf{r})\right), \\ p_v(\mathbf{r}) &= \frac{1}{2}\left(x_v(\mathbf{r}) - y_v(\mathbf{r})\right). \end{aligned} \tag{2.2.63}$$

After this rotation, we define $Q = \{q_v\}$ and $P = \{p_v\}$, then operator $\mathcal{L}$ reads:

$$\mathcal{L}\begin{pmatrix} Q \\ P \end{pmatrix} = \begin{pmatrix} 0 & \mathcal{D} \\ \mathcal{D}+2\mathcal{K} & 0 \end{pmatrix}\begin{pmatrix} Q \\ P \end{pmatrix}, \tag{2.2.64}$$

and Eq. (2.2.31) can be written as:

$$(\omega - \mathcal{L})\begin{pmatrix} Q \\ P \end{pmatrix} = \begin{pmatrix} \omega & \mathcal{D} \\ \mathcal{D}+2\mathcal{K} & \omega \end{pmatrix}\begin{pmatrix} Q \\ P \end{pmatrix} = \begin{pmatrix} 0 \\ \left\{\hat{Q}\hat{r}\psi_v^\circ(\mathbf{r})\right\} \end{pmatrix}. \tag{2.2.65}$$

For the convenience of the following discussion, we define:

$$\begin{aligned} u &= (\{\hat{Q}\hat{r}^\mu\psi_v^\circ\}, 0), \\ v &= -(0, \{\hat{Q}\hat{r}^\nu\psi_v^\circ\}), \end{aligned} \tag{2.2.66}$$

then Eq. (2.2.29) can be elegantly written as:

$$\alpha_{\mu\nu}(\omega) = \left(u, (\omega - \mathcal{L})^{-1}\cdot v\right). \tag{2.2.67}$$

2.2.5 Hybrid functionals

So far the formulation of operator $\mathcal{L}$ is built with regular, *i.e.* (semi-) local, XC functionals. In this subsection, we present the formulation of linearized TDDFT encompassing hybrid functionals.[10] In the hybrid functional expression, the operator $\mathcal{L}$ of hybrid functionals can be defined by adding an extra term to the original definition, Eq. (2.2.23):

$$\mathcal{L}\hat{\rho}' = \left[\hat{H}_{KS}^\circ, \hat{\rho}'(t)\right] + \left[\hat{V}'_{Hxc}[\hat{\rho}'(t)], \hat{\rho}^\circ\right] + \alpha\left[\hat{V}'_{exx}[\hat{\rho}'(t)], \hat{\rho}^\circ\right]. \tag{2.2.68}$$

Similarly to the ground-state formulation, Eq. (2.1.17), the linearization of the Fock-exchange operator is straightforward:

$$\begin{aligned} \int d\mathbf{r}' V'_{exx}[\hat{\rho}'_\parallel](\mathbf{r},\mathbf{r}')\psi_j^\circ(\mathbf{r}') &= -\int d\mathbf{r}' \frac{\rho'_\parallel(\mathbf{r},\mathbf{r}')\psi_j^\circ(\mathbf{r}')}{|\mathbf{r}-\mathbf{r}'|} \\ &= -\sum_{i\in occ}\int d\mathbf{r}' \frac{x_i(\mathbf{r})\psi_i^\circ(\mathbf{r}') + \psi_i^\circ(\mathbf{r})y_i(\mathbf{r}')}{|\mathbf{r}-\mathbf{r}'|}\psi_j^\circ(\mathbf{r}'). \end{aligned} \tag{2.2.69}$$

[10] This part was done in collaboration with Simon Binnie

In this equation $\rho'_{\parallel}(\mathbf{r},\mathbf{r}')$ is defined as in Eq. (2.2.53), it is essentially half of the usual expression $\rho'(\mathbf{r},\mathbf{r}')$ due to the spin-dependence of the exact exchange interaction. Functions $\{x_i\}$ and $\{y_i\}$ are batch orbitals of the response density matrix.

Using the definition of BR for a generalized operator, Eq. (2.2.56), we can derive the representation of the non-local contribution to the Liouvillian operator, *i.e.* the last term in Eq. (2.2.68), as:

$$\begin{aligned} V'^{x}_{exx,v}(\mathbf{r}) &= \hat{Q}\left[\hat{V}_{exx},\hat{\rho}^{\circ}\right]\psi^{\circ}_{v}(\mathbf{r}) = \hat{Q}\hat{V}_{exx}\psi^{\circ}_{v}(\mathbf{r}), \\ V'^{y}_{exx,v}(\mathbf{r}) &= \left(\hat{Q}\left[\hat{V}_{exx},\hat{\rho}^{\circ}\right]^{\dagger}\psi^{\circ}_{v}(\mathbf{r})\right)^{*} = -\left(\hat{Q}\hat{V}^{\dagger}_{exx}\psi^{\circ}_{v}(\mathbf{r})\right)^{*}. \end{aligned} \tag{2.2.70}$$

Expanding this equation with Eq. (2.2.69) it reads:

$$\begin{aligned} V'^{x}_{exx,v}(\mathbf{r}) &= -\hat{Q}\sum_{v'}\int d\mathbf{r}'\left[\frac{\psi^{\circ}_{v}(\mathbf{r}')\psi^{\circ}_{v'}(\mathbf{r}')}{|\mathbf{r}-\mathbf{r}'|}x_{v'}(\mathbf{r}) + \frac{\psi^{\circ}_{v}(\mathbf{r}')y_{v'}(\mathbf{r}')}{|\mathbf{r}-\mathbf{r}'|}\psi^{\circ}_{v'}(\mathbf{r})\right] \\ &\equiv \sum_{v'}\left[-\hat{K}^{1d}_{v,v'}x_{v'}(\mathbf{r}) - \hat{K}^{2d}_{v,v'}y_{v'}(\mathbf{r})\right], \\ V'^{y}_{exx,v}(\mathbf{r}) &= \hat{Q}\sum_{v'}\int d\mathbf{r}'\left[\frac{\psi^{\circ}_{v}(\mathbf{r}')x_{v'}(\mathbf{r}')}{|\mathbf{r}-\mathbf{r}'|}\psi^{\circ}_{v'}(\mathbf{r}) + \frac{\psi^{\circ}_{v}(\mathbf{r}')\psi^{\circ}_{v'}(\mathbf{r}')}{|\mathbf{r}-\mathbf{r}'|}y_{v'}(\mathbf{r})\right] \\ &= \sum_{v'}\left[\hat{K}^{2d}_{v,v'}x_{v'}(\mathbf{r}) + \hat{K}^{1d}_{v,v'}y_{v'}(\mathbf{r})\right]. \end{aligned} \tag{2.2.71}$$

This leads to the BR of $\mathcal{L}$ with hybrid functionals:

$$\mathcal{L}\begin{pmatrix} X \\ Y \end{pmatrix} = \begin{pmatrix} \mathcal{D}+\mathcal{K}-\alpha\mathcal{K}^{1d} & \mathcal{K}-\alpha\mathcal{K}^{2d} \\ -\mathcal{K}+\alpha\mathcal{K}^{2d} & -\mathcal{D}-\mathcal{K}+\alpha\mathcal{K}^{1d} \end{pmatrix}\begin{pmatrix} X \\ Y \end{pmatrix}. \tag{2.2.72}$$

Applying the rotation defined in Eq. (2.2.63), the SBR of $\mathcal{L}$ is given by:

$$\mathcal{L}\begin{pmatrix} Q \\ P \end{pmatrix} = \begin{pmatrix} 0 & \mathcal{D}-\alpha(\mathcal{K}^{1d}-\mathcal{K}^{2d}) \\ \mathcal{D}+2\mathcal{K}-\alpha(\mathcal{K}^{1d}+\mathcal{K}^{2d}) & 0 \end{pmatrix}\begin{pmatrix} Q \\ P \end{pmatrix}. \tag{2.2.73}$$

Similarly to the Liouvillian with semi-local XC potentials, this representation contains no explicit reference to the empty states. However, in the Liouvillian with hybrid functionals, three non-local V_{exx}-like operators (they are contained in $\mathcal{K}^{1d}$, $\mathcal{K}^{2d}$, and the term $\mathcal{D}$) must be applied to a given batch of orbitals. To apply a Fock-like operator to a batch of orbitals requires $2N_v^2$ fast Fourier transforms (FFTs), N_v being the number of occupied states. It is clear that for a reasonable sized system, the time taken to perform the FFTs will dominate the wall time for the calculation.

Whilst the implementation of the algorithms we will introduce in Sec. (2.3) themselves are largely unaffected by the inclusion of the EXX potential, with only the definition of the Liouvillian being modified, there is a secondary concern brought about the non-local exchange operator. In order to evaluate the right side of Eq. (2.2.65), the dipole operator has to be applied to the ground-state orbitals, which is an ill-defined operation in periodic boundary conditions (PBC) [69]. Only the projection of the resulting orbitals onto the empty-state manifold, however, is actually needed, and this difficulty can be solved by the tricks usually adopted in time-independent DFPT [20]. The latter basically amounts to transforming the action of the dipole operator into that of an appropriate current, which is well defined in PBC and whose implementation requires the evaluation of the commutator of the dipole with the unperturbed KS Hamiltonian [72]:

$$\langle \psi_c | \hat{r}_\mu | \psi_v \rangle = \frac{1}{\varepsilon_c - \varepsilon_v} \left\langle \psi_c | \hat{[} H^\circ_{KS}, r_\mu] | \psi_v \right\rangle , \tag{2.2.74}$$

While the local potentials commute with the dipole operator, in the case of hybrid functionals this commutator has a non-vanishing contribution from the non-local exchange operator, which, in a plane-wave (PW) representation, would require the computation of weakly converging sums in reciprocal space [73], and which has not been implemented yet. For finite systems, however, this difficulty is trivially overcome by restricting the range of the dipole operator to a limited region of space comprising entirely the molecular electronic charge-density distribution and not touching the boundary of the periodically repeated simulation cell, and by evaluating its action in real space:

$$\langle \psi_c | \hat{r}_\mu | \psi_v \rangle \approx \int_{cell} d\mathbf{r} r_\mu \psi^*_c(\mathbf{r}) \psi_v(\mathbf{r}), \tag{2.2.75}$$

Another limitation of the current implementation of hybrid functionals is that it is currently restricted to norm-conserving pseudo-potentials.

2.2.6 Tamm-Dancoff and double-pole approximations

Before introducing numerical algorithms to solve the Casida's equation, or the linear system, Eq. (2.2.29), we would like to introduce a very common approximation used in this type of calculation. Based on this approximation, we have created a simplified model in order to obtain some important features of the TDDFT spectra.

Tamm-Dancoff approximation

Some of the algorithmic hurdles that hinder the way to the computation of the spectrum are due to the non-Hermitian character of the Liouvillian

super-operator, see Eq. (2.2.58). The special form of the Liouvillian, known in the literature as the form of an *Random-phase Approximation (RPA) Hamiltonian* [74], can be forced to be Hermitian by taking away the term $\pm\mathcal{K}$ in the off-diagonal elements. This gives rise to the Tamm-Dancoff approximation (TDA), and Eq. (2.2.59) can be reduced as:

$$(\omega - \mathcal{D} - \mathcal{K})\, X = \{\hat{Q}\hat{r}\psi_v^\circ(\mathbf{r})\}. \tag{2.2.76}$$

Respectively, the Casida's equation can be written as:

$$\mathcal{L}^{TDA} X \equiv (\mathcal{D} + \mathcal{K})\, X = \omega X. \tag{2.2.77}$$

The dimension of these two equations is half that of the original one. What is more important, since they are Hermitian equations, many methods invented for ground-state Hamiltonian can be applied to the time-dependent problem in a similar way. The TDA has been known for a long time in nuclear physics, and it is also often used in time-dependent Hartree Fock (TDHF) and TDDFT calculation [75, 76].

Independent-particle and single-pole approximation

By ignoring interaction effects and treating electrons as independent particles, we set $\mathcal{K} = 0$ even in the diagonal elements, then Eq. (2.2.77) gives:

$$\mathcal{D}X = \left\{(\hat{H}_{KS}^\circ - \varepsilon_v)x_v(\mathbf{r})\right\} = \omega X. \tag{2.2.78}$$

The eigenvalue of this equation is simply the energy difference of two KS orbitals, $\omega_{cv}^{KS} = \varepsilon_c - \varepsilon_v$, and the corresponding eigenvector is:

$$X_{cv}^{KS} = \begin{pmatrix} 0 \\ \vdots \\ \psi_c(\mathbf{r}) \\ \vdots \\ 0 \end{pmatrix} \leftarrow v\text{–}th \text{ element} \tag{2.2.79}$$

The corresponding oscillator strength can be calculated by Eq. (2.2.42). The BR of $\hat{r}$ and $\hat{s}$ is given by (only X component since we are using TDA):

$$\begin{aligned} \hat{r} &\xrightarrow{BR} \{\hat{Q}\hat{r}\psi_v^\circ(\mathbf{r})\}\ , \\ \hat{s} = -[\hat{r}, \rho^\circ] &\xrightarrow{BR} \{-\hat{Q}\hat{r}\psi_v^\circ(\mathbf{r})\}\ . \end{aligned} \tag{2.2.80}$$

Using the definition of the inner product for the BR, Eq. (2.2.57), it reads:

$$\begin{aligned} (\hat{r}, \hat{v}) = (\hat{r}, X_{cv}^{KS}) &= \langle\psi_v^\circ|\hat{r}|\psi_c^\circ\rangle\,, \\ -(\hat{u}, \hat{s}) = -(X_{cv}^{KS}, \hat{s}) &= \langle\psi_c^\circ|\hat{r}|\psi_v^\circ\rangle\,. \end{aligned} \tag{2.2.81}$$

At the end, the oscillator strength of the KS transition is given by: $F_{cv}^{KS} = |R_{cv}|^2 \pi$, where R_{cv} reads:

$$R_{cv} = \langle \psi_c^\circ | \hat{r} | \psi_v^\circ \rangle \,. \tag{2.2.82}$$

The absorption spectrum obtained with this approximation is often called KS spectrum [76], which is defined as:[11]

$$\kappa^{KS}(\omega) = \omega \sum_{cv} |R_{cv}|^2 \, \pi \delta(\omega - \omega_{cv}). \tag{2.2.83}$$

Though its simplicity, and clear physical image, this independent-particle approximation is too rough to give the correct excitation properties. Using LDA, the excitation energy obtained with this method is usually significantly lower than the experimental value [77].

In the single-pole approximation (SPA) [111, 112], the interaction effects are treated by the first-order perturbation theory for the non-degenerate system, and the eigenvalues are given as:

$$\omega_{cv}^{SPA} = \omega_{cv}^{KS} + K_{cv,cv}, \tag{2.2.84}$$

where $K_{cv,cv}$ is the diagonal element of the interaction term $\mathcal{K}$, defined as:

$$K_{cv,cv} = \int d\mathbf{r} d\mathbf{r}' \psi_v^\circ(\mathbf{r}) \psi_c^\circ(\mathbf{r}) \kappa_{Hxc}(\mathbf{r}, \mathbf{r}') \psi_c^\circ(\mathbf{r}') \psi_v^\circ(\mathbf{r}'), \tag{2.2.85}$$

$\kappa_{Hxc}(\mathbf{r}, \mathbf{r}')$ being the Hartree-plus-XC kernel. In the SPA, all the eigenvectors, as well as the oscillator strength, are the same as in the KS approximation. Despite the simplicity of this approximation, it gives significant improvement to the excitation energies [77], but it can be used only when the eigenvalues of the full interacting matrix, Eq. (2.2.77), are well separated.

Double-pole approximation

When two KS poles are very close, the perturbation theory for degenerate states should be used. We consider a fictitious system with only two occupied states and one empty state.[12] The ground-state of this system can be described by three wavefunctions: ψ_1° and ψ_2° for occupied states, and ψ_c°

[11] In practice, the δ function is replaced by some broadening functions, such as the Gaussian function or Cauchy distribution function.

[12] This can be seen as a real system where the two highest occupied molecular orbitals (HOMO) and the lowest un-occupied molecular orbital (LUMO) are well separated from other states.

for the empty state. Within the TDA, the response density matrix can be completely determined by two parameters:

$$\hat{\rho}' = x_1 \left|\psi_c^\circ\right\rangle \left\langle\psi_1^\circ\right| + x_2 \left|\psi_c^\circ\right\rangle \left\langle\psi_2^\circ\right|, \tag{2.2.86}$$

where:

$$\begin{aligned} x_1 &= \left\langle\psi_c^\circ|\hat{\rho}'|\psi_1^\circ\right\rangle, \\ x_2 &= \left\langle\psi_c^\circ|\hat{\rho}'|\psi_2^\circ\right\rangle, \end{aligned} \tag{2.2.87}$$

Hence Eq. (2.2.77) for this system reads:

$$\begin{pmatrix} \varepsilon_c - \varepsilon_1 + K_{11} & K_{12} \\ K_{21} & \varepsilon_c - \varepsilon_2 + K_{22} \end{pmatrix} \begin{pmatrix} x_1 \\ x_2 \end{pmatrix} = \omega \begin{pmatrix} x_1 \\ x_2 \end{pmatrix} \tag{2.2.88}$$

where K_{ij} is defined as:

$$K_{ij} = K_{ji} = \int d\mathbf{r}d\mathbf{r}'\psi_i^\circ(\mathbf{r})\psi_c^\circ(\mathbf{r})\kappa_{Hxc}(\mathbf{r},\mathbf{r}')\psi_c^\circ(\mathbf{r}')\psi_j^\circ(\mathbf{r}'), \tag{2.2.89}$$

which indicates the interaction between two KS transitions.

Equation(2.2.88) can be discussed in two extreme situations. First when the difference of the diagonal elements is much larger than the off-diagonal elements:

$$|(\varepsilon_c - \varepsilon_1 + K_{11}) - (\varepsilon_c - \varepsilon_2 + K_{22})| \gg |\mathcal{K}_{12}|. \tag{2.2.90}$$

This gives exactly the same result as the SPA, Eq. (2.2.84), hence we call it single-pole extreme. In this situation, the KS transition energy is shifted by the diagonal element of $\mathcal{K}$, while the transition strength is not affected. On the other side, there is a so called double-pole extreme [78], in which the diagonal terms are equal:

$$(\varepsilon_c - \varepsilon_{v1} + K_{11}) = (\varepsilon_c - \varepsilon_{v2} + K_{22}) = \omega_0, \tag{2.2.91}$$

then Eq. (2.2.88) reads:

$$\begin{pmatrix} \omega_0 & K_{12} \\ K_{12} & \omega_0 \end{pmatrix} \begin{pmatrix} x_1 \\ x_2 \end{pmatrix} = \omega \begin{pmatrix} x_1 \\ x_2 \end{pmatrix}. \tag{2.2.92}$$

The eigenvalues of this equation read:

$$\begin{aligned} w_a &= w_0 - K_{12}, \\ w_b &= w_0 + K_{12}, \end{aligned} \tag{2.2.93}$$

and their respective eigenvectors are:

$$\begin{aligned} X_a &= (\frac{\sqrt{2}}{2}, -\frac{\sqrt{2}}{2}), \\ X_b &= (\frac{\sqrt{2}}{2}, \frac{\sqrt{2}}{2}). \end{aligned} \tag{2.2.94}$$

Using the BR, the response density matrix in this model can be written as:

$$\hat{\rho}' \xrightarrow{BR} \begin{pmatrix} x_1\psi_c(\mathbf{r}) \\ x_2\psi_c(\mathbf{r}) \end{pmatrix}. \tag{2.2.95}$$

Following the similar calculation to Eq. (2.2.79) $\sim$ Eq. (2.2.82), the corresponding oscillator strength reads: $|x_1R_{1c} + x_2R_{2c}|^2\pi$. Hence for transition a and b, there are:

$$\begin{aligned} F_a &= \frac{\pi}{2}|R_{1c} - R_{2c}|^2, \\ F_b &= \frac{\pi}{2}|R_{1c} + R_{2c}|^2. \end{aligned} \tag{2.2.96}$$

Two main characters can be seen from Eq. (2.2.93) $\sim$ Eq. (2.2.96). The first is that the energy of two KS transitions are splitted due to the interaction. The other important feature is that excitations are not any more one-to-one correspondent to KS transitions. Instead, each eigenvector is the mixture of two KS transitions. An interesting inference that one could notice from Eq. (2.2.96) is that, if R_{1c} is large but R_{2c} is very small, the resulting two excitations have almost the same oscillator strength, equal to the average of the two KS transitions. This phenomenon occurs only when the interaction between two poles is taken into account.

In order to illustrate this phenomenon, we suppose a system where $\varepsilon_c - \varepsilon_1 = 1.0$ eV and $\varepsilon_c - \varepsilon_2 = 1.2$ eV. Respectively, $R_{1c} = 8$ and $R_{2c} = 1$. For the case of single-pole extreme, we suppose $K_{11} = K_{22} = 0.5$ eV, and $K_{12} = K21 = 0$; instead for the double-pole extreme, we suppose $K_{11} = 0.5$ eV, $K_{22} = 0.3$ eV, and $K_{11} = K_{22} = 0.2$ eV. The resulting KS spectra and interacting spectra are presented in Fig. (2.1).

The real situation is often between these two extremes. To illustrate the transition from the single-pole extreme to the double-pole extreme, we define parameter W, which equals to the ratio between K_{12}, and the difference of diagonal elements in Eq. (2.2.88):

$$W = \frac{K_{12}}{(\varepsilon_1 - K_{11}) - (\varepsilon_2 - K_{22})}. \tag{2.2.97}$$

Here we use $R_{1c} = 2$ and $R_{2c} = 1$, F_a and F_b can be plotted as the function of W, see Fig. (2.2). It can be seen that when $W = 0$ the single-pole extreme applies, where transition a has high strength and the oscillator strength of transition b is weak. When the value of W decreases, at the beginning F_a goes up and F_b goes down, and to a certain point F_b totally disappears and F_a reaches its maximum. After this point, F_a starts to decrease and F_b increases. At the end, their limit values are just like in the double-pole extreme. On the other side, if W is positive, F_a immediately decreases and

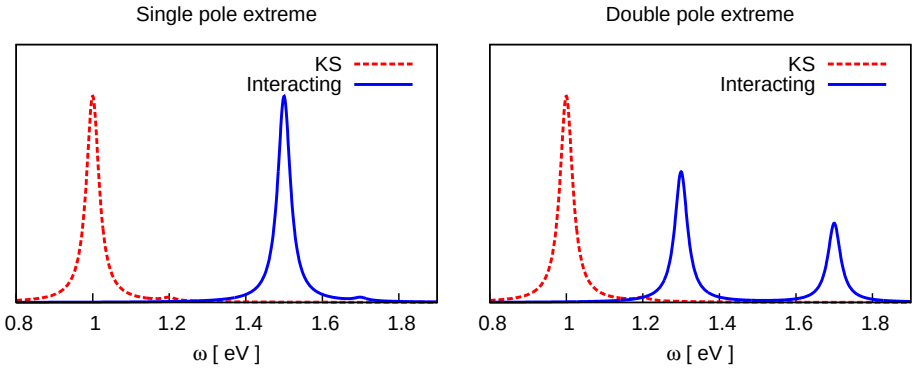

Figure 2.1: In the double-pole extreme the oscillator strength of two KS transitions are shared by two TDDFT transitions due to the interaction, therefore one dark transition turns to be bright.

F_b increases, at a certain point they have equal values. The limit values at the positive side of this plot are the same as the negative side, but with the oscillator strength of F_a and F_b swapped. It can also be noticed that the total oscillator strength is always conserved during the transition between the single-pole extreme to the double-pole extreme.

The double-pole approximation reproduces an important character of TDDFT spectrum caused by the interaction between two KS transitions. The same idea can also be generalized to the n-pole approximation, where the linear combination of a few KS transitions describes the excitation in the TDDFT spectrum. Later in this thesis, we will see that the double-pole effects are crucial to understand the difference between the spectra of several types of anthocyanins.

2.3 Numerical implementation

In this section we focus on two different numerical algorithms. First we adopt a newly proposed algorithm to solve the Casida's equation. This algorithm is an extension of the Davidson method in the ground-state Hamiltonian problem, to deal with Liouvillian problem. Another quite different approach, which directly solves the linear equation, Eq. (2.2.29), is also introduced. In this approach, we have applied a recently introduced pseudo-Hermitian Lanczos algorithm [51], which shows better efficiency and stability with respect to the bi-orthogonalization Lanczos algorithm [70].

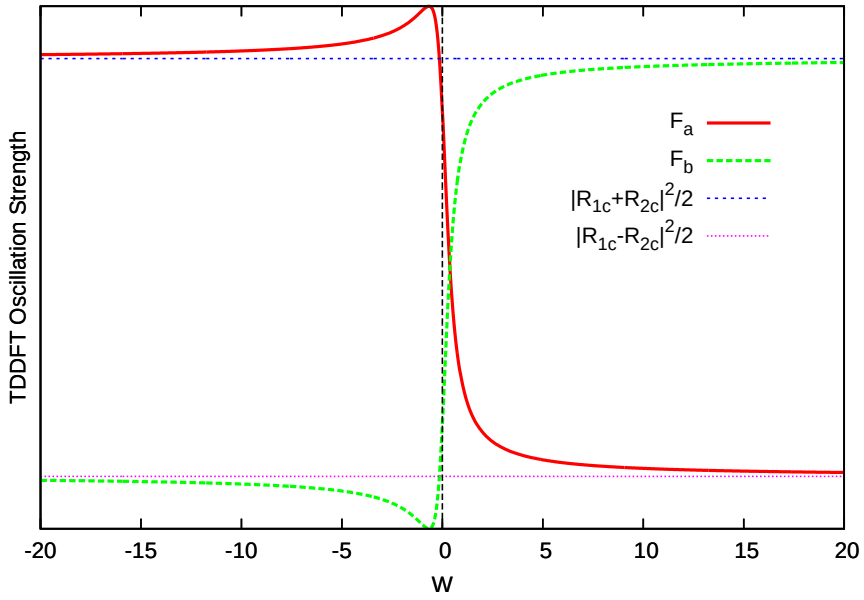

Figure 2.2: The TDDFT oscillator strength of excitation a and b as a function of W.

2.3.1 Davidson diagonalization

There are a number of problems where one is interested in only a few eigen-triplets of Liouvillian matrix.[13] These include the computation of excited-state properties, such as *e.g.* forces in higher Born-Oppenheimer surface [79], or systems whose dynamical response functions can be satisfactorily represented by a few eigen-triplets. The eigenvalue equation for Liouvialian super-operator has been formulated in terms of the Casida's equation in Sec. (2.2.3).

For a matrix with reasonably small size (within a few thousands), it is straightforward to compute its eigenvectors and eigenvalues, using standard matrix decomposition (also called matrix factorization) techniques [80, 81]. This task becomes extremely difficult when its dimension grows lager since the computational complexity of most the super-matrix factorization methods scales as $O(N^3)$. The dimension of operator $\mathcal{L}$ is $2N_v(N-N_v)$, or $2N_vN$, N being the dimension of the basis set, in the electron-hole or batch representations respectively. To give an estimation, if we consider anthocyanin molecules, which will be studied in this thesis, as an example, the system

[13] Analogous to the eigen-pair of a Hermitian matrix, the eigenvalue, left and right eigenvectors of a non-Hermitian matrix make up its eigen-triplet.

has about 100 occupied bands, and a reasonable choice of supercell and energy cutoff leads to $N_{PW} \approx 70,000$.[14] In TDDFT applications sometimes we need to deal with even larger systems, which makes it impossible to solve the Casida's equation directly, or even to store the matrix representation of the Liouvillian.

Subspace methods are often used to overcome this difficulty. In these methods, the matrix is projected and the problem is solved in a rather small subspace (of dimension a few tens to a few thousands). The dimension of the subspace is then systematically increased until the desired quantities are converged. Among many different subspace methods, characterized by different algorithms to construct the subspace, we focus on the Davidson method because of its fast convergence.

The Davidson algorithm was first formulated to solve large Hermitian eigen-problems [82, 83], such as in ground-state Hamiltonian diagonalization. Later it was employed also for TDDFT problem with TDA [75], where the Liouvillian operator is constructed to be Hermitian (see Sec. (2.2.6)). The extension to encompass the RPA matrices was further extended for the general response calculation [84, 85], and then generalized in a so-called *representation independent* formulation [86] that is similar in spirit to our batch representation. In this subsection, we first introduce the ordinary Davidson algorithm for Hermiatian matrices, and then a modified version is presented in order to solve the non-Hermitian Liouvillian problem. This new Davidson-like method has been implemented in the QUANTUM ESPRESSO package as `turbo_davidson`. In Appendix C, we also present a user's guide for this new application.

Davidson algorithm for Hermitian matrices

For the sake of clarity, let us suppose to compute only one lowest-lying eigenpair of a Hermitian matrix H. Starting from a trial eigenvector, v_1, which we suppose to be normalized, $(v_1, v_1) = 1$, and the corresponding estimate for the eigenvalue, $\varepsilon_1 = (v_1, Hv_1)$, one iteratively builds a reduced basis set according to the following procedure. One first defines the residual of the current estimate of the eigenvector as:

$$r = (H - \epsilon_1)v_1, \tag{2.3.1}$$

and then appends it to the current basis set upon orthonormalization. In practice, before this step is performed, the residual vector is *preconditioned*,

[14] In this thesis, the supercell is chosen to be $20 \times 20 \times 12$ $\mathring{A}^3$, and the energy cutoff is 25 Ry.

i.e. multiplied by a suitably defined matrix, G: $r \leftarrow Gr$. Here G is a $n \times n$ matrix, n being the dimension of matrix H, chosen in such a way as to speed up convergence. For an arbitrary matrix H, the choice of G is not very straightforward. However, in many practical situations, H is a diagonally dominant matrix, for which a very simple form of G can be adopted:

$$G = (\mathrm{diag}(H) - \varepsilon_1)^{-1}, \tag{2.3.2}$$

where $\mathrm{diag}(H)$ denotes the diagonal part of matrix H.

Once the basis has been thus enlarged, H is diagonalized in the subspace spanned by it, the lowest-lying eigenvector is elected to be the new trial vector, and the procedure is repeated until convergence is achieved (typically, $|r|$ smaller than a preassigned threshold). When the dimension of the reduced basis set exceeds some preassigned value, the subspace is then reset.

Turbo-Davidson algorithm for Liouvillian problem

The extension of the Davidson method that we introduce in the following is designed to find several *interior* eigen-triplets for a RPA-like matrix:

$$L = \begin{pmatrix} 0 & B \\ A & 0 \end{pmatrix}. \tag{2.3.3}$$

For the specific Liouvillian equation that we are studying in this thesis, A and B are defined as in Eq. (2.2.64) for non-hybrid functional, or Eq. (2.2.73) for hybrid functional. Our algorithm is a variation of the one described in Sec.IIIB of reference [86], featuring a sorting process, that allows to target interior eigenstates (*i.e.* those that are closest in magnitude to a preassigned reference excitation energy, ω_{ref}) and a preconditioning step that significantly increases its performance.

Let L be a $2n \times 2n$ RPA matrix of the form of Eq. (2.3.3), its eigenvalue equation reads:[15]

$$L \begin{pmatrix} Q \\ P \end{pmatrix} = \begin{pmatrix} 0 & B \\ A & 0 \end{pmatrix} \begin{pmatrix} Q \\ P \end{pmatrix} = \begin{pmatrix} BP \\ AQ \end{pmatrix} = \omega \begin{pmatrix} Q \\ P \end{pmatrix}. \tag{2.3.4}$$

Equation (2.3.4) can be written equivalently as:

$$\begin{cases} BP &= \omega Q, \\ AQ &= \omega P, \end{cases} \tag{2.3.5}$$

[15] It has been demonstrated in Sec. (2.2.3) that the left eigenvector of a RPA matrix can be easily obtained from its corresponding right eigenvector.

or:

$$\begin{cases} (BA)Q & = \omega^2 Q, \\ (BA)^T P & = \omega^2 P. \end{cases} \tag{2.3.6}$$

This shows that the Q and P components of the right eigenvector of L are obtained as the conjugated right and left eigenvectors of the matrix product $C \equiv BA$, and the eigenvalue of L is the square root of the eigenvalue of C. Among many advantages of this new formulation, the most important one is that C is a diagonally dominant matrix, for which it is easy to find a preconditioner similar to Eq. (2.3.2).

In order for transition energies to be real, the eigenvalue of Eq. (2.3.6), ω^2, have to be real and positive, which is the case by virtue of the following lemma:

Lemma: The eigenvalues of the product of two Hermitian positive definite matrices, denoted as BA, are real and positive.

This lemma is easily demonstrated by noticing that the eigenvalues of BA are equal to those of the Hermitian positive definite matrix $\tilde{A} = B^{\frac{1}{2}} A B^{\frac{1}{2}}$.

In Eq. (2.3.6), both A and B are Hermitian matrix. The eigenvalues of B are the energy differences between empty and occupied states (always positive), so this matrix is positive definite. It is less straightforward to demonstrate this for matrix A. However, as discussed in reference [87], this matrix is usually positive definite apart from very rare cases, which is enough to ensure that excitation energies are real.

Let us suppose that one is interested in finding k eigen-triplets of Eq. (2.3.6) whose ω's are closest to a referenced energy, $\omega_{ref} > 0$. The subspace is defined in terms of an orthonormal basis, $\{w_i; i = 1, \cdots, m\}$. We define ${}^m W = [w_1, w_2, \cdots, w_m]$ as a $n \times m$ rectangular matrix, whose columns are basis vectors. The orthonormality condition reads:

$${}^m W^{\dagger m} W = {}^m I, \tag{2.3.7}$$

where ${}^m I$ is the $m \times m$ identity matrix. The Q and P components of the right eigenvector of Eq. (2.3.4) are obtained as the right and left eigenvectors of the matrix $C = BA$ (see Eq. (2.3.6)), respectively. Following the arguments given in the lemma above, in order to guarantee that the reduced eigenvalue problem has real eigenvalues, it is convenient to project, instead of the product matrix $C = BA$, its factors, A and B [88]. We define therefore the reduced matrix to be diagonalized as:

$${}^m C = {}^m B {}^m A, \tag{2.3.8}$$

where ${}^mA = {}^mW^\dagger \mathcal{A}^m W$ and ${}^mB = {}^mW^\dagger \mathcal{B}^m W$. Being interested in finding multiple interior eigen-triplets, the orthogonal basis sets is enlarged by appending to it the left and right residuals corresponding to the eigenvalues whose square roots are closest to a target reference eigenvalue, ω_{ref}. The residuals themselves are calculated and preconditioned from Eq. (2.3.5), rather than from Eq. (2.3.6). The action of the preconditioner on a batch of orbitals, $Q = \{q_v\}$, is defined as:

$$Gq = \{\hat{Q}\hat{g}(\varepsilon_v)q^v\}, \tag{2.3.9}$$

where $\hat{g}(\epsilon_v) = \Big(\mathrm{diag}(\hat{H}^\circ_{KS} - \epsilon_v - \omega_{ref})\Big)^{-1}$, and $\hat{Q}$ is the projector over the empty-states manifold, defined in Eq. (2.2.50), to satisfy the constraint that batch orbitals are orthogonal to all the occupied states. In practice, the unperturbed Hamiltonian $\hat{H}^\circ_{KS}$ can be substituted with the kinetic-energy operator, facilitating considerably the calculation of matrix G, without any appreciable degradation of the performances.

Algorithm box 1 summarizes the Davidson algorithm for the pseudo-Hermitian problem. To find k eigen-triplets, we usually start from $2k$ trial vectors (line 1). At each iteration basis vectors are first orthonormalized (line 3). The reduced matrix ${}^mC$ is generated (line 4) and then diagonalized (line 5). In order to target interior eigenvalues, the resulting eigen-triplets are sorted in order of ascending $|\bar{\omega}_i - \omega_{ref}|$ (line 6). For each one of the k eigen-triplets of reduced matrix ${}^mC$, one obtains an computed of the corresponding eigenvector in the full linear manifold (line 9) and the residuals are estimated using Eq. (2.3.5) (lines 10 to 12); convergence is finally tested, and the reduced basis set updated upone preconditioning of the residuals (see Eq. (2.3.9)), when appropriate (lines 17 and 20).

2.3.2 Pseudo-Hermitian Lanczos algorithm

In the last subsection we have introduced a Davidson-like subspace method to solve the Casida's equation. This method is nearly optimal to calculate a few independent transitions, but severe difficulties occur for very large systems where the density of transitions is very high, or in the continuous part of the spectrum of even small systems. Drawbacks mainly come from two aspects. One is simply because of the large number of transitions that have to be calculated. Usually both the time and the memory cost of the turbo-Davidson algorithm increase linearly with the number of transitions. The other reason is because when the density of transitions is very high, the efficiency of the preconditioner deteriorates and the convergence of the algorithm also becomes very slow. A so-called Liouville-Lanczos approach has been introduced by D. Rocca et al. as an efficient tool to calculate the

Algorithm 1 turbo-Davidson: Davidson-like algorithm for multiple interior eigenvalues of the Liouvillian.

Initialization: $m \leftarrow 2k$; ${}^{m}W \leftarrow [w_1, w_2, \cdots w_m]$;
repeat
  Orthonormalization: ${}^{m}W^{\dagger}{}^{m}W = {}^{m}I$;
  ${}^{m}A \leftarrow {}^{m}W^{\dagger}A^{m}W$; ${}^{m}B \leftarrow {}^{m}W^{\dagger}B^{m}W$; ${}^{m}C \leftarrow {}^{m}B^{m}A$;
  Solve: ${}^{m}C^{\dagger}\bar{p}_i = \bar{\omega}_i^2\bar{p}_i$ and ${}^{m}C\bar{q}_i = \bar{\omega}_i^2\bar{q}_i$;
  Sort $\{\bar{p}_i, \bar{q}_i, \bar{\omega}_i^2\}$ in ascending order of $|\bar{\omega}_i - \omega_{ref}|$;
  for $i = 1$ to k **do**
    if $(\{p_i, q_i, \omega_i^2\}$ is not converged) **then**
      Update the eigenvectors of C: $q_i \leftarrow {}^{m}W\bar{q}_i$; $p_i \leftarrow {}^{m}W\bar{p}_i$;
      Computer left and right residuals:
        $l_i \leftarrow Bp_i - (p_i, Bp_i)q_i$;
        $r_i \leftarrow Aq_i - (q_i, Aq_i)p_i$
      if $(|r_i| < \epsilon$ and $|l_i| < \epsilon)$ **then**
        p_i and q_i are converged;
      else
        if $(|r_i| > \epsilon)$ **then**
          $m \leftarrow m + 1$; $w_m \leftarrow Gr_i$;
        end if
        if $(|l_i| > \epsilon)$ **then**
          $m \leftarrow m + 1$; $w_m \leftarrow Gl_i$;
        end if
      end if
    end if
  end for
until (All the first k eigen-triplets are converged)

entire spectra for large systems [70, 89, 90]. In this approach, instead of solving individual eigen-triplets of $\mathcal{L}$, the dynamical dipole polarizability is directly calculated as the response to a given perturbation.

In the original work of D. Rocca, a Lanczos bi-orthogonalization algorithm (LBOA) was applied due to the non-Hermitian character of the Liouvillian operator. It is, however, well known that the LBOA may have stability problems and suffers from the possibility of a numerical break-down [91]. For this reason a pseudo-Hermitian Lanczos algorithm (PHLA) was introduced by M. Grüning et al. [51], which improves both the efficiency and the stability of the LBOA. In this section, we start from the introduction of the original LBOA, and then we present the PHLA and its implementation in Quantum ESPRESSO.

Lanczos bi-orthogonalization algorithm

According to Eqs. (2.2.66) and (2.2.67), the dynamical polarizability can be calculated as the off-diagonal matrix element of $(\omega - \mathcal{L})^{-1}$. The main challenge that remains in this formulation is to compute the inverse of a very big matrix, for which The LBOA was introduced [70, 89].

Suppose one wants to compute the quantity described by Eq. (2.2.67), in which u and v are vectors in an n-dimension linear space, and L, the Liouvillian, is an $n \times n$ matrix. Given a pair of vectors, u_1 and v_1 normalized by the condition $(u_1, v_1) = 1$ (although it is not strictly necessary, we assume that $u_1 = v_1 = v$), two sets of vectors are generated through the recursion illustrated in Algorithm box 2.

Algorithm 2 LBOA: Lanczos bi-orthogonalization algorithm.

$v_0 \leftarrow 0$; $\quad u_0 \leftarrow 0$
$v_1 \leftarrow v$; $\quad u_1 \leftarrow v$
$l \leftarrow 1$
repeat
  $\alpha_l \leftarrow (u_l, Lv_l)$
  $\bar{v} \leftarrow Lv_l - \alpha_l v_l - \gamma_l v_{l-1}$
  $\bar{u} \leftarrow L^\dagger u_l - \alpha_l u_l - \beta_l u_{l-1}$
  $\beta_{l+1} \leftarrow \sqrt{(\bar{u}, \bar{v})}$
  $\gamma_{l+1} \leftarrow \mathrm{sgn}(\bar{u}, \bar{v}) \times \beta_{l+1}$
  $v_{l+1} \leftarrow \bar{v}/\beta_{l+1}$; $\quad u_{l+1} \leftarrow \bar{u}/\gamma_{l+1}$
  $l \leftarrow l + 1$
until convergence or breakdown

Here β_{l+1} and γ_{l+1} are scaling factors for the bi-normalization:

$$(u_{l+1}, v_{l+1}) = 1, \tag{2.3.10}$$

One should notice that when $(\bar{u}, \bar{v}) = 0$, this bi-normalization can not be achieved. This leads to a *breakdown* of the LBOA [91], and the algorithm must be stopped. Though in practice an exact breakdown never occurs due to numerical round-off errors, quasi-breakdowns, *i.e.* $(\bar{u}, \bar{v}) \approx 0$, often show up. To the best of our knowledge the overall algorithm is rather robust with respect to quasi-breakdowns, however, their occurrence remains an unpleasant feature of the method and may be potentially harmful to the algorithm.

Let us now define:[16]

$$\begin{aligned} {}^{m}U &= [u_1, u_2, ..., u_m], \\ {}^{m}V &= [v_1, v_2, ..., v_m], \end{aligned} \tag{2.3.11}$$

which are two $n \times m$ rectangular matrices whose columns are the two sets of vectors generated by the LBOA. By construction these two sets of vectors are bi-orthogonal: ${}^{m}U^{\dagger m}V = {}^{m}I$, where ${}^{m}I$ is the $m \times m$ identity matrix.[17] In terms of them, the resolution of the identity reads:

$$I = \sum_{i=1}^{m} |v_i\rangle \langle u_i| . \tag{2.3.12}$$

By inserting this relation into Eq.(2.2.67), and noticing $v_1 = v$, one obtains:

$$\alpha(\omega) = \sum_{i=1}^{m} (u, v_i) \left(u_i, (\omega - L)^{-1} v_1\right) . \tag{2.3.13}$$

One important feature of the LBOA is that the oblique projection of L onto the bi-orthogonal bases, defined as: ${}^{m}T = {}^{m}U^{\dagger} L {}^{m}V$, is tridiagonal [92]:

$${}^{m}T = \begin{pmatrix} \alpha_1 & \gamma_2 & 0 & \dots & 0 \\ \beta_2 & \alpha_2 & \gamma_3 & 0 & \vdots \\ 0 & \beta_3 & 0 & \ddots & 0 \\ \vdots & 0 & \ddots & \ddots & \gamma_m \\ 0 & \dots & 0 & \beta_m & \alpha_m \end{pmatrix} , \tag{2.3.14}$$

where the matrix elements are obtained from the recursion in Algorithm 2. In Eq. (2.3.13), the scalar products can be calculated on the fly during the Lanczos recursion, while the matrix elements of the resolvent of the Liouvillian, $\left(u_i, (\omega - L)^{-1} v_1\right)$, are simply the $(i, 1)$ matrix elements of matrix $(\omega - {}^{m}T)^{-1}$. To see this, let us write the Lanczos recursion for the right vectors as:

$$L {}^{m}V = {}^{m}V {}^{m}T + \epsilon, \tag{2.3.15}$$

where ϵ is a remainder that can be neglected as the number of iterations grows large enough. Let us subtract $\omega {}^{m}V$ from both sides of Eq. (2.3.15),

[16] The resulting algorithm is described with details also, *e.g.*, in Chap. 7 of reference [92].

[17] In practice, due to the numerical round-off errors, this relation is often lost for large number of iterations, leading to the notorious loss-of-orthogonality problem of Lanczos-like method [91]. This problem often causes fictitious eigenstates in the eigenvalue problem, but as it will be demonstrated by numerical test in the next section, the calculation of spectrum is rather robust with respect to the loss of orthogonality.

and multiply the resulting equation by ${}^mU^\dagger(L-\omega)^{-1}$ on the left and by $({}^mT-\omega)^{-1}$ on the right. Using the relation ${}^mU^\dagger{}^mV = {}^mI$, the final result is: ${}^mU^\dagger(\omega-L)^{-1}{}^mV \approx (\omega-{}^mT)^{-1}$, whose $(i,1)$ matrix element is:

$$\left(u_i,(\omega-L)^{-1}v_1\right) \approx \left[(\omega-{}^mT)^{-1}\right]_{i1}. \tag{2.3.16}$$

Solving the inverse of the tridiagonal matrix on the right side of Eq. (2.3.16) is numerically very easy. Another important advantage of the tri-diagonality is that for calculating matrix ${}^mT$ one needs to store, only three pairs of vectors instead of all the basis vectors (as it is the case in the Davidson method). In the calculation of excited states, the size of a single basis vector can often be very large,[18] so it is important to store as less basis vectors as possible. A huge memory requirement is the main hindrance of many other methods. In some cases when we want to calculate large number of transitions for a very large system, Lanczos-like algorithm may turn out to be the best choice.

The construction of the matrix ${}^mT$, which is the dominant cost of the calculation, is independent of the frequency. For this reason the calculation of the spectrum is carried on in two steps. In the first step, the recursion described in Algorithm 2 is performed and the matrix ${}^mT$ is built, then in the second step Eq. (2.3.16) is solved. In order to calculate the spectrum for different energies, one can repeat only the second step which is computationally very inexpensive.

Pseudo-Hermitian Lanczos algorithm

A matrix M is said to be η-pseudo-Hermitian if there exists a non-singular matrix η such that $M = \eta^{-1}M^\dagger\eta$. It is easy to verify that a Hermitian matrix is also pseudo Hermitian (by letting $\eta = I$ in this definition). If η is a positive definite Hermitian matrix, it can be used as the metric of a linear space where the inner product is defined as:

$$\langle : \mid : \rangle_\eta = \langle : \mid \eta : \rangle, \tag{2.3.17}$$

where $\langle : \mid : \rangle_\eta$ is called the η-inner product, and $\langle : \mid : \rangle$ is the standard inner product. It can be verified that $M_{uv} = M^*_{vu}$, where $M_{uv} \equiv \langle u|Mb\rangle_\eta$, u and b being two arbitrary vectors in this linear space. To see this we use the definition of η-inner product, which gives $M_{ub} = \langle u|\eta M|v\rangle$. Considering the pseudo-Hermitian property of M, it reads: $\langle u|\eta M|v\rangle = \left\langle u|M^\dagger\eta|v\right\rangle = \left[\left\langle v|\eta^\dagger M|u\right\rangle\right]^*$. Taking into account that η is a Hermitian matrix, this expression finally leads to: $[\langle v|\eta M|u\rangle]^* = \left[\langle v|Mu\rangle_\eta\right]^* = M^*_{vu}$.

[18] See the estimation in Sec. (2.3.1)

In the most general form of an RPA Hamiltonian, represented in Eq. (2.3.3), it is easily seen that:

$$L = \sigma \bar{L}, \tag{2.3.18}$$

where

$$\sigma = \begin{pmatrix} 0 & 1 \\ 1 & 0 \end{pmatrix} \text{ and } \bar{L} = \begin{pmatrix} A & 0 \\ 0 & B \end{pmatrix}. \tag{2.3.19}$$

It can be seen that L is pseudo-Hermitian both respect to $\eta = \sigma$ and $\eta = \bar{L}$. In our case σ-pseudo-Hermitian would not help because σ is not positive definite, hence cannot be used to define the inner product. As we have discussed in Sec. (2.3.1), in most cases both A and B are positive definite matrix, and so is $\bar{L}$. Therefore, we can use $\bar{L}$ as the matric matrix for the linear space in which the $\bar{L}$-inner-product is defined as:

$$(u, v)_{\bar{L}} \equiv (v, \bar{L}u) \tag{2.3.20}$$

A complete set of vectors is said to be *pseudo-orthonormal* if they are orthonormal with respect to the $\bar{L}$ metric:

$$(v_i, v_j)_{\bar{L}} = \delta_{ij}. \tag{2.3.21}$$

The resolution of the identity reads in this case:

$$I = \sum_i \bar{L} \left|v_i\right\rangle \left\langle v_i\right| = \sum_i \left|v_i\right\rangle \left\langle v_i\right| \bar{L}. \tag{2.3.22}$$

By inserting this relation into Eq.(2.2.67), and noticing $v_1 = v$, one obtains:

$$\alpha(\omega) = \sum_{i=1}^{m} (u, v_i) \left(v_i, (\omega - \mathcal{L})^{-1} v_1\right)_{\bar{L}}. \tag{2.3.23}$$

Following Ref. [51], the matrix elements in Eq. (2.3.23) can be easily obtained via a generalized Hermitian Lanczos method where all the relevant scalar products are performed with respect to the $\bar{L}$ metric, as illustrated in Algorithm 3.

The following discussion are analogous to the discussion for the LBOA (see Eq. (2.3.14) $\sim$ Eq. (2.3.16)). The oblique projection of $\mathcal{L}$ onto the pseudo-orthonormal basis set is defined as: $T_{ij} = (v_i, Lv_j)_{\bar{L}}$, which reads:

$${}^{m}T = \begin{pmatrix} \alpha_1 & \beta_2^* & 0 & \dots & 0 \\ \beta_2 & \alpha_2 & \beta_3^* & 0 & \vdots \\ 0 & \beta_3 & \alpha_3 & \ddots & 0 \\ \vdots & 0 & \ddots & \ddots & \beta_n^* \\ 0 & \dots & 0 & \beta_n & \alpha_n \end{pmatrix}, \tag{2.3.24}$$

Algorithm 3 PHLA:Pseudo-Hermitian Lanczos algorithm.

$v_0 \leftarrow 0$
$v_1 \leftarrow v$
$l \leftarrow 1$
repeat
  $\beta_l \leftarrow \sqrt{(v_l, v_l)_{\bar{L}}} \leftarrow \sqrt{(\sigma v_l, L v_l)}$
  $v_l \leftarrow v_l/\beta_l$
  $\alpha_l \leftarrow (v_l, L v_l)_{\bar{L}} \leftarrow ((L v_l), \sigma(L v_l))$
  $v_{l+1} \leftarrow L v_l - \alpha_l v_l - \beta_l v_{l-1}$
  $l \leftarrow l + 1$
until convergence

where $\{\alpha_i\}$ and $\{\beta_i\}$ are obtained from the recursion in Algorithm 3. Different from the LBOA, in this case ${}^mT$ is a Hermitian matrix.

The scalar products in Eq. (2.3.23) can be calculated on the fly during the Lanczos recursion, while the matrix elements of the resolvent of the Liouvillian, $\left(v_i, (\omega - L)^{-1} v_1\right)_{\bar{L}}$, are simply approximated by the $(i, 1)$ matrix elements of matrix $(\omega - {}^mT)^{-1}$:

$$\left(v_i, (\omega - L)^{-1} v_1\right)_{\bar{L}} \approx \left[(\omega - {}^mT)^{-1}\right]_{i1} . \tag{2.3.25}$$

To see this, we define the $n \times m$ rectangular matrices, ${}^mV = [v_1, v_2, \cdots, v_m]$ and ${}^mU = [\bar{L} v_1, \bar{L} v_2, \cdots, \bar{L} v_m]$. Pseudo-orthonormality reads: ${}^mU^{\dagger m}V = {}^mI$, where ${}^mI$ is the $m \times m$ identity matrix. Then the demonstration of Eq. (2.3.25) is the same as that of Eq. (2.3.16).

Considering that one single column of the inverse of a tridiagonal matrix can be inexpensively calculated by solvine a tridiagonal linear system, as it is the case in the ordinary Hermitian or non-Hermitian Lanczos methods, we have all the ingredients for an accurate and efficient calculation of the generalized susceptibility, Eq. (2.2.67). The two main features of the PHLA that makes it stand out over the standard LBOA are that it requires half as many matrix-vector products and that, not relying on the left and right vectors that can occasionally be almost orthogonal to each other, it is not subject to quasi-breakdowns.

Optical sum rule

Optical susceptibilities satisfy many sum rules, among which the most fundamental one is probably the Thomas-Reiche-Kuhn [93], which connects the integral of the absorption coefficient of a molecular system to the number of

electron in it:

$$f = \sum_{\mu} Im \int d\omega \alpha_{\mu\mu}(\omega)\omega = \frac{3}{2} N_e \pi, \tag{2.3.26}$$

N_e being the number of electrons in the system. A remarkable feature of the Liouville-Lanczos approach to TDDFT is that the TRK sum rule is satisfied exactly when truncating the Lanczos recursion to any number of iterations [72]. But strictly speaking, the above equation only holds when electrons are subject to a local external potential. A violation of the sum rule should be expected when non-local (norm-conserving as well as ultra-soft) pseudopotentials are used.

2.4 Numerical performance

2.4.1 Davidson algorithm

We have chosen C_2H_4 as the molecule to test. The supercell was set as $12 \times 12 \times 18$ $bohr^3$. Ultra-soft pseudo-potential (USPP) [94, 95] with PBE functional was used with kinetic energy cutoff 25 Ry for the wavefunctions and 200 Ry for the density. The spectra have been broadened by adding a small imaginary part to the frequency: $\omega \to \omega + i\epsilon$, with $\epsilon = 0.01$ Ry.

A detailed description of the paremeters in the input of turbo-Davidson can be found in Appendix C. In this test, we used 10^{-4} Ry as the convergence threshold. We performed the calculation for three times with different reference energies: 0.4, 0.6, and 0.76 Ry, and for each reference energy, 5 eigenstates are calculated. For such a small system the spectrum can certainly be obtained by calculating many transitions at the same time. It has been carried on in this way in order to illustrate the use of multiple reference energy. For the LBOA, 1000 iterations have been performed for each polarization. The turbo-Davidson spectrum is compared with the LBOA spectrum and the result is displayed in Fig. (2.3). It can be seen that the new algorithm matches the LBOA result to a very high precision.

In reference [86] a similar diagonalization method was introduced, but without any preconditioning. In order to illustrate the importance of preconditioning, we have calcualted the lowest 5 eigenstates of C_2H_4, and in Fig. (2.4) we report the maximum residual, as a function of the number of Liouvillian builds with or without preconditioning. Two main features can be found from this plot. The first is that the curve without preconditioning increases at a certain point. This is because another eigenstate has been found. This kind of behavior can be very harmful to the convergence because the previous effort that has been paid in order to improve the old

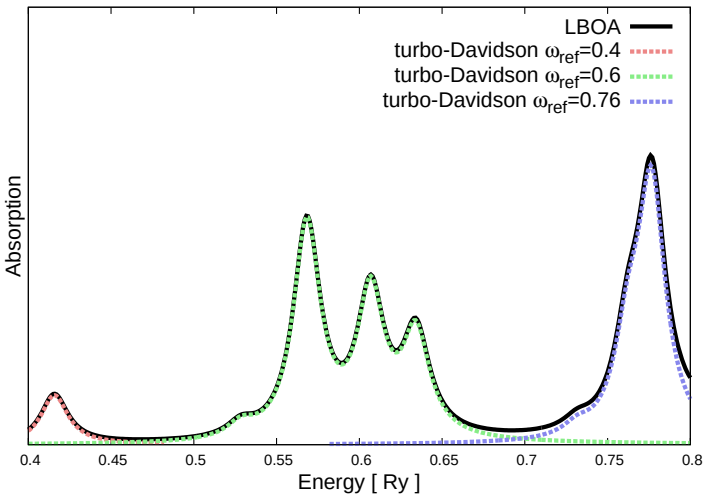

Figure 2.3: Spectra of C_2H_4 calculated by LBOA and turbo-Davidson with different reference energies.

eigenstate is wasted. It occurs often when the density of eigenstates is high, or the way to look for new vectors is not good enough. From the plot one can see that this does not occur when we are using preconditioning. The second feature is that without preconditioning the residual decreases exponentially (apart from the bump caused by new eigenstate), agreed with the result in reference [86]; while with preconditioning it decreases hyperexponentially which indicates very fast convergence of our new method.

In Appendix D we have derived that the error of the transition energy is proportional to the squared modulus of the residual and the error of the oscillator strength is proportional to the modulus of residual. This is a useful knowledge for us to decide the convergence threshold for the turbo-Davidson algorithm. This conclusion from analytical estimation has also been demonstrated by the numerical experiment. In Fig. (2.5) we have converge the calculation of C_2H_4 to a very high level in which the modulus of the residual is 10^{-5} and then illustrate the error of the transition energy and oscillator strength of the first transition.

Tests of turbo-Davidson algorithm on small molecules have shown great efficiency. It is also interesting and helpful to test the convergence speed for systems of different size, and see how the convergence is affected by the size of the system. This test has been done on a group of polycyclic aromatic hydrocarbon which can be formulated as $C_6H_6(C_4H_2)_n$. Their structures are illustrated in Fig. (2.6):

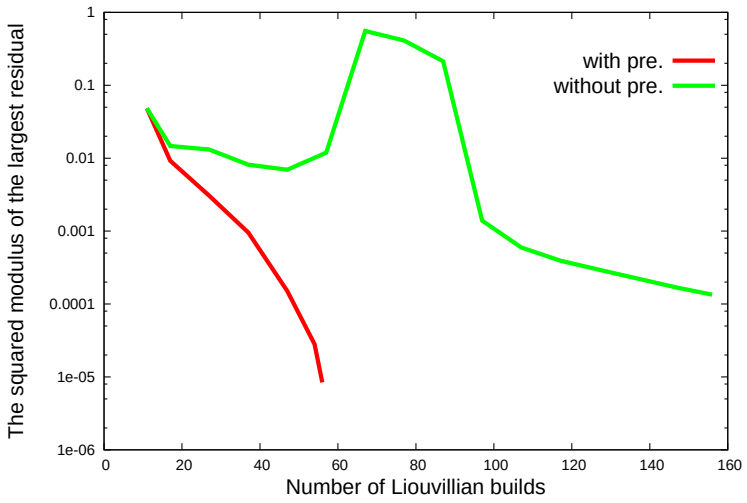

Figure 2.4: The number of Liouvillian builds versus the largest squared modulus of the residual vectors for 5 eigenstates of C_2H_4.

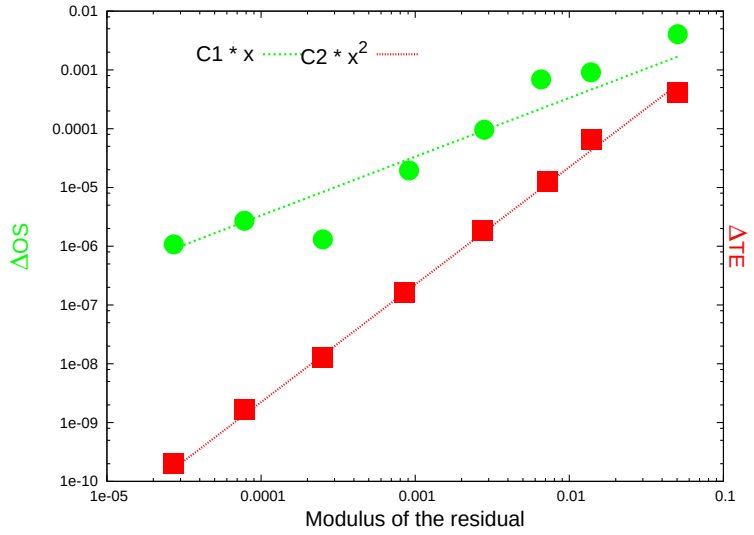

Figure 2.5: The error of oscillator strength (OS, green circle) and transition energy (TE, red square) versus the modulus of the residual for the first transition of C_2H_4. The green and red lines are fitting lines, in which $C1$ and $C2$ are two constants. It can be seen that ΔOS is proportional to the modulus while ΔTE is proportional to the squared modulus of the residual.

All the molecules are simulated in the same supercell ($80\times32\times20$ $bohr^3$). Their structures are first optimized with the same functionals (PBE) used

n	0	1	2	...
Mol			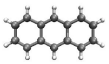	...

Figure 2.6: The structure of $C_6H_6(C_4H_2)_n$ for different n in the formula.

in the spectra calculation, and then the turbo-Davidson algorithm is used to calculate the first transition. The convergence threshold for the squared modulus is chosen to be 10^{-4}. The number of Liouvillian operations for each molecule is presented in Fig. (2.7) which shows that the convergence speed is independent with the size of the system. This means that for calculating the spectrum of a larger system, the increase of calculation cost comes only from the fact that applying each Liouvillian operator for a larger system is more expensive, but this cost scales in the same way as the ground-state calculation.

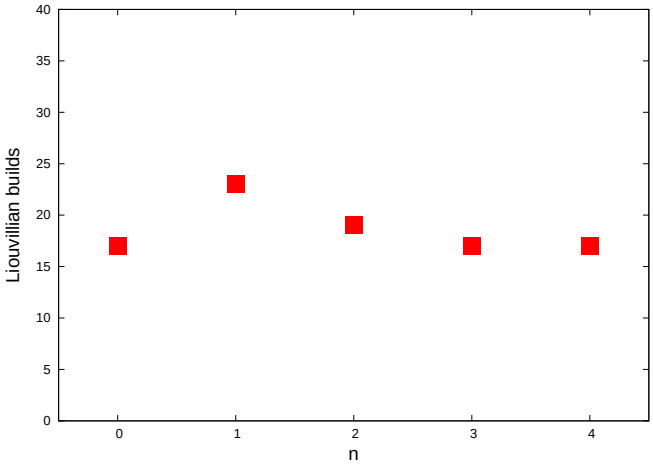

Figure 2.7: The number of Liouvillian builds to converge the first transition of $C_6H_6(C_4H_2)_n$.

2.4.2 Pseudo-Hermitian Lanczos algorithm

The PHLA has been used to calculate the same C_2H_4 molecule described in the last subsection. Its result has been compared with the LBOA, see Fig. (2.8). In both cases, 1000 Lanczos iterations are carried on for each polarization. But since the cost of the PHLA is only half of the LBOA for each iteration, the total cost for PHLA is only half as much as the LBOA case.

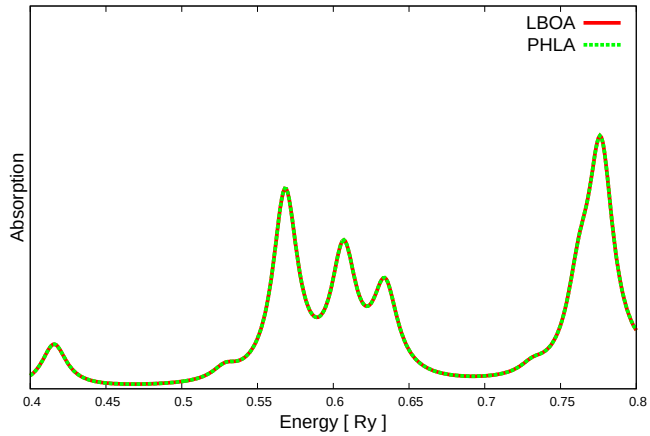

Figure 2.8: Comparing the spectra of C_2H_4 calculated by both the LBOA and the PHLA. Broadening parameter is chosen as 0.01 Ry for both algorithms.

As two methods give identical converged results, it is meaningful to compare their convergence speed. We have calculated the error of the energy of the first peak as the function of the iteration number. The results for both two methods are plotted it in Fig. (2.9). It is shown that in both methods, the energy error decreases exponentially. The PHLA method needs slightly more iterations to achieve the same level of precision (about a few tens). As discussed in Sec. (2.3.2), the PHLA method costs half with respect to the LBOA for each iteration, at the end PHLA will approximately increase the efficiency of LBOA by the fact of two.

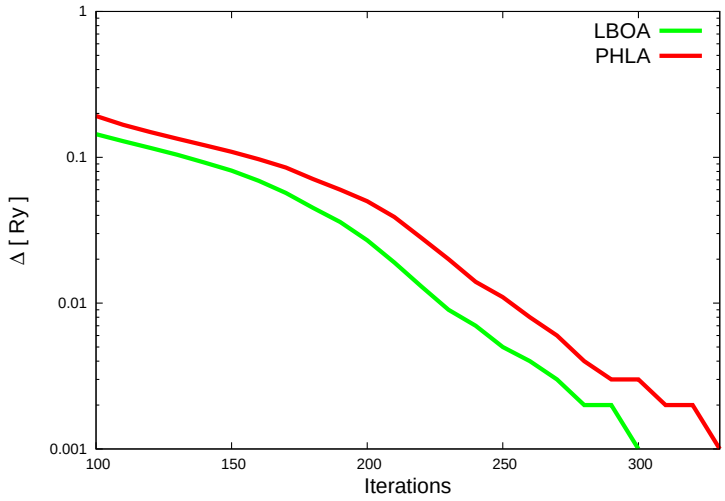

Figure 2.9: Convergence of the energy of the first peak of C_2H_4. The X-axis is the iteration number and Y-axis is the energy error.

In Dario Rocca's original work [70], a type of instability caused by the bi-orthogonality was introduced. This instability happens when the left and right vectors are close to orthogonal to each other. This is indeed the qauasi-breakdown introduced in Sec. (2.3.2). In practice, when the quasi-breakdowns occur, the β coefficients show unpleasant behaviors as the left side of Fig. (2.10). The test was performed with benzene molecule in a $20 \times 20 \times 12$ $bohr^3$ supercell. Norm-conserving pseudo potentials (NCPP) with energy cutoff 40 Ry were used. In Fig. (2.10) we see that for both methods β coefficients stay in a narrow range for most of the time. But for the LBOA case β sometimes deviates from this range due to the quasi-breakdown discussed above. The situation can be relieved by using larger supercell, but a few *jumping points* can often be observed even in a very large supercell. Fortunately to the best of our knowledge, the calculation of spectrum is rather robust, and we haven't found any proof that this kind of instability can be so fatal to spoil the spectra. The worst situation that has been met is when the spectra is calculated with extremely small brodening, some tiny but negative peaks may show up. But this kind of problems can be fixed by using larger broadening. Even though it is still an unpleasant feature of the LBOA. As a contrast, in PHLA algorithm the left and right vectors are the same, and a vector can never be orthogonal to itself, this kind of instability never occurs. As shown on the right side of Fig. (2.10), one can see that in the PHLA case no *jumping point* appears.

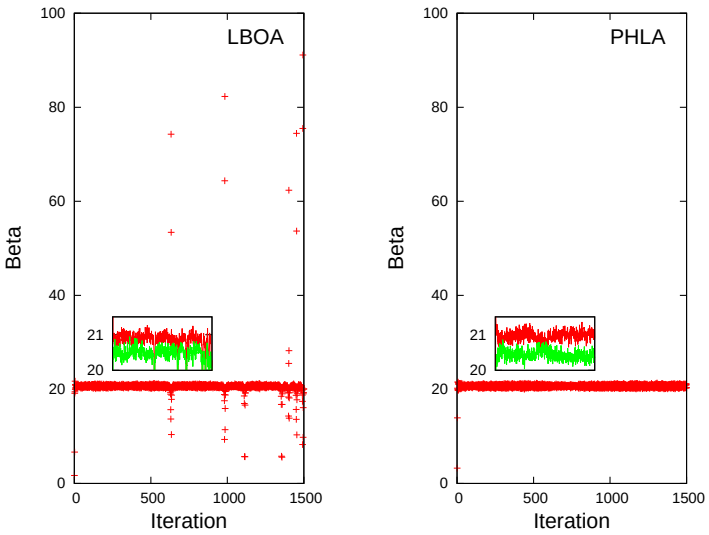

Figure 2.10: Beta coefficients of LBOA (*left*) and PHLA (*right*) algorithms. In the inset, the same data are shown on a different scale and with different colors for odd (red) and even (green) coefficients.

2.4.3 Comparing turbo-Davidson with turbo-Lanczos

In general Davidson can favor a certain eigenstates and has much faster convergence to individual eigenstates. Also the eigenvectors are obtained in Davidson method, so calculating other related quantities, such as the electron-hole pairs and the response charge density of a certain transition is easy and straightforward. However as a severe bottleneck of Davidson algorithm, every basis vector in this method has to be stored during the calculation, which leads to very large memory requirement. As a contrast, Lanczos method converges slower to individual eigenstates, but has advantages when the energy scale of interest is large, and the density of transitions is high. In Lanczos method, only three (three pairs in the case of LBOA) vectors need to be stored, so the requirement for the memory is much less with respect to Davidson method, making it the best approach for very large system. Among our two Lanczos methods, PHLA is more efficient and more stable than LBOA, so in the following part of the thesis, Turbo-Lanczos will always refer to PHLA unless it is explicitly indicated.

In order to compare the efficiency of turbo-Davidson and turbo-Lanczos for calculating anthocyanins' spectra, we have calculated the visible spectrum of cyanin, of which the result will be shown again and discussed with more details in the next chapter, here we use it only as a benchmark of the numerical performance. Cyanin contains 53 atoms with 85 occupied states. The calculation is performed with PBE functional, ultra-soft pseudo potential with the kinetic energy cutoff 25/200 Ry, and the size of the supercell is $20 \times 20 \times 12$ Å^3. The transition peaks are broadened with coefficient 0.001 Ry. The spectra are displayed in Fig. (2.11).

In the Davidson method, 15 eigenstates are calculated. The convergence of turbo-Davidson is very fast, the squared of the residual becomes smaller than 10^{-4} after 9 iterations, and the Liouvillian operator has been applied for 246 times. Since applying this operator is the dominant expense for the spectra calculation, it can be used as the benchmark for the speed of the convergence. In fact, with 64 cores on the `EURORA`[19] machine at `CINECA` [96], we are able to finish this calculation within 5 minutes.

As a comparison, Lanczos with 2000 iterations fails to give correct number of peaks and the transition energy. With 3000 iterations Lanczos is able to reproduce the general feature of the spectrum with acceptable precision. But the convergence of the higher energy spectrum is still not achieved, and the shoulder at 2.83 *ev* is missing. The shoulder starts to show up at 4000 iterations, and the spectrum at the visible range is finally converged

[19] Intel Xeon (Eight-Core SandyBridge) E5-2687W 3.10 GHz

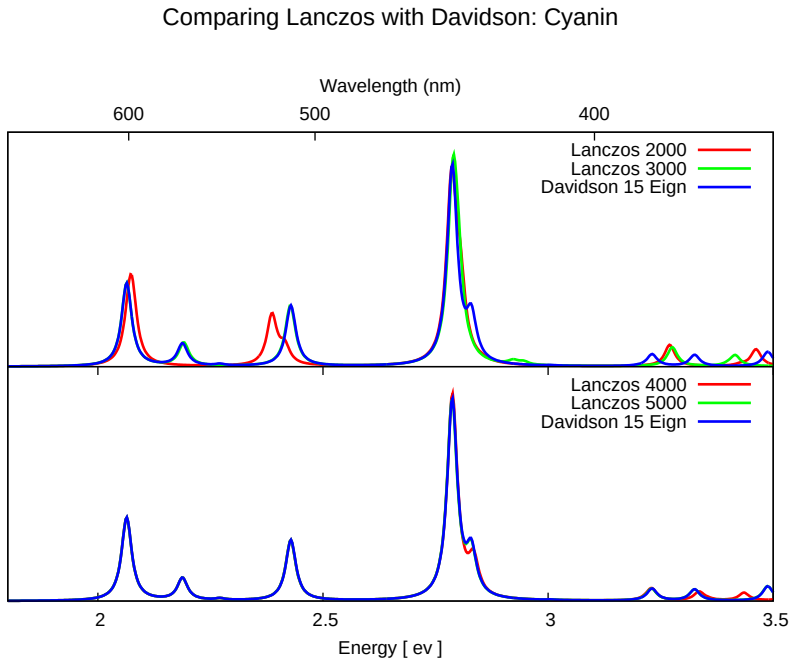

Figure 2.11: Comparing the numerical performance of Davidson and PHLA. The tested molecule is cyanin (85 bands).

at 5000 iterations. In this case the Liouvillian operator has been applied for 5000 times for each polarization, so the total number of Liouvillian builds is 15000. Compared with the 246 Liouvillian builds in turbo-Davidson we can see that in the case of calculating the spectrum of gas phase anthocyanins, turbo-Davidson is more efficient. However from the result of the comparison one can also see that even though Lanczos has slower convergence, its converged spectrum does not suffer a lot from the loss of orthogonality. It is consistent with the well known fact that the spectrum calculated with Lanczos is less sensitive to the loss of orthogonality than the eigenvalues [97, 91]. This is probably because the oscillator strength of these ghost eigenstates is usually very small.

The main reason why Davidson is more efficient for this case is because only a few eigenstates are responsible for the spectrum of anthocyanin in the visible range. As we have discussed before, Davidson-like method is nearly optimal for calculating a few eigenstates. However when the explicit solvent is considered in the spectra calculation, there are more than 450 bands in the system, and Davidson algorithm has difficulties dealing with the huge memory requirement. In that case Lanczos can be the only method that can overcome the memory bottleneck.

As the result of the discussion above, in this thesis we will use as default turbo-Davidson to calculate the spectra of anthocyanins in the gas phase, and Turbo-Lanczos to calculate the spectra in the solvated system.

2.4.4 Implementation of hybrid functionals

In Sec. (2.2.5) it has been discussed that calculating $\langle\psi_c|\hat{r}_\mu|\psi_v\rangle$ is not trivial for the non-local Fock-operator. Failing to calculate this term would not change the energy of peaks in the absorption spectrum, but affects the oscillator strength of each peak, hence the TRK sum rule would fail in that case. In order to have a better estimation of this term, we have used Eq. (2.2.75). To show the performance of the new method, we have calculated the integral of the spectra with both Eq. (2.2.74), neglecting the contribution of the Fock-operator, and Eq. (2.2.75) for three small molecules. In all these cases, molecules are located at the center of a $12 \times 12 \times 18$ $bohr^3$ supercell. The error between the actual integral and the f given by the TRK sum rule is defined as Δf, and the relative error is given by $\Delta f/f$. In Tab. (2.1) we present the relative error for both two methods. It can be seen that in the non-hybrid functional case, both methods can give very good results. But Eq. (2.2.74) tends to give too low integral for the PBE0 calculation. Instead Eq. (2.2.75) gives good results for both PBE and PBE0 calculation.

$\Delta f/f$	PBE		PBE0	
Molecule	Eq. (2.2.74)	Eq. (2.2.75)	Eq. (2.2.74)	Eq. (2.2.75)
CH_4	-0.006	0.000	-0.330	0.000
C_2H_4	-0.009	-0.003	-0.335	-0.018
CO	-0.044	-0.008	-0.306	-0.012

Table 2.1: Relative error of the spectrum integral with two different methods to calculate term $\langle\psi_c|\hat{r}_\mu|\psi_v\rangle$.

In order to test the implementation of hybrid functional in QUANTUM ESPRESSO, we have calculated the spectrum of cyanin with B3LYP with turbo-Davidson and compared it with the result obtained with Gaussian09. For turbo-Davidson, we have used norm-conserving pseudo potential with kinetic energy cutoff 60/240 Ry, and 80 Ry for the cutoff of Fock operator [98]. Eq. (2.2.75) is used to estimate term $\langle\psi_c|\hat{r}_\mu|\psi_v\rangle$. For Gaussian09, we have used the cc-pVTZ basis set. The spectra of both calculation are broadened with $\epsilon = 0.005$ Ry, and reported in Fig. (2.12), which shows excellent agreement between two methods.

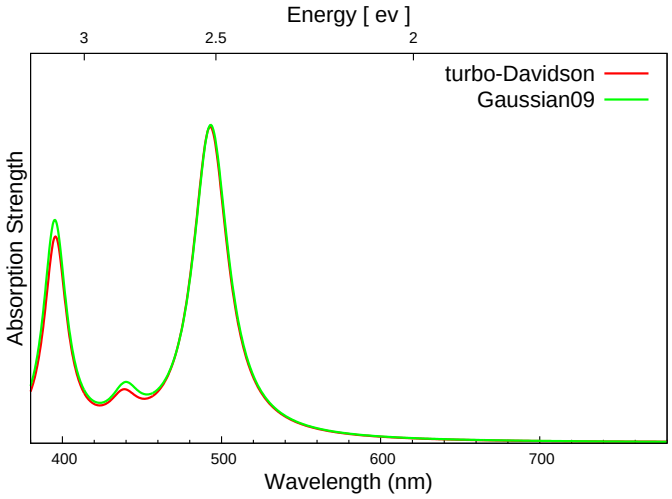

Figure 2.12: Comparing the absorption spectra of cyanin-B3LYP calculated by turbo-Davidson and Gaussian09.

Chapter 3

Optical properties and colors of Anthocyanins

In this chapter we study the optical properties of the six most common anthocyanins. We first characterize the molecules in the gas phase, and analyze the effects of different side groups on both their ground-state and optical properties. We then consider the dielectric and thermal effects induced by the presence of a surrounding solvent. In particular, we study the modification of the spectra and colors of anthocyanins induced by water, using an explicit solvent model. Our simulation is compared with experimental spectra and shows very good agreement.

3.1 Anthocyanins in the gas phase

As we have mentioned in Sec. (1.1), there are mainly four stable forms of anthocyanins. In this thesis we focus on the flavylium form, that is the most studied one in biological systems. In this study, we have selected the six most common anthocyanins formed in nature (see Fig. (1.2) for overview of their structures). All these molecules differ from each other by the side groups on the phenyl rings.

The geometry of six anthocyanins were first optimized in the gas phase with PBE functional using QUANTUM ESPRESSO. We used plane waves and ultra-soft pseudo potentials (USPP) with a kinetic energy cutoff of 25/200 Ry.[1] The molecule was located in a $20 \times 20 \times 12$ Å^3 supercell. Since the flavylium form of anthocyanin is the cation with 1 positive charge, the supercell was neutralized with a uniform negative charge background [46].

[1] Here and in the following the notation X/Y Ry will indicate a kinetic energy cutoff of X and Y Ry for the wavefunctions and charge-density distributions, respectively.

After the optimization of the structure, the turbo-Davidson algorithm was used to calculate their spectra in the visible range. We first calculated the spectra with PBE functionals. In order to understand the effects of the XC functional and to correct the well known deficiencies of DFT in reproducing the observed optical gaps, we re-simulated the spectra of anthoycanins, by using hybrid functionals such as PBE0 and B3LYP. For PBE0 we used norm-conserving pseudo potentials (NCPP) with a kinetic energy cutoff of 40/160 Ry, and for B3LYP we used NCPP with kinetic cutoff 50/200 Ry. A Lorentzian broadening of $\epsilon = 0.005$ Ry has been applied to all the spectra. The fifteen lowest-energy transitions were computed. A comparison with spectra previously obtained with `turbo_lanczos` algorithm confirms that 15 transitions are sufficient to completely characterize the spectral features in the visible range.

The spectra of all the six molecules calculated with the PBE are presented in Fig. (3.1), along with their simulated colors. For all molecules, the absorption edge is the visible range, in agreement with the observed color activity of these systems. Based on the spectral features (e.g. number and intensity of the peaks) we can classify these molecules in three groups. The first group (panel a) has two main absorption peaks around 450 and 500 nm. Molecules in the second group (panel b) have two strong peaks near 450 and 600 nm, and a third lower intensity contribution in between. The third group (panel c) is characterized by a single absorption peak between 530 and 570 nm. With the method discussed in Sec. (1.2), the observable colors of these anthocyanins can be simulated from their spectra, shown by the color squares in the figure.

The spectra with B3LYP and PBE0 are shown in Fig. (3.2) and Fig. (3.3), respectively, along with their simulated colors. The classification of 3 kinds of anthocyanins and the general shape of their respective spectra are not affected by the choice of functionals. However, there are generally two main changes in the spectra induced by hybrid functionals. First, the lowest-energy peaks are blue-shifted by about $50 \sim 100$ nm. This is due to the inclusion of the Fock-exchange contribution in the XC functional that leads to a larger gap and excitation energies with respect to PBE. The PBE0 spectra are slightly more blue-shifted than these of B3LYP ones. The second change concerns the relative intensity of two strong peaks in the first and the second groups. In the case of PBE, the peak at shorter wavelength has a higher intensity, while the opposite holds for B3LYP and PBE0. The blue-shifts of the absorption spectra increase the red components in the simulated colors, therefore these molecules express yellow and magenta colors when they are simulated with hybrid functionals.

In Fig. (3.4), we summarize the simulated colors for anthocyanins in

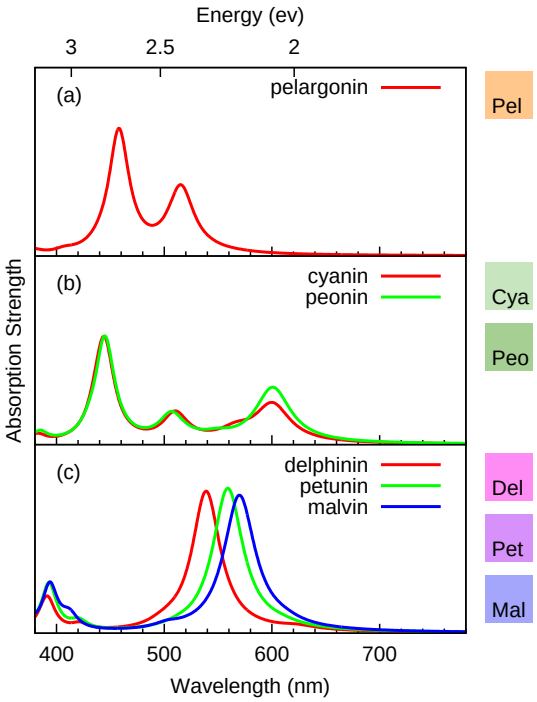

Figure 3.1: Absorption spectra (PBE) of anthocyanins and their simulated colors.

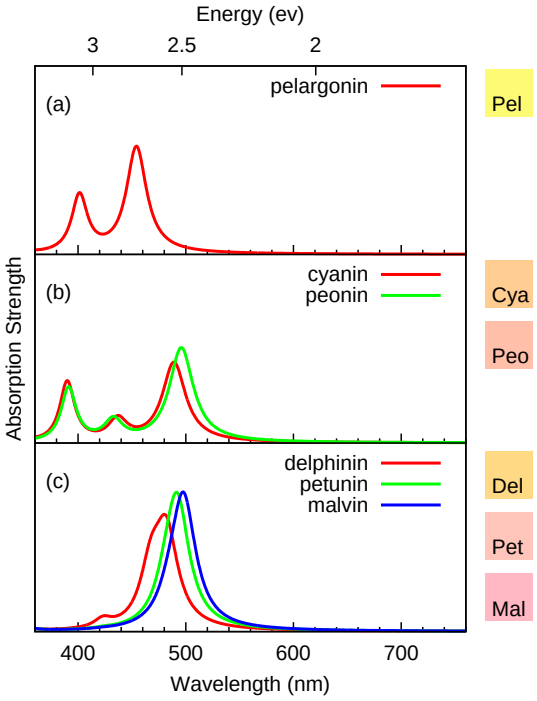

Figure 3.2: Absorption spectra (B3LYP) of anthocyanins and their simulated colors.

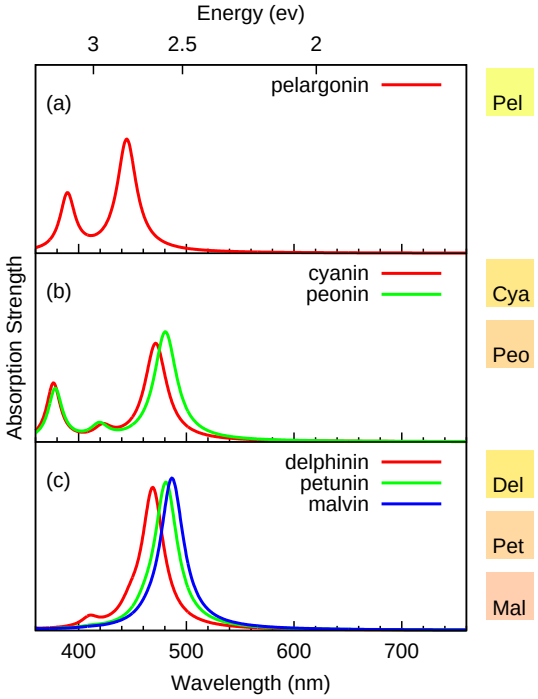

Figure 3.3: Absorption spectra (PBE0) of anthocyanins and their simulated colors.

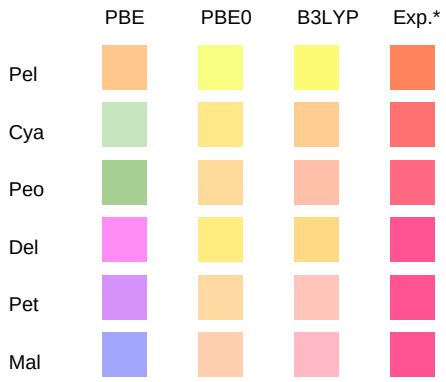

Figure 3.4: Comparing simulated colors in the gas phase with observed colors. *The experimental colors refer to spectra taken in water solution [21, 113, 114].

the gas phase with different XC functionals, and compare them with the observed colors from experimental spectra in water solution. It can be seen that the hybrid functionals give very different colors with respect to PBE functionals, and in some cases, such as in cyanin, peonin, and malvin, they give colors closer to the experimental ones. However, the overall prediction

in the gas phase is not satisfactory. Another interesting feature is that despite the similarity of experimental colors, the PBE gives very distinct colors for different anthocyanins, while this diversity of colors is less pronounced with the hybrid functionals. This is because the peak at short wavelength are shifted to the ultraviolet or near ultraviolet in hybrid functionals, which gives no or little contribution to the color.

3.2 Effects of side groups

In this section, we would like to correlate the differences in the optical spectra among anthocyanins with their chemical structure, in particular with the composition, number, and position of the side groups that decorate the phenyl ring. Possible side groups include $-H$ or $-OR$ ($-OR$ represent both $-OH$ and $-OCH_3$) terminators. From a qualitative point of view, $-H$ has significantly lower electronegativity than the $-OR$ groups, implying a modification of the charge distribution and of the polarization properties by substituting a $-H$ group with a $-OR$ one. Not surprisingly, we found that anthocyanins belonging to each group in Fig. (3.1) have the same number of $-OR$ groups and in the same positions. As we have shown that the choice of the XC functional does not change qualitatively the main features of the molecular spectra, in this section we use PBE results to analyze the effects of side groups.

3.2.1 Ground-state orbitals

For the sake of simplicity, we select one representative molecule from each group, namely pelargonin, peonin, and malvin. In order to illustrate the effects of $-OR$ groups on the ground-state orbitals, we first plot the KS spectra, as discussed in Sec. (2.2.6), of these representative molecules in Fig. (3.5). In the KS spectrum, the transition energy is the energy difference of two KS orbitals, and the oscillator strength of each peak is given by Eq. (2.2.82). Due to the fact that the KS spectra usually have longer absorption wavelength with respect to the TDDFT spectra, in order to consider the TDDFT spectra in the visible range ($380 \sim 780$ nm), we consider the KS spectra in the range of $450 \sim 830$ nm. For all the three molecules, the dominant transition is between an orbital, marked by A, and the LUMO (L). In the case of peonin (panel b), there are two other visible but much weaker transitions, orbital B and orbital C to L. In the case of pelargonin (panel a) and malvin (panel c), the transition $B \to L$ is similar with that in peonin, but the transition $C \to L$ is so weak that it is almost invisible.

In Figs. (3.6) and (3.7) we display the molecular energy levels and orbitals involved in the optical transitions responsible for the spectra reported

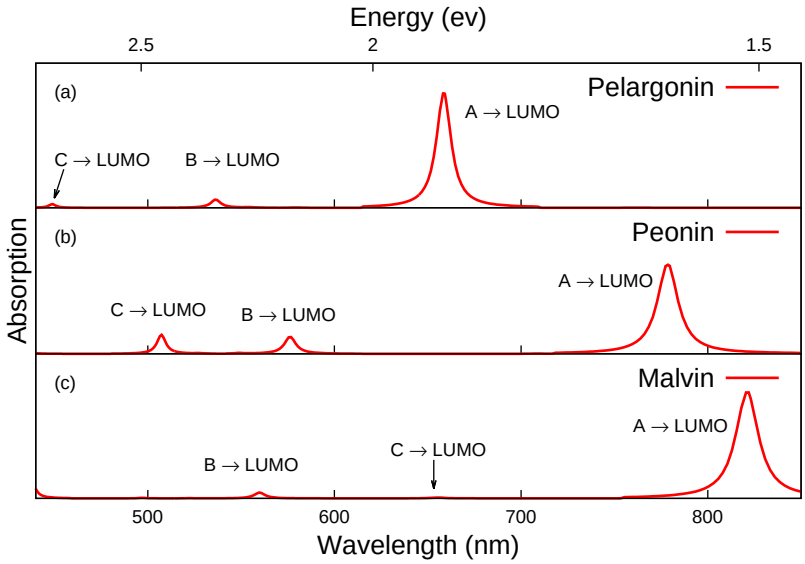

Figure 3.5: KS spectra of selected anthocyanins.

in Fig. (3.5). In Fig. (3.6), all the LUMO's are aligned to 0. The three different colors used for the energy levels indicate the relative localization of the corresponding molecular orbitals on the three different groups constituting the molecule (green for chormenylium, red for phenyl, and sugar in black). It can be found that the transitions from the sugar-localized states, black lines in the figure, to LUMO's are not visible in the KS spectra in Fig. (3.5). This is because all the LUMO's are distributed only on the flavylium backbone (phenyl + chromenylium), with no component from the sugar. Since sugar-localized states have very small overlap with the LUMO, transitions between these states to LUMO are very weak. This is consistent with the conclusions drawn in reference [46].

In Tab. (3.2.1) we present the energy difference between HOMO and LUMO, HOMO and LUMO+1 for all the six molecules. We see that the smallest energy gap between occupied states and LUMO+1's have an energy difference larger than 3 eV. This explains why only these transitions from occupied states to LUMO are relevant for optical spectroscopy.

The iso-surfaces of the four orbitals relevant for optical transitions (A, B, C and LUMO) are illustrated in Fig. (3.7). The shape of LUMO's is hardly affected by the side groups, while occupied states are more sensitive to the presence of $-OR$ groups. The effect of the side groups to the ground-state orbitals is twofold involving both the energy and the symmetry of the single-particle orbitals. Different side groups affect the energy of individ-

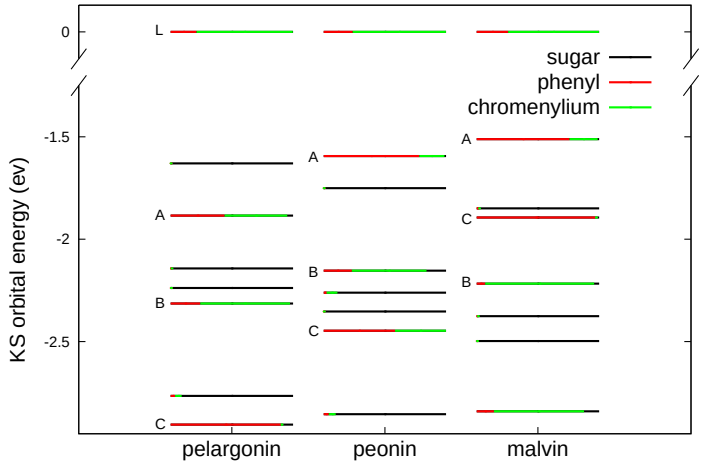

Figure 3.6: Colored KS energy levels of three representative anthocyanins. Different colors indicate the spatial distribution of the orbital (see text).

Anthocyanins	Pel	Cya	Peo	Del	Mal	Pet
$H \rightarrow L$	1.65	1.50	1.59	1.64	1.51	1.55
$H \rightarrow L+1$	3.17	3.05	3.11	3.17	3.01	3.07

Table 3.1: Energy difference of HOMO to LUMO, and HOMO to LUMO+1 of anthocyanins [eV].

ual energy levels both via the influence on the molecular structure and the electrostatic effect (see Fig. (3.6)). The energy of orbital A increases with the number of $-OR$ groups. This is mainly because the $-OR$ group forms an anti-bonding with the A orbital, hence introduces an extra node in the orbital, see Fig. (3.7). For the same reason the energy of orbital C is also increased by the $-OR$ group. The energy of orbital C is more sensitive to the $-OR$ group, because orbital C is localized on the phenyl ring, therefore it is more affected by the change on this ring. In the case of pelargonin and peonin, orbital C has lower energy than both A and B, but in malvin, there are three $-OR$ groups which lifts the energy of C to be higher than the orbital B.

The oscillator strength of individual transitions is affected by the approximate symmetry of the molecular orbitals involved in them. In order to explain the change of orbital symmetry, we define an axis of symmetry for the penyl part of anthocyanin in In Fig. (3.8). In Fig. (3.7) it can be seen that the phenyl ring part of all the LUMO orbitals have approximately the even symmetry with respect to this axis, as well as the orbital A and B of pelargonin and malvin.[2] The orbital C of pelargonin and malvin has

[2] If the molecular orbital rotating along the axis by 180° gives the same wavefunc-

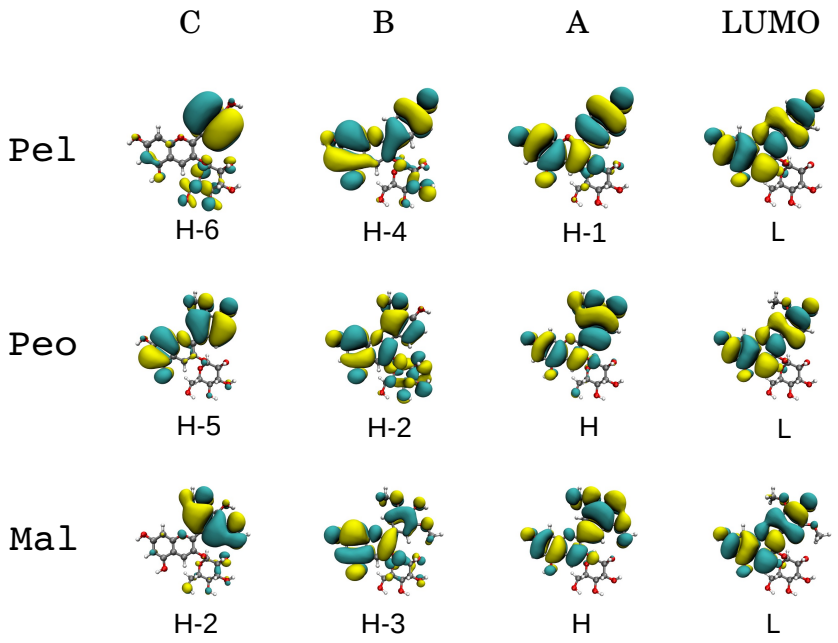

Figure 3.7: Iso-surface of orbitals that are responsible for the spectra in visible range. A, B, C are marked in the same way as they are in Fig. (3.6)

approximately the odd symmetry. Instead in the case of peonin, due to the $-OR$ group on the $R3'$ and the $-H$ on the $R5'$, its ionic structure does not have symmetry on the phenyl ring, as the consequence all the occupied states have also lost the symmetry.

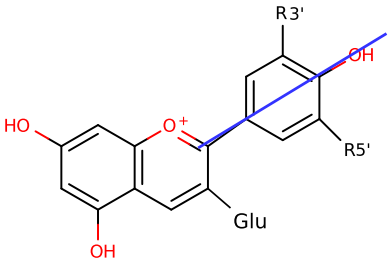

Figure 3.8: Axis of symmetry (blue line) defined for the phenyl group in the molecule.

The influence of $-OR$ groups on the KS spectra can now be understood by the the energy and symmetry of KS orbitals. The transition wavelength of $A \rightarrow L$ and $C \rightarrow L$ increases with the number of $-OR$ groups, because $-OR$ groups relatively increase the energy of orbital A and C as it is shown

tion, we call it even symmetry, while if the rotating gives the negative of the original wavefunction, it is called odd symmetry.

in Fig. (3.6). In the case of pelargonin and malvin, the LUMO has $A1$ symmetry and orbital C has $B1$ symmetry. The oscillator strength of a KS transition is determined by the integration in Eq. (2.2.82). The transition from a $A1$ symmetry orbital to a $B1$ symmetry orbital leads to vanished oscillator strength, therefore the $C \to L$ transition is very weak in panel (a) and panel (c) in Fig. (3.5). However, in the case of peonin, the symmetry of C orbital is broken as we have discussed, so $C \to L$ transition turns to be a bright transition, and introduce an extra peak in the KS spectra.

3.2.2 Optical spectra

In order to better characterize the effects of side groups to the optical spectra, we have analyzed the electron-hole (EH) components of each absorption peak in the TDDFT spectra. The results are summarized both in Tab. (3.2) and Fig. (3.9). In the figure, the transition components are represented by the pie chart in which red indicates the $A \to L$ component, green is $B \to L$ and blue is $C \to L$. White indicates components from other KS transitions. Apart from the second peak of peonin, the white part is always very small, thus confirming that it is very reasonable to analyze optical peaks in terms of a few KS transitions.

Anthocyanins	Peak	Energy(ev)	A → L	B → L	C → L
pelargonin	1	2.03	**64.5**%	**32.9**%	0.0%
	2	2.18	**35.1**%	**59.2**%	0.1%
peonin	1	2.06	**81.0**%	9.7%	8.5%
	2	2.44	3.7%	**67.8**%	5.3%
	3	2.79	12.9%	3.1%	**82.1**%
malvin	1	2.40	5.7%	0.0%	**92.6**%
	2	2.71	**92.9**%	0.0%	5.3%
	3	2.46	0.0%	**84.9**%	0.0%

Table 3.2: EH components of the main peaks of selected anthocyanins in visible range. Bold faces highlight the main contribution to the transition.

In the case of malvin, the only relevant peak is the second one which is mainly due to an $A \to L$ transition. $B \to L$ and $C \to L$ contribute to the first and the third peak respectively. However, since these two KS transitions have very small oscillator strength, their contribution to the TDDFT spectrum is also very weak. This phenomenon can be well described by the single-pole approximation introduced in Sec. (2.2.6).

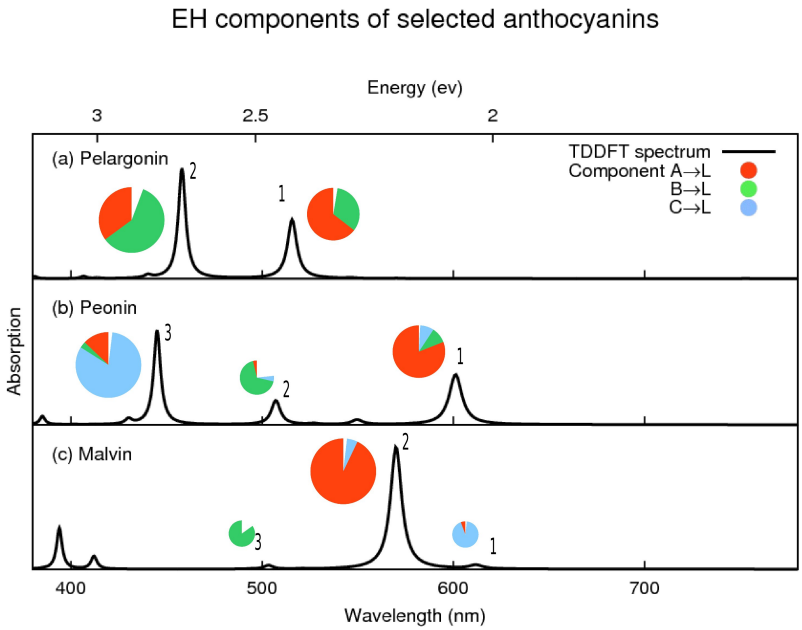

Figure 3.9: The illustration of EH components of the TDDFT peaks. The white part in the chart indicates the components from other KS transitions.

In the case of pelargonin the two strong peaks are both linear combination of $A \rightarrow L$ and $B \rightarrow L$ KS transitions. Although the oscillator strength of $B \rightarrow L$ is very small, due to the effect of the double-pole interaction (see Sec. (2.2.6)), the oscillator strength of $A \rightarrow L$ gives contribution to both TDDFT transitions, resulting in two distinct strong peaks. $C \rightarrow L$ does not contribute to the spectrum for two reasons. First it is energetically too high for the spectrum in the visible range which can be seen in Fig. (3.6). The second reason is related to its symmetry: the oscillator strength of the C $\rightarrow$ LUMO transition is very small hence it cannot be seen in the TDDFT spectrum. The reason why the double-pole effect applies to pelargonin, but not to malvin can be understood by Fig. (3.5), where it is shown that the energy difference between these two KS transitions ($A \rightarrow L$ and $B \rightarrow L$) is much larger in malvin than it is in pelargonin.

As we have discussed for the KS spectrum of peonin, $C \rightarrow L$ becomes a bright transition due to the break of symmetry. From Tab. (3.2) one can see that $A \rightarrow L$, $B \rightarrow L$ and C $\rightarrow L$ are respectively responsible for one peak in the spectrum with slight mixture between each other. The fact that in peonin $C \rightarrow L$ turns to be bright explains why peonin has more absorption peaks in its TDDFT spectrum.

3.2.3 Side groups on the chromenylium ion

Although the change of side groups on the phenyl ring significantly affects the optical properties, we have found that similar changes on the chromenylium ion has little effects on the spectra of anthocaynin. This is illustrated in Figs. (3.10) and (3.11), where we represent the spectra computed for three hypotetical structures derived from delphinin by removing one -OH group on the position 5 (marked as 5H-delphinin), or adding a $-OH$ group on the position 6 (6OH-delphinin). The spectra of these three molecules are presented in Fig. (3.11). It can be seen that neither the spectra nor the simulated colors are remarkably affected by the change of side groups on the chromenylium ring. This is probably because the change on this part of the molecule does not arise any change to the symmetry of anthocyanins.

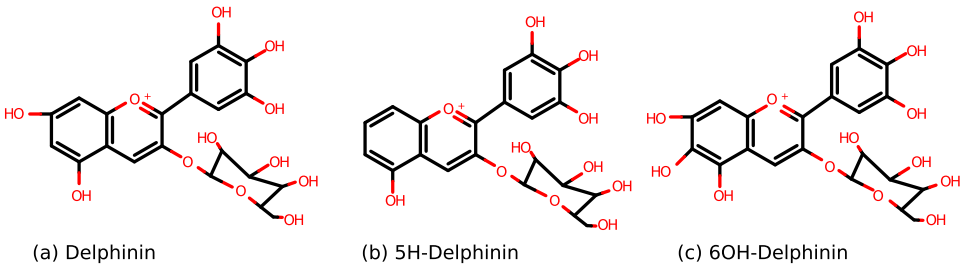

Figure 3.10: The structure of delphinin and two hypothetical anthocyanins derived from it.

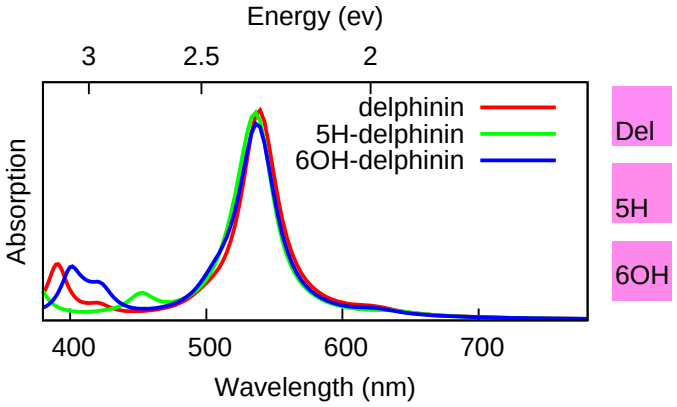

Figure 3.11: The spectra of delphinin and two modified delphinins changing the side groups on the chromenylium ring.

3.3 Explicit solvent model

In Sec. (3.1) we have seen that the simulated colors in the gas phase do not well have good agreement with respect to what is observed in nature. In nature anthocyanins occur in the vacuole of plants' cells, where they are surrounded by an aqueous environment. It is well known that properties of anthocyanins, such as their colors, are strongly affected by the solvent. There are two important effects on the absorption spectra of anthocyanins induced by the solvent. The first is the introduction of a dielectric medium which affects the electronic structure of the molecule. The other effect is due to the thermal fluctuation of the molecular structure in the solvent. Explicit solvent models account for both these effects in a natural way [47].

In this thesis, we have applied a similar procedure as described in Ref. [47]. We have performed AIMD with explicit water molecules for three kinds of anthocyanins: pelargonin, cyanin, and delphinin, using the PBE functional. The molecule was located in the center of a $20 \times 20 \times 12$ Å^3 supercell, and the solvent was simulated with 96 water molecules for delphinin and pelargonin, 95 for cyanin, as illustrated in Fig. (3.12). One Cl atom was also added in the supercell as a counterion in order neutralize the system.

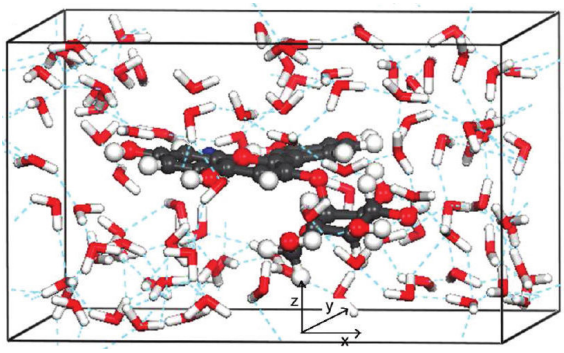

Figure 3.12: The illustration of the supercell of anthocyanin plus water molecules. Reprinted from Ref. [47] with permission.

The water molecules in the system were first thermalized by classical dynamics with anthocyanin kept frozen. Then the whole system was thermalized for 5 ps at room temperature (300K) with Car-Parrinello MD [45], using the `cp.x` executable of the QUANTUM ESPRESSO package with a Nosé-Hoover thermostat to mimic the thermal reservoir of the canonical ensemble [99, 100]. The equilibration phase was then followed by 10 ps of production run under micro canonical (constant-energy) condition. Optical spectra were calculated for 20 snapshots captured along the micro canonical AIMD simulation, and the final spectrum was determined by averaging the

spectra of all the snapshots. The spectra calculation was carried on by the PHLA implemented in this thesis. 3000 iterations for each of three polarizations were taken to converge the spectra in the visible range.

The average spectra calculated with explicit solvent are shown in Fig. (3.13), along with the single-configuration spectra obtained in the gas phase, and the colors obtained from experimental spectra. Solvation results in an overall broadening and red-shift of the absorption peaks.

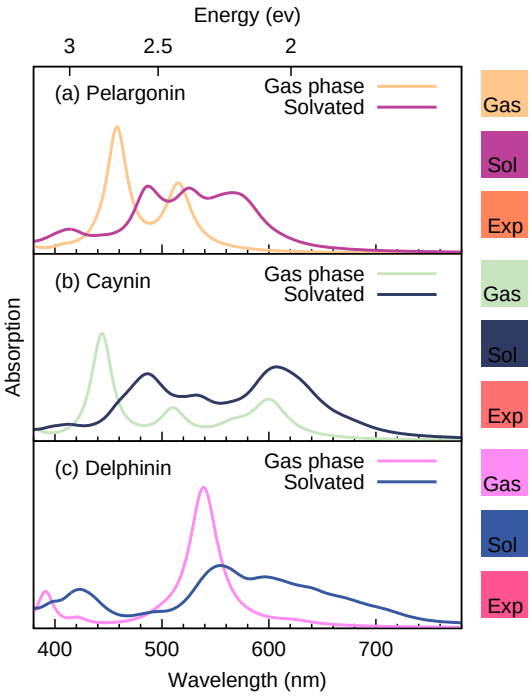

Figure 3.13: Comparing the spectra (PBE) and simulated colors between the single stable configuration in gas phase and the average solvated spectra. The average spectra are calculated with 20 snapshots. All spectra are broadened with $\epsilon = 0.005$ Ry.

In order to illustrate how dramatically the spectra are affected by thermal fluctuations, we took three snapshots from the cyanin's dynamical trajectory and their individual spectra are displayed in Fig. (3.14). One can see that for the same molecule the variation of the spectra of different snapshots is quite large, demonstrating the importance to consider the averaged spectrum instead of single configuration.

In order to highlight the dielectric effects of the solvent, we computed the spectra of the *dehydrated* anthocyanins by taking away the water molecules and the counterion from the dynamical snapshots (See Fig. (3.15)). It can be seen that while the spectra of delphinin and pelargonin are only slightly

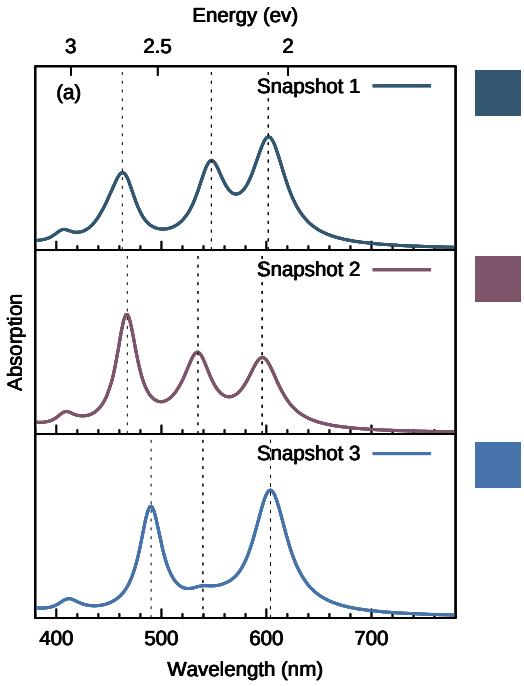

Figure 3.14: Comparing the spectra and simulated colors of 3 different cyanin snapshots.

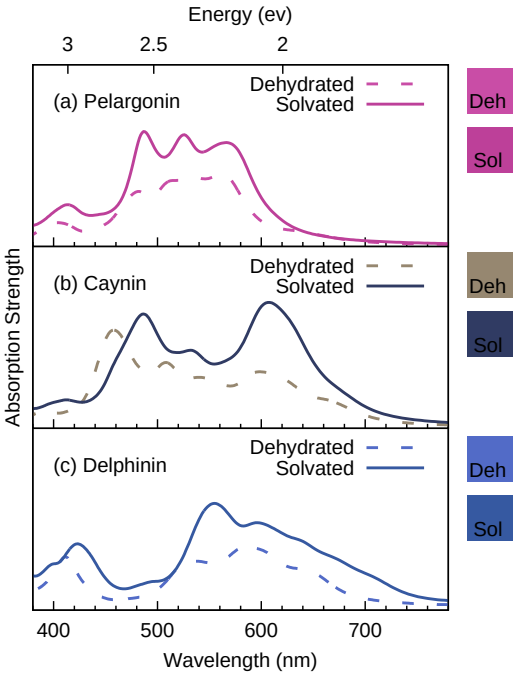

Figure 3.15: Comparing the solavted spectra with dehydrated spectra (PBE). Both kinds of spectra are averaged from 20 snapshots.

affected by the dehydration, the change of cyanin's spectra, especially the position of the third peak, are significant. One possible reason of the difference in cyanin is that hydrogen bonds between anthocyanin and water formed in the simulation of cyanin, but not in the case of delphinin and pelargonin due to the short simulation time. One can also notice that only the peak around 460 nm in cyanin is strongely shifted by the dehydration, which is due to $C \rightarrow L$ KS transition, while this transition is dark for other two molecules (see the analysis in Sec. (3.2)). So another hypothetical explanation is that the transition $C \rightarrow L$ is more affected by the solvent because the orbital C has large polarization. Whatever the reason may be, this is a matter that deserves further investigation.

It can be seen that the solvated spectra calculated with the PBE still do not match the experiment. This is probably due to the failure of the PBE functional. Since we can not afford calculating spectra with hybrid functional for the solvated system at this moment, we have to compromise and consider the hybrid functional spectra for their solvated phase. As we just mentioned, in the case of pelargonin and delphinin, the dehydrated spectra are very similar to the solvated ones. As we have seen in the hybrid functional spectra in the gas phase, the intensity of the peak with short wavelength decreases when using the hyrbrid functional, therefore for cyanin, the difference between the solvated spectra and the dehydrated spectra is supposed to be less dramatic with hybrid functionals. We have calculated the dehydrated spectra with PBE0 and B3LYP. We used the same numerical setting for the gas phase calculation, and the averaged spectra are reported in Fig. (3.16), along with the spectra calculated with PBE. It can be seen that hybrid functionals lead to a blue-shift in the spectra with respect to the PBE, and the intensity of peaks at short wavelength are reduced, being similar to the phenomenon in the gas phase spectra.

In Figs. (3.17) and (3.18) we present comparisons between the dehydrated spectra (PBE0 and B3LYP respectively) and the experimental results. For pelargonin, the calculated absorption peak with both two functionals at about 490 nm is slightly blue-shifted with respect to the experimental result, but the shoulder of the spectrum at the wavelength 405 nm is well reproduced. For cyanin, the main absorption peak calculated with B3LYP excellently matches the experimental spectra, but the peak at 400 nm in the calculation does not appear in the experimental result. In the case of delphinin, the simulated spectrum is about 40 and 15 nm, for the PBE0 and the B3LYP respectively, blue-shifted with respect to the experiment. In spite of some minor deficiencies, such as failing to account the slight red-shift of absorption peaks with respect to the number of $-OR$ groups, our simulation seems to predict rather accurately the observed color properties of anthocyanins.

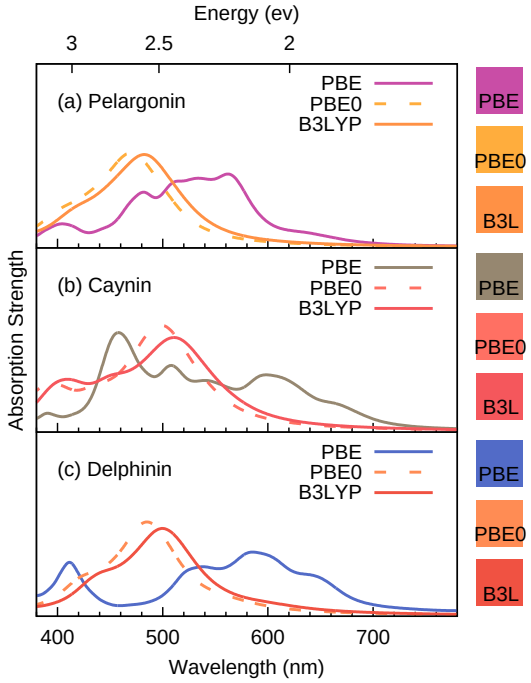

Figure 3.16: Comparing the dehydrated spectra calculated with PBE and B3LYP. All the spectra are averaged from 20 snapshots.

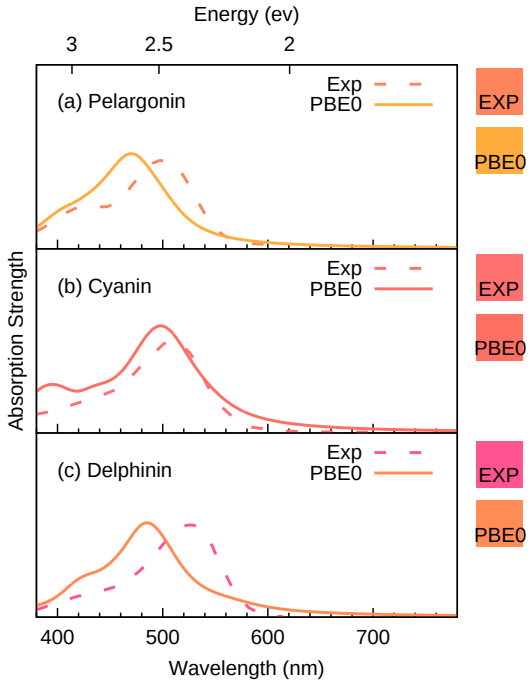

Figure 3.17: Comparing the dehydrated spectra (PBE0) with experimental spectra.

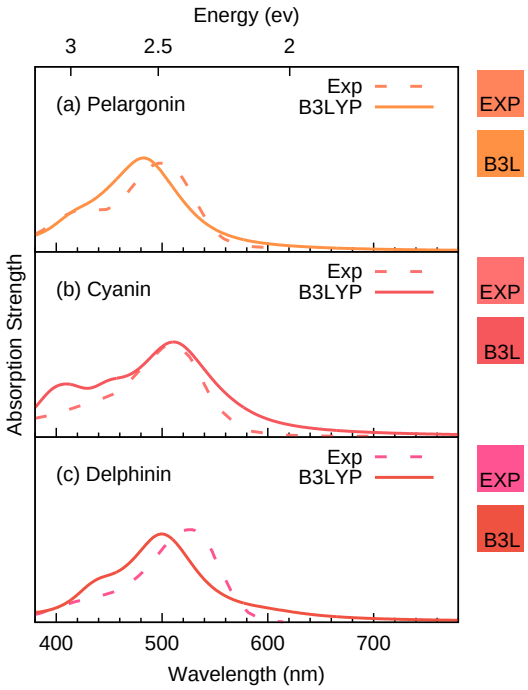

Figure 3.18: Comparing the dehydrated spectra (B3LYP) with experimental spectra.

3.4 Morphing the colors of anthocyanins

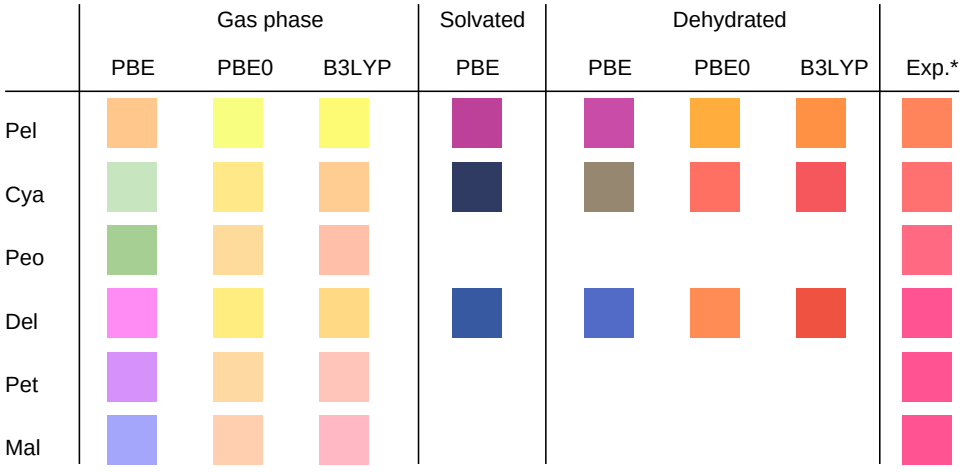

Figure 3.19: Comparing simulated colors obtained from various methods and the experiment. *The experimental colors refer to spectra taken in water solution [21, 113, 114].

In Fig. (3.19) we summarize different colors obtained from the methods we have used so far, along with the experimental colors. Despite the good agreement between the hybrid functional results and the experiment, calculating molecular spectrum with hybrid functional is very expensive. It would be practically very useful if we could estimate the hybrid functional, *e.g.* B3LYP, spectra by morphing the PBE spectra which is computationally much easier. The way we do this is to calculate both the PBE spectra and the B3LYP spectra for the gas phase anthocyanin, and we denote these two spectra as $\kappa_{PBE}(\omega)$ and $\kappa_{B3LYP}(\omega)$, respectively. Then we define a linear function:

$$\Omega = \alpha\omega + \beta. \tag{3.4.1}$$

By choosing parameter α and β we are able to make the two main peaks (or the only one main peak for delphinin) of the PBE gas-phase spectrum computed as a function of Ω coincide with the peaks of the B3LYP as a function of its natural variable, ω. Then we can define a re-scaling function as:

$$s(\omega) = \frac{\kappa_{B3LYP}(\omega)}{\kappa_{PBE}(\Omega(\omega))}. \tag{3.4.2}$$

Then the morphed PBE spectra can be defined as:

$$\tilde{\kappa}_{PBE}(\omega) = s(\omega)\kappa_{PBE}(\alpha\omega + \beta). \tag{3.4.3}$$

By its definition, $\tilde{\kappa}_{PBE}(\omega)$ exactly equals to $\kappa_{B3LYP}(\omega)$. Once we have obtained α, β, and $s(\omega)$, we can estimated the morphed spectra for the dehydrated and solvated phase as:

$$\begin{aligned} \tilde{\kappa}^{Deh}_{PBE}(\omega) &= s(\omega)\kappa^{Deh}_{PBE}(\alpha\omega + \beta), \\ \tilde{\kappa}^{Sol}_{PBE}(\omega) &= s(\omega)\kappa^{Sol}_{PBE}(\alpha\omega + \beta). \end{aligned} \tag{3.4.4}$$

To show the performance of this morphing method, in Fig. (3.20) we display the simulated colors of dehydrated anthocyanins obtained from different methods. Considering the low calculation cost to obtain the morphed spectra, its improvement to the colors calculated by PBE is significant. This indicates a very promising method to estimate the colors calculated with high precision functionals from the results of less expensive calculations.

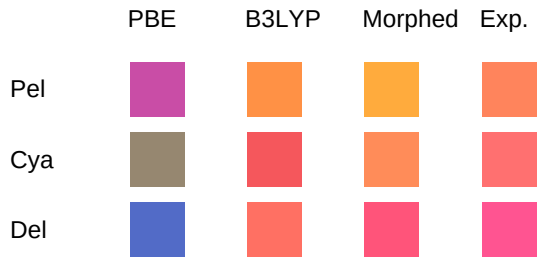

Figure 3.20: Comparing the morphed colors with other calculated and experimental ones.

Conclusions

In this thesis we have developed new numerical methods to calculate the optical spectra of complex molecular systems in complex environments, with time-dependent density-functional theory, and applied them to the color optical properties of anthocyanins in water solution. We have highlighted the importance of a proper account of thermal fluctuation and of a careful choice of exchange-correlation functioanls for describing optical properties, and developed a morphing technique which allows us to approximate the spectra calculated by hybrid functionals based on the much cheaper PBE calculation. The comparison with experimental results has shown rather good accuracy of our approach.

Future work will be devoted to studying the effects of pH and copigmentations, which are important sources of the color diversity of anthocyanins, and to extending our approach to other natural pigments, such as carotenoids and porphyrins. The main chanllenge ahead of us is to incorporate our findings and newly developed methods in an integrated modeling framework that, while increasing efficiency and predictive power of the fully ab-initio techniques utilized in this thesis, will allow to speed up the simulations to the point where hundreds or thousands of molecular systems can be screened for custom-tailored optical properties in a highly automatic way. To this end, we have been working in progress to apply PCM [115] and QM/MM [116] to simulate the solvent model, which allows us to study larger systems with higher efficiency. We are improving the morphing technique as well in order to better approximate the costly calculations from the cheaper ones. In the future, approximate semi-empirical quantum methods are also to be explored in order to best compromise the accuracy and efficiency in predicting colors of natural dyes.

A. Batch representation of general operators

The Batch Representation of an arbitrary operator is defined as:

$$\begin{cases} A_v^x(\mathbf{r}) = \hat{Q}\hat{A}\psi_v^\circ(\mathbf{r}) \\ A_v^y(\mathbf{r}) = \left(\hat{Q}\hat{A}^\dagger\psi_v^\circ(\mathbf{r})\right)^* \end{cases} \tag{0.5}$$

In order to solve Eq. (2.2.31), or the Casida's equation, it is necessary to derive also the BR of all the terms in the definition of $\mathcal{L}$, and the term on the right side of Eq. (2.2.31). For the convenience of our discussion, we name these three terms as:

$$\begin{aligned} \hat{A}1 &= \left[\hat{H}_{KS}^\circ, \hat{\rho}'(\omega)\right] \\ \hat{A}2 &= \left[\hat{v}'_{Hxc}[\hat{\rho}'](\omega), \hat{\rho}^\circ\right] \\ \hat{A}3 &= \left[\hat{r}', \hat{\rho}^\circ\right] \end{aligned} \tag{0.6}$$

In this section, we will derive the BR of all these three operators. We start with the x component of $\hat{A}1$:

$$\begin{aligned} a1_v^x(\mathbf{r}) &= \hat{Q}\left[\hat{H}_{KS}^\circ, \hat{\rho}'(\omega)\right]\psi_v^\circ(\mathbf{r}) \\ &= \hat{Q}\hat{H}_{KS}^\circ\hat{\rho}'(\omega)\psi_v^\circ(\mathbf{r}) - \hat{Q}\hat{\rho}'(t)\hat{H}_{KS}^\circ\psi_v^\circ(\mathbf{r}) \\ &= \hat{H}_{KS}^\circ\hat{Q}\hat{\rho}'(\omega)\psi_v^\circ(\mathbf{r}) - \varepsilon_v\hat{Q}\hat{\rho}'(t)\psi_v^\circ(\mathbf{r}) \\ &= \left(\hat{H}_{KS}^\circ - \varepsilon_v\right)x_v(\mathbf{r}) \\ &\equiv \mathcal{D}x_v(\mathbf{r}) \end{aligned} \tag{0.7}$$

In this expression ε_v is the eigenvalue of the ground-state Hamiltonian, and operator $\hat{H}_{KS}^\circ - \varepsilon_v$ is defined as an operator $\mathcal{D}$. Following similar procedure, we can derive the y component of $\hat{A}1$:

$$a1_v^y(\mathbf{r}) = \left(\hat{Q}\left[\hat{H}_{KS}^\circ, \hat{\rho}'(\omega)\right]^\dagger\psi_v^\circ(\mathbf{r})\right)^* = -\mathcal{D}y_v(\mathbf{r}) \tag{0.8}$$

Before deriving the BR of $\hat{A}2$ we need first to define the response charge density and the Hartree-plus-XC energy caused by the response charge density. The response charge density can be obtained from the diagonal elements of the density matrix:

$$\begin{aligned} n'(\mathbf{r}) &= 2\left\langle \mathbf{r}|\hat{\rho}'(\omega)|\mathbf{r}\right\rangle \\ &= 2\sum_{v\in occ}\psi_v^\circ(\mathbf{r})\left[x_v(\mathbf{r})+y_v(\mathbf{r})\right] \end{aligned} \tag{0.9}$$

Using Density Functional Perturbation Theory (DFPT) [101] the change of Hartree-plus-XC energy caused by the response charge density is calculated as the following way:

$$\begin{aligned} v'_{Hxc}[n'](\mathbf{r}) &= V_{Hxc}[n^\circ+n'] - V_{Hxc}[n^\circ] \\ &= \int \frac{\partial V_{Hxc}[n](\mathbf{r})}{\partial n(\mathbf{r}')}n'(\mathbf{r}')d\mathbf{r}' \\ &\equiv \int \kappa_{Hxc}(\mathbf{r},\mathbf{r}')n'(\mathbf{r}')d\mathbf{r}' \\ &= \sum_{v\in occ}\int 2\kappa_{Hxc}(\mathbf{r},\mathbf{r}')\psi_v^\circ(\mathbf{r}')\left[x_v(\mathbf{r}')+y_v(\mathbf{r}')\right]d\mathbf{r}' \end{aligned} \tag{0.10}$$

Here $\kappa_{Hxc}(\mathbf{r},\mathbf{r}')$ is the kernel of Hartree-plus-XC energy:

$$\kappa_{Hxc}(\mathbf{r},\mathbf{r}') = \frac{1}{|\mathbf{r}-\mathbf{r}'|} + f_{xc}(\mathbf{r},\mathbf{r}') \tag{0.11}$$

Now we can calculate the x component of $\hat{A}2$:

$$\begin{aligned} a2_v^x(\mathbf{r}) &= \hat{Q}\left[\hat{v}'_{Hxc}[\hat{n}'],\hat{\rho}^\circ\right]\psi_v^\circ(\mathbf{r}) \\ &= \hat{Q}\hat{v}'_{Hxc}[n']\hat{\rho}^\circ\psi_v^\circ(\mathbf{r}) - \hat{Q}\hat{\rho}^\circ\hat{v}'_{Hxc}[n']\psi_v^\circ(\mathbf{r}) \\ &= \hat{Q}\hat{v}'_{Hxc}[n']\psi_v^\circ(\mathbf{r}) \\ &= \hat{Q}\sum_{v'\in occ}\int 2\psi_v^\circ(\mathbf{r})\kappa(\mathbf{r},\mathbf{r}')\psi_{v'}^\circ(\mathbf{r}')\left[x_{v'}(\mathbf{r}')+y_{v'}(\mathbf{r}')\right]d\mathbf{r}' \end{aligned} \tag{0.12}$$

The second term in the second step disappears because $\hat{Q}\hat{\rho}^\circ = 0$. We define $K_{vv'}(\mathbf{r},\mathbf{r}') = 2\psi_v^\circ(\mathbf{r})\kappa_{Hxc}(\mathbf{r},\mathbf{r}')\psi_{v'}^\circ(\mathbf{r}')$, then Eq. (0.12) reads:

$$\begin{aligned} a2_v^x(\mathbf{r}) &= -\hat{Q}\sum_{v'\in occ}\int K_{vv'}(\mathbf{r},\mathbf{r}')\left[x_{v'}(\mathbf{r}')+y_{v'}(\mathbf{r}')\right]d\mathbf{r}' \\ &\equiv \mathcal{K}\left[x_{v'}(\mathbf{r}')+y_{v'}(\mathbf{r}')\right] \end{aligned} \tag{0.13}$$

The y component of $\hat{A}2$ can be calculated in the similar way:

$$\begin{aligned} a2_v^y(\mathbf{r}) &= \left(\hat{Q}\left[\hat{v}'_{Hxc}[\hat{n}'],\hat{\rho}^\circ\right]^\dagger\psi_v^\circ(\mathbf{r})\right)^* \\ &= -\mathcal{K}\left[x_{v'}(\mathbf{r}')+y_{v'}(\mathbf{r}')\right] \end{aligned} \tag{0.14}$$

Liouvillian operator is defined as the summation of $A1$ and $A2$, so we are now ready to write $\mathcal{L}$ with BR:

$$\mathcal{L}\begin{pmatrix} X \\ Y \end{pmatrix} = \begin{pmatrix} \mathcal{D}+\mathcal{K} & \mathcal{K} \\ -\mathcal{K} & -\mathcal{D}-\mathcal{K} \end{pmatrix}\begin{pmatrix} X \\ Y \end{pmatrix} \tag{0.15}$$

Now we calculate the BR of $A3$, for the x component there is:

$$\begin{aligned} a3_v^x(\mathbf{r}) &= \hat{Q}\left[\hat{v}'_{ext}, \hat{\rho}^\circ\right]\psi_v^\circ(\mathbf{r}) \\ &= \hat{Q}\hat{v}'_{ext}\psi_v^\circ(\mathbf{r}) \\ &= \hat{Q}\hat{v}'_{ext}\psi_v^\circ(\mathbf{r}) \end{aligned} \tag{0.16}$$

and the y component reads:

$$\begin{aligned} a3_v^y(\mathbf{r}) &= \left(\hat{Q}\left[\hat{v}'_{ext}, \hat{\rho}^\circ\right]^\dagger \psi_v^\circ(\mathbf{r})\right)^* \\ &= -\hat{Q}\hat{v}'_{ext}\psi_v^\circ(\mathbf{r}) \end{aligned} \tag{0.17}$$

Therefore Eq. (2.2.25) can be written with BR as:

$$\begin{pmatrix} \omega-\mathcal{D}-\mathcal{K} & -\mathcal{K} \\ \mathcal{K} & \omega+\mathcal{D}+\mathcal{K} \end{pmatrix}\begin{pmatrix} X \\ Y \end{pmatrix} = \begin{pmatrix} \left\{\hat{Q}\hat{v}'_{ext}\psi_v^\circ(\mathbf{r})\right\} \\ -\left\{\hat{Q}\hat{v}'_{ext}\psi_v^\circ(\mathbf{r})\right\} \end{pmatrix} \tag{0.18}$$

B. Color space

In Sec. (1.2) the RGB color space and its color matching functions (CMF's) are introduced. The exact CMF's that we use in our visualization, as illustrated in Fig. (21), are defined by the CIE standards [102]. For the monochrome at each wavelength, the corresponding values of the RGB CMF's indicate the amount of primary colors in order to reproduce the same color. Not all the monochrome can be matched by mixing three primary colors. When this is the case, one primary color is added to the test monochrome in order to match the mixture of other two primaries. Then the amount of primary color added to the test monochrome is considered to be the negative value in Fig. (21).

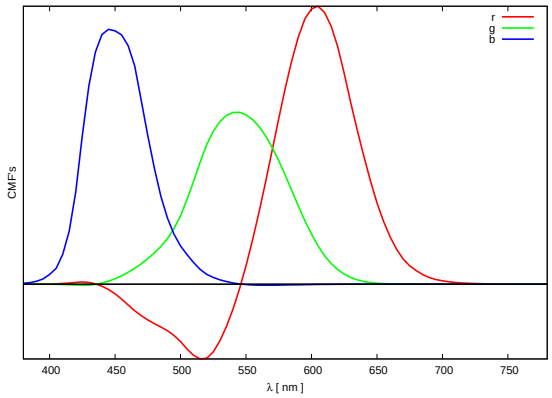

Figure 21: The CIE 1931 RGB CMF's functions. The negative part of function R is explained in the text.

Having negative values in the CMF's is not very convenient, because one can not produce negative amount of light on the screen, neither to add negative amount of pigment in the dyestuff. For this reason a linear transform of RGB CMF's is defined in order to ensure that functions are always positive [102] (The XYZ CMF's are illustrated in Fig. (22)):

$$\begin{pmatrix} X \\ Y \\ Z \end{pmatrix} = \frac{1}{0.17697} \begin{pmatrix} 0.49 & 0.31 & 0.20 \\ 0.17697 & 0.81240 & 0.01063 \\ 0.00 & 0.01 & 0.99 \end{pmatrix} \begin{pmatrix} R \\ G \\ B \end{pmatrix} \qquad (0.19)$$

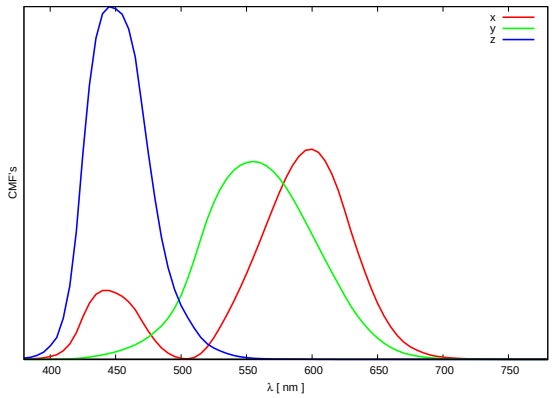

Figure 22: The CIE standard XYZ CMF's functions.

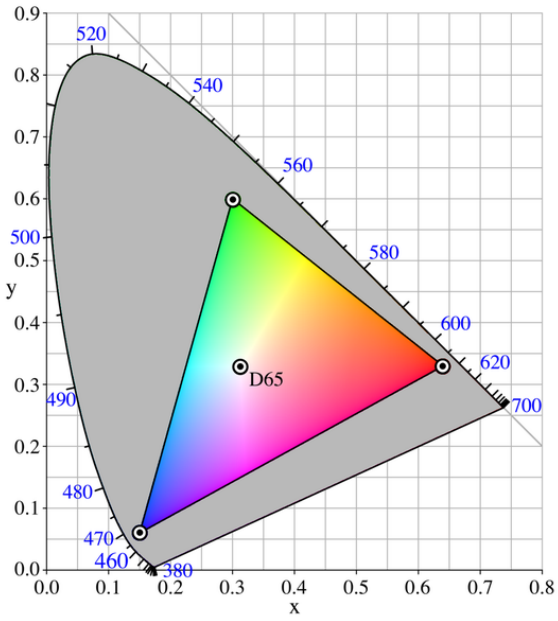

Figure 23: The relation between the XYZ and the RGB color space. D65 is the color of standard solar ray.

The relation between the XYZ space and the RGB space is shown in Fig. (23)). In principle XYZ is a larger color space than RGB, but all the colors that can be displayed on the screen has to be constrained by the fact that no RGB component can be negative, so only the colors within the RGB space can be displayed here. In this figure the area on the outside of the RGB triangle is represented by grey color.

C. User's guide for turbo_davidson.x

The turbo-Davidson algorithm introduced in Sec. (2.3.1) has been implemented in QUANTUM ESPRESSO [103, 104] as `turbo_davidson.x`. The code can be downloaded from website:

`http://qe-forge.org/gf/project/q-e/scmsvn/?action=AccessInfo`

Information about the installation of the code can be found in reference [104]. This guide is written for the SVN version 10468 and later.

1 Quick start: the minimum input and output

The `turbo_davidson.x` should be run after the standard ground-state calculation `pw.x` [104].[3] The minimum input of `turbo_davidson.x` consists of two namelists. The necessary parameters and their meanings are presented in Tab. (3) When the calculation is finished, one obtains three output file: *prefix.plot*, *prefix.eigen*, and the standard output. The file *prefix.eigen* contains the excitation energy of *num_eign* eigenstates, and their respective oscillator strength. The file *prefix.plot* is the spectrum interpreted from the eigenstates.

If one is interested in more detailed information of the transition rather than just the absorption spectrum, the standard output file can be very useful. A typical standard output presents various information for every eigenstate, among which the most interesting one is the electron-hole components of each transition. Depending on how many empty states have been computed in the ground-state calculation, there are usually $N_v \times N_c$ electron-hole pairs, all of their components can be found in the component list. For underlining the dominant contribution fo each transition, electron-

[3] Although not necessary, it is highly suggested to compute a few empty states in the ground-state calculation. It helps to guess the trial vectors, which significantly improves the convergence.

Namelist	Variable	Value	Description
lr_input	`prefix`	C2H4	Should have the same prefix with the ground-state `pw.x` run .
	`outdir`	'out'	The directory that contains the run critical files, which include the files generated by ground-state `pw.x` run..
lr_dav	`num_eign`	10	Number of eigenstates to be calculated.
	`num_init`	20	Number of trial vectors.
	`num_basis_max`	200	Maximum number of basis vectors allowed in the subspace. When this number is reached, a discharging routine is called, sorting out 2×num_eign best vectors in the subspace and dumping the others.
	`residue_conv_thr`	10E-4	Threshold for the convergence. When the square of the residue is smaller than this value, the convergence is achieved.
	`reference`	0.0	ω_{ref} (Ry) is used to favor these eigenstates which have ω's the closest to this value.
	`start`	0.0	The lower limit of the energy (Ry) scale for the spectrum calculation.
	`finish`	1.0	The upper limit of the energy (Ry) scale for the spectrum calculation.
	`broadening`	0.01	Value (Ry) to broaden the spectrum.
	`step`	0.001	Energy step (Ry) for the spectrum calculation.

Table 3: Input parameters for `turbo_davidson.x`

hole pairs with contribution larger than 10% are also printed as the *principle components*. In principle, if all the empty states were calculated, the square summation of these components should equal to 1. However, this is smaller than 1 if only a few number of empty states are calculated.

2 Memory bottleneck

The biggest bottleneck for the `turbo_davidson.x` is the consumption of the memory. For better utilizing this code, it is helpful to have a little bit knowledge about its memory use. The dominant memory use for this algorithm comes from the storage of basis vectors and eigenvectors. The size of a single vector is $N_{PW}N_v \times 16$ *bytes*, where 16 accounts for the number of *bytes* in order to store a double precision complex number in a *64-bit* system.[4] For each eigenstate, two vectors are required, respectively for the left and right eigenvectors. The situation is a little bit more complicate for the storage of basis vectors. In principle, only one vector is necessary for storing each basis vector in the basis set, $[w_1, w_2, ..., w_m]$. However, when one is using USPP, it is often suggested to store also the basis set acted by the $\hat{s}$ matrix, $\{\hat{s}w_i\}$.[5] Besides, in order to construct the *oblique projection* of the matrix A and B in the subspace,[6] one can also store the vectors $\{Aw_i\}$ and $\{Bw_i\}$, which are used for many times in the algorithm. In total, this leads to $4 \times num\_basis\_max$ vectors to be stored. In order to help users to understand how much memory is required for the calculation, the memory per core for storing the basis vectors and eigenvectors is reported at the beginning of the standard output. Users should make sure that the system has enough memory to perform the calculation.

A straightforward method to decrease the memory use is to calculate less eigenstates, and set smaller num_basis_max. If more eigenstates are needed, one could perform multiple calculation with different reference energy. Besides, with the planewave parallelization [104], the wave-functions are distributed among different processes, using more CPU's can almost linearly decrease the memory cost for each CPU.

There are two other parameters that the user can utilize to significantly decrease the memory cost by scarifying the calculation efficiency. By setting $poor\_of\_ram = .true.$ in the lr_dav namelist, one calculates $\hat{s}w_i$ whenever it is used, instead of storing it. This would affect only the calculation with USPP. One could also set $poor\_of\_ram2 = .true.$, then $\{Aw_i\}$ and $\{Bw_i\}$

[4] It can be different depending on the machine system, but it is usually 16 bytes.
[5] One can look into reference [94] for the explanation of the $\hat{s}$ matrix.
[6] See Eq. (2.3.8).

will not be stored. By using both these two parameters, the memory cost can be reduced almost by a factor of 4. As the price, the calculation speed is usually decreased by a factor of 2.

3 Recalculating the spectrum

All the information required to calculate the spectrum is in the file *prefix.eigen*. In the case that user would like to recalculate the spectrum with different setting, such as broadening and energy scale, he can use the `turbo_spectrum.x` which has been adapted to work with `turbo_davidson.x`. The input parameters and their explanation are presented in Tab. (4).

Namelist	Variable	Value	Description
lr_input	`prefix`	C2H4	Should have the same prefix with the ground-state `pw.x` run .
	`td`	"davidson"	To tell the code that it is working with turbo-Davidson.
	`start`	0.0	The lower limit of the energy (Ry) scale for the spectrum calculation.
	`end`	1.0	The upper limit of the energy (Ry) scale for the spectrum calculation.
	`epsilon`	0.01	Value (Ry) to broaden the spectrum.
	`increment`	0.001	Energy step (Ry) for the spectrum calculation.

Table 4: Input parameters for `turbo_spectrum.x`

D. Convergence indicator for the turbo-Davidson

When we are talking about the convergence of the spectrum we are caring about the convergence of the transition energy and the oscillator strength. However most of the time knowing the level of their convergence and knowing when to stop the iteration is a hindsight because we have to consider much more iterations before concluding that the calculation has already converged with less iterations. Instead in the turbo-Davidson algorithm we can monitor the modulus of the residual and use it as the convergence variable. Now we show that it is possible to estimate the error of the transition energy and the oscillator strength based on the residual vectors.

Although it is not necessary, we use the TDA, Eq. (2.2.77), to estimate the error for the sake of clarity. Suppose $\{\omega, X\}$ is an exact eigenpair of Eq. (2.2.77), while $\{\tilde{\omega}, \tilde{X}\}$ is its approximation in the subspace, their difference are small values:

$$\begin{aligned} X &= \tilde{X} + \Delta X, \\ \omega &= \tilde{\omega} + \Delta\omega. \end{aligned} \tag{3.1}$$

The residual vector reads:

$$\begin{aligned} r &= \mathcal{L}^{TDA}\tilde{X} - \tilde{\omega}\tilde{X} \\ &= \mathcal{L}^{TDA}(X - \Delta X) - (\omega - \Delta\omega)\tilde{X} \\ &= \omega\Delta X - \mathcal{L}^{TDA}\Delta X + \Delta\omega\tilde{X} \\ &\approx O(\Delta X). \end{aligned} \tag{3.2}$$

The exact eigenvalue reads:

$$\begin{aligned} \omega &= \langle X|\mathcal{L}^{TDA}|X\rangle \\ &= \left\langle \tilde{X} + \Delta X|\mathcal{L}^{TDA}|\tilde{X} + \Delta X\right\rangle \\ &= \tilde{\omega} + 2\left\langle \Delta X|\mathcal{L}^{TDA}|\tilde{X}\right\rangle + \langle \Delta X|\mathcal{L}^{TDA}|\Delta X\rangle \\ &= \tilde{\omega} + 2\tilde{\omega}\left\langle \Delta X|\tilde{X}\right\rangle + 2\langle \Delta X|r\rangle + \langle \Delta X|\mathcal{L}^{TDA}|\Delta X\rangle . \end{aligned} \tag{3.3}$$

The second term in Eq. (3.3) can be estimated by the normalization condition:

$$\langle X|X\rangle = \left\langle \tilde{X}|\tilde{X}\right\rangle = 1, \tag{3.4}$$

which leads to :

$$2\left\langle \Delta X|\tilde{X}\right\rangle = -|\Delta X|^2 \approx O(|r|^2) \tag{3.5}$$

With the same approxmation the third and the last term in Eq. (3.3) can be estimated as:

$$\begin{aligned} 2\langle \Delta X|r\rangle &\approx O(|r|^2) \\ \left\langle \Delta X|\mathcal{L}^{TDA}|\Delta X\right\rangle &\approx O(|r|^2) \end{aligned} \tag{3.6}$$

Now it is sufficient to conclude that:

$$\omega - \tilde{\omega} \approx O(|r|^2) \tag{3.7}$$

The convergence of the oscillator strength can be derived in a similar way :

$$\begin{aligned} F &= \pi\,(u, X)\,(X, v) \\ &= \tilde{F} + \pi\left[\left(u, \tilde{X}\right)(\Delta X, v) + (u, \Delta X)\left(\tilde{X}, v\right)\right] + O(|r|^2) \end{aligned} \tag{3.8}$$

so Eq. (3.8) leads to :

$$F - \tilde{F} \approx O(|r|) \tag{3.9}$$

In summary, the error of the transition energy is proportional to the squared modulus of the residual and the error of the oscillator strength is proportional to the modulus of residual.

Bibliography

[1] Barbara Berrie and Louisa Matthews, *Material Innovation and Artistic Invention; New Materials and New Colors in Renaissance Venetian Paintings. NAS Colloquium on the Scientific Examination of Art: Modern Techniques* , Conservation and Analysis. National Academies Press, (2005)

[2] Filip Vermeylen, The Colour of Money: Dealing in Pigments in Sixteenth-Century Antwerp, pg. 359. *Venice dominated the trade in pigments in the Mediterranean basin during the sixteenth century.* Pg. 359

[3] Make-Up Industry: *Market Research Reports*, Statistics and Analysis, marketline, Nov.

[4] Ø.M. Andersen, *Anthocyanins*, in: eLS, John Wiley & Sons, Ltd, 2001.

[5] R.L. Jackman, R.Y. Yada, M.A. Tung, R.A. Speers, *Anthocyanins as Food Colorants*: a Review, Journal of Food Biochemistry. 11 (1987) 201-247.

[6] J. Kang, Z. Li, T. Wu, G.S. Jensen, A.G. Schauss, X. Wu, *Anti-oxidant capacities of flavonoid compounds isolated from acai pulp* (Euterpe oleracea Mart.), Food Chemistry. 122 (2010) 610.

[7] F.J. Francis, P.C. Markakis, *Food colorants: Anthocyanins*, Critical Reviews in Food Science and Nutrition. 28 (1989) 273.

[8] C. Kaur, H.C. Kapoor, *Anti-oxidant activity and total phenolic content of some Asian vegetables*, International Journal of Food Science & Technology. 37 (2002) 153.

[9] S. Zafra-Stone, T. Yasmin, M. Bagchi, A. Chatterjee, J.A. Vinson, D. Bagchi, *Berry anthocyanins as novel antioxidants in human health and disease prevention*, Molecular Nutrition & Food Research. 51 (2007) 675.

[10] L.-S. Wang, G.D. Stoner, *Anthocyanins and their role in cancer prevention*, Cancer Letters. 269 (2008) 281.

[11] Hou D-X., *Potential Mechanisms of Cancer Chemoprevention by Anthocyanins*, Current Molecular Medicine. 3 (2003) 149.

[12] J.-M. Kong, L.-S. Chia, N.-K. Goh, T.-F. Chia, R. Brouillard, *Analysis and biological activities of anthocyanins*, Phytochemistry. 64 (2003) 923-933.

[13] K. Wongcharee, V. Meeyoo, S. Chavadej, *Dye-sensitized solar cell using natural dyes extracted from rosella and blue pea flowers*, Solar Energy Materials and Solar Cells. 91 (2007) 566.

[14] H. Zhu, H. Zeng, V. Subramanian, C. Masarapu, K.-H. Hung, B. Wei, *Anthocyanin-sensitized solar cells using carbon nanotube films as counter electrodes*, Nanotechnology. 19 (2008) 465204.

[15] A. Yella, H.-W. Lee, H.N. Tsao, C. Yi, A.K. Chandiran, M.K. Nazeeruddin, et al., *Porphyrin-Sensitized Solar Cells with Cobalt (II/III) Based Redox Electrolyte Exceed 12 Percent Efficiency*, Science. 334 (2011) 629.

[16] V.V. de Rosso, A.Z. Mercadante, *Evaluation of colour and stability of anthocyanins from tropical fruits in an isotonic soft drink system*, Innovative Food Science & Emerging Technologies. 8 (2007) 347

[17] Brouillard, R. Flavonoids and flower color. *In "The Flavonoids"*; Harborne, J. B., Ed.; Chapman and Hall Ltd: London, 1988; pp 525- 538

[18] Erich Grotewold, *The science of 5 flavonoids*, Springer Ed. (2007)

[19] R. Brouillard, Chapter 1, in: *Anthocyanins as Food Colors*, Elsevier, 1982.

[20] R.N. Cavalcanti, D.T. Santos, M.A.A. Meireles, *Non-thermal stabilization mechanisms of anthocyanins in model and food systemsâAn overview*, Food Research International. 44 (2011) 499-509.

[21] L. Rustioni, F. Di Meo, M. Guillaume, O. Failla, P. Trouillas, *Tuning color variation in grape anthocyanins at the molecular scale*, Food Chemistry. 141 (2013) 4349-4357.

[22] J. He, L.E. Rodriguez-Saona, M.M. Giusti, *Midinfrared Spectroscopy for Juice AuthenticationRapid Differentiation of Commercial Juices*, J. Agric. Food Chem. 55 (2007) 4443-4452.

[23] J. Barrios, C.P. Cordero, F. Aristizabal, F.J. Heredia, A.L. Morales, C. Osorio, *Chemical analysis and screening as anticancer agent of anthocyanin-rich extract from Uva Caimarona (Pourouma cecropiifolia Mart.) fruit*, J. Agric. Food Chem. 58 (2010) 2100-2110.

[24] W. Zheng, S.Y. Wang, *Oxygen radical absorbing capacity of phenolics in blueberries, cranberries, chokeberries, and lingonberries*, J. Agric. Food Chem. 51 (2003) 502-509.

[25] F. Tatsuzawa, K. Shinoda, *Comparison between identification of anthocyanin by HPLC analysis with a photodiode array detector and that using TLC combined with UV-VIS spectral analysis*, Hort. Res.(Japan) 4(2):225, 2005

[26] A. Unciti-Broceta, M. Rahimi Yusop, P.R. Richardson, J.G.A. Walton, M. Bradley, *A fluorescein-derived anthocyanidin-inspired pH sensor*, Tetrahedron Letters. 50 (2009) 3713.

[27] Th. Mulder-Krieger, R. Verpoorte, *Anthocyanins as Flower Pigments, Feasibilities for flower colour modification* Springer Netherlands, 1994

[28] L. Michaelis, M.P. Schubert, C.V. Smythe, *Potentiometric Study of the Flavins*, J. Biol. Chem. 116 (1936) 587-607.

[29] M. Forster, *Plant pigments as acid-base indicators - An exercise for the junior high school*, J. Chem. Educ. 55 (1978) 107.

[30] M. Rein, *Copigmentation reactions and color stability of berry anthocaynins*, 2005, PHD thesis

[31] R. Brouillard, *The in vivo expression of anthocyanin colour in plants, Phytochemistry.* 22 (1983) 1311

[32] L.F. Reyes, L. Cisneros-Zevallos, *Degradation kinetics and colour of anthocyanins in aqueous extracts of purple- and red-flesh potatoes (Solanum tuberosum L.)*, Food Chemistry. 100 (2007) 885-894.

[33] C. Malien-Aubert, O. Dangles, M.J. Amiot, *Color stability of commercial anthocyanin-based extracts in relation to the phenolic composition. Protective effects by intra- and intermolecular copigmentation*, J. Agric. Food Chem. 49 (2001) 170

[34] T. Yabuya, M. Nakamura, T. Iwashina, M. Yamaguchi, T. Takehara, *Anthocyanin-flavone copigmentation in bluish purple flowers of Japanese garden iris (Iris ensata Thunb.)*, Euphytica. 98 (1997) 163

[35] M. E. Nadal, E. A. Early, E. A. Thompson, *Specular Gloss* ,NIST Special Publication SP250-70, 2006

[36] D.H.B. Bei Xiao, *Surface gloss and color perception of 3D objects.*, Visual Neuroscience. 25 (2008) 371

[37] N. Ohta, A.R. Robertson, *CIE Standard Colorimetric System*, in: Colorimetry, John Wiley & Sons, Ltd, 2006: pp. 63.

[38] J. Marshall, T.W. Cronin, S. Kleinlogel, *Stomatopod eye structure and function: A review*, Arthropod Structure & Development. 36 (2007) 420

[39] G. Ruskell, *The Human Eye, Structure and Function*, Clyde W. Oyster; Sinauer Associates, Sunderland, MA, 1999, 766 pages, hardback, ISBN 0-87893-645-9

[40] A. Stockman, D.I.A. MacLeod, N.E. Johnson, *Spectral sensitivities of the human cones*, J. Opt. Soc. Am. A. 10 (1993) 2491.

[41] J. Schanda, *CIE Colorimetry*, in: J.S.S. of the C.V.P. chairs President (Ed.), Colorimetry, John Wiley & Sons, Inc., 2007: pp. 25.

[42] H.J.A. Dartnall, J.K. Bowmaker, J.D. Mollon, *Human Visual Pigments: Microspectrophotometric Results from the Eyes of Seven Persons*, Proc. R. Soc. Lond. B. 220 (1983) 115.

[43] A.D. Broadbent, *A critical review of the development of the CIE1931 RGB color-matching functions*, Color Research & Application. 29 (2004) 267.

[44] *Numerical Simulation in Molecular Dynamics - Numerics, Algorithms, Parallelization, Applications*, n.d.

[45] M.C. Payne, M.P. Teter, D.C. Allan, T.A. Arias, J.D. Joannopoulos, *Iterative minimization techniques for ab initio total-energy calculations: molecular dynamics and conjugate gradients*, Rev. Mod. Phys. 64 (1992) 1045

[46] A. Calzolari, D. Varsano, A. Ruini, A. Catellani, R. Tel-Vered, H.B. Yildiz, et al., *Optoelectronic Properties of Natural cyanin Dyes*, J. Phys. Chem. A. 113 (2009) 8801.

[47] O.B. Malcıoğlu, A. Calzolari, R. Gebauer, D. Varsano, S. Baroni, *Dielectric and Thermal Effects on the Optical Properties of Natural Dyes: A Case Study on Solvated cyanin*, J. Am. Chem. Soc. 133 (2011) 15425

[48] A. Calzolari, S. Monti, A. Ruini, A. Catellani, *Hydration of cyanin dyes*, The Journal of Chemical Physics. 132 (2010) 114304

[49] E. Runge, E.K.U. Gross, *Density-Functional Theory for Time-Dependent Systems*, Phys. Rev. Lett. 52 (1984) 997.

[50] G. Onida, L. Reining, A. Rubio, *Electronic excitations: density-functional versus many-body Greenâs-function approaches*, Rev. Mod. Phys. 74 (2002) 601

[51] M. Grüning, A. Marini, X. Gonze, *Implementation and testing of Lanczos-based algorithms for Random-Phase Approximation eigenproblems*, Computational Materials Science. 50 (2011) 2148.

[52] P. Hohenberg, W. Kohn, *Inhomogeneous Electron Gas*, Phys. Rev. 136 (1964) B864.

[53] R.P. Feynman, *Statistical Mechanics* (Benjamin, Reading, 1972, p. 249

[54] A.D. Becke, *Density-functional exchange-energy approximation with correct asymptotic behavior*, Phys. Rev. A. 38 (1988) 3098

[55] J.P. Perdew, Y. Wang, *Accurate and simple analytic representation of the electron-gas correlation energy*, Phys. Rev. B. 45 (1992) 13244

[56] J.P. Perdew, K. Burke, M. Ernzerhof, *Generalized Gradient Approximation Made Simple*, Phys. Rev. Lett. 77 (1996) 3865

[57] R. M. Martin, *Electronic structure: Basic Theory and practical methods*, 2003

[58] A.D. Becke, *A new mixing of Hartree-Fock and local density-functional theories*, The Journal of Chemical Physics. 98 (1993) 1372.

[59] C. Adamo, V. Barone, *aoward reliable density functional methods without adjustable parameters: The PBE0 model*, The Journal of Chemical Physics. 110 (1999) 6158.

[60] R.P. Feynman, *Forces in Molecules*, Phys. Rev. 56 (1939) 340-343.

[61] Fetter, A. L. and Walecka, J. D. *Quantum Theory of Many-Particle Systems*. McGraw-Hill, New York, first edition, 1971

[62] R. Bauernschmitt, R. Ahlrichs, *Treatment of electronic excitations within the adiabatic approximation of time dependent density functional theory*, Chemical Physics Letters. 256 (1996) 454.

[63] organ A. Dreuw, M. Head-Gordon, *Failure of time-dependent density functional theory for long-range charge-transfer excited states: the zincbacteriochlorin-bacteriochlorin and bacteriochlorophyll-spheroidene complexes*, J. Am. Chem. Soc. 126 (2004) 4007

[64] E.K.U. Gross, W. Kohn, *Local density-functional theory of frequency-dependent linear response*, Phys. Rev. Lett. 55 (1985) 2850

[65] M. E. Casida. *Recent Advances in Density Functional Methods* Part I. World Scientific, Singapore, 1995.

[66] M. E. Casida. *Propagator corrections to adiabatic time-dependent density-functional theory linear response theory.* J. Chem. Phys., 122:054111, 2005.

[67] U. H. Gerlach, *LINEAR MATHEMATICS IN INFINITE DIMENSIONS Signals Boundary Value Problems and Special Functions*, 2010

[68] S. Baroni, P. Giannozzi, A. Testa, *Green's-function approach to linear response in solids*, Phys. Rev. Lett. 58 (1987) 1861

[69] S. Baroni, S. de Gironcoli, A. Dal Corso, P. Giannozzi, *Phonons and related crystal properties from density-functional perturbation theory*, Rev. Mod. Phys. 73 (2001) 515

[70] D. Rocca, R. Gebauer, Y. Saad, S. Baroni, *Turbo charging time-dependent density-functional theory with Lanczos chains*, The Journal of Chemical Physics. 128 (2008) 154105.

[71] J. Hutter, *Excited state nuclear forces from the Tamm-Dancoff approximation to time-dependent density functional theory within the plane wave basis set framework*, The Journal of Chemical Physics. 118 (2003) 3928

[72] S. Baroni, R. Gebauer, in: M.A.L. Marques, N. Maitra, F. Nogueira, E.K.U. Gross, A. Rubio (Eds.), *Fundamentals of Time-Dependent Density Functional Theory*, Springer, Berlin, in preparation.

[73] X. Ge, S. Binnie, and S. Baroni, unpublished.

[74] D.J. Thouless, *Stability conditions and nuclear rotations in the Hartree-Fock theory*, Nuclear Physics. 21 (1960) 225

[75] S. Hirata, M. Head-Gordon, *Time-dependent density functional theory within the Tamm-Dancoff approximation*, Chemical Physics Letters. 314 (1999) 29

[76] C.A. Ullrich, *Time-dependent density-functional theory: concepts and applications*, Oxford University Press, Oxford; New York, 2012.

[77] I. Vasiliev, S. Ögüt, J.R. Chelikowsky, *Ab Initio Excitation Spectra and Collective Electronic Response in Atoms and Clusters*, Phys. Rev. Lett. 82 (1999) 1919

[78] H. Appel, E.K.U. Gross, K. Burke, *Double-pole approximation in time-dependent density functional theory*, International Journal of Quantum Chemistry. 106 (2006) 2840

[79] J. Hutter, *Excited state nuclear forces from the Tamm-Dancoff approximation to time-dependent density functional theory within the plane wave basis set framework*, The Journal of Chemical Physics. 118 (2003) 3928.

[80] E. Anderson, Z. Bai, C. Bischof, S. Blackford, J. Demmel, J. Dongarra, et al., *LAPACK Users' Guide*, Third, Society for Industrial and Applied Mathematics, Philadelphia, PA, 1999.

[81] C.D. Meyer, *Matrix analysis and applied linear algebra, Society for Industrial and Applied Mathematics*, Philadelphia, 2000.

[82] E.R. Davidson, *Super-matrix methods*, Computer Physics Communications. 53 (1989) 49

[83] E.R. Davidson, *The iterative calculation of a few of the lowest eigenvalues and corresponding eigenvectors of large real-symmetric matrices*, Journal of Computational Physics. 17 (1975) 87

[84] S. Rettrup, *An iterative method for calculating several of the extreme eigensolutions of large real non-symmetric matrices*, Journal of Computational Physics. 45 (1982) 100

[85] J. Olsen, B.O. Roos, P. Jørgensen, H.J.A. Jensen, *Determinant based configuration interaction algorithms for complete and restricted configuration interaction spaces*, The Journal of Chemical Physics. 89 (1988) 2185.

[86] S. Tretiak, C.M. Isborn, A.M.N. Niklasson, M. Challacombe, *Representation independent algorithms for molecular response calculations in time-dependent self-consistent field theories*, The Journal of Chemical Physics. 130 (2009) 054111.

[87] R. Zimmermann, *Influence of the Non-Hermitian Splitting Terms on Excitonic Spectra*, Physica Status Solidi (b). 41 (1970) 23.

[88] R.E. Stratmann, G.E. Scuseria, M.J. Frisch, *An efficient implementation of time-dependent density-functional theory for the calculation of excitation energies of large molecules*, The Journal of Chemical Physics. 109 (1998) 8218

[89] D. Rocca, S. Baroni, R. Gebauer, *Time-Dependent Density Functional Perturbation Theory: New algorithms with applications to molecular spectra*, PHD thesis, 2007

[90] O.B. Malcıoğ, R. Gebauer, D. Rocca, S. Baroni, *turboTDDFT – A code for the simulation of molecular spectra using the Liouville-Lanczos approach to time-dependent density-functional perturbation theory*, Computer Physics Communications. 182 (2011) 1744

[91] Z. Bai, *Templates for the Solution of Algebraic Eigenvalue Problems: A Practical Guide*, SIAM, 2000.

[92] Saad, Y.: *Iterative Methods for Sparse Linear Systms*, 2nd edition (SIAM, philadelphia) (2003)

[93] W. Thomas, Naturwissenschaften 13 (1925) 627.

[94] B. Walker, R. Gebauer, *Ultrasoft pseudopotentials in time-dependent density-functional theory*, The Journal of Chemical Physics. 127 (2007) 164106

[95] D. Vanderbilt, *Soft self-consistent pseudopotentials in a generalized eigenvalue formalism*, Phys. Rev. B. 41 (1990)

[96] http://www.cineca.it/en/content/eurora

[97] E. Cahill, A. Irving, C. Johnson, J. Sexton, *Numerical Stability of Lanczos Methods*, 1999.

[98] M. Marsili, P. Umari, *Method for the fast evaluation of Fock exchange for nonlocalized wave functions*, Phys. Rev. B. 87 (2013) 205110.

[99] S. Nosé, *A unified formulation of the constant temperature molecular dynamics methods*, The Journal of Chemical Physics. 81 (1984) 511

[100] W.G. Hoover, *Canonical dynamics: Equilibrium phase-space distributions*, Phys. Rev. A. 31 (1985) 1695-1697.

[101] A.M.S. Brent Walker, *Efficient approach to time-dependent density-functional perturbation theory for optical spectroscopy*, Physical Review Letters. 96 (2006) 113001.

[102] H.S. Fairman, M.H. Brill, H. Hemmendinger, *How the CIE 1931 color-matching functions were derived from Wright-Guild data*, Color Research & Application. 22 (1997) 11

[103] P. Giannozzi, S. Baroni, N. Bonini, M. Calandra, R. Car, C. Cavazzoni, et al., *QUANTUM ESPRESSO: a modular and open-source software project for quantum simulations of materials*, J. Phys.: Condens. Matter. 21 (2009) 395502.

[104] http://www.quantum-espresso.org

[105] E.E. Koch, *Handbook on synchrotron raidaion*, 1983, Volume 1A, chapter 7

[106] K. Emiko, M. Yoshihiro, N. Yoshinobu, *Conformational Searching and Analysis of Anthocyanins Dyes*, Koryo, Terupen Oyobi Seiyu Kagaku Ni Kansuru Toronkai Koen Yoshishu.

[107] M. Yoshihiro, K. Emiko, N. Yoshinobu, *Molecular Simulation for Exploring the Color Stability of Anthocyanins Dyes*, Nihon Shimyureshon Gakkai Taikai Happyo Ronbunshu. (n.d.).

[108] G. Hundskopf, M. Monica, *Structure and conformation of red radish (Raphanus sativus L.) anthocyanins and their effect on color and pigment stability*

[109] K.S. Lau, A. Mantas, G.A. Chass, F.H. Ferretti, M. Estrada, G. Zamarbide, et al., *Ab initio and DFT conformational analysis of selected flavones: 5,7-dihydroxyflavone (chrysin) and 7,8-dihydroxyflavone*, Can. J. Chem. 80 (2002) 845-855.

[110] T. Schneider, E. Stoll, *Molecular-dynamics study of a three-dimensional one-component model for distortive phase transitions*, Phys. Rev. B. 17 (1978) 1302

[111] M. Petersilka, U.J. Gossmann, E.K.U. Gross, *Excitation Energies from Time-Dependent Density-Functional Theory*, Phys. Rev. Lett. 76 (1996) 1212

[112] H. Appel, E.K.U. Gross, K. Burke, *Excitations in Time-Dependent Density-Functional Theory*, Phys. Rev. Lett. 90 (2003) 043005

[113] T. Fossen, L. Cabrita, O.M. Andersen, *Colour and stability of pure anthocyanins influenced by pH including the alkaline region*, Food Chemistry. 63 (1998) 435-440.

[114] F. Lopes-da-Silva, S. de Pascual-Teresa, J. Rivas-Gonzalo, C. Santos-Buelga, *Identification of anthocyanin pigments in strawberry (cv Camarosa) by LC using DAD and ESI-MS detection*, Eur Food Res Technol. 214 (2002) 248-253.

[115] J. Tomasi, B. Mennucci, R. Cammi, *Quantum mechanical continuum solvation models*, Chem. Rev. 105 (2005) 2999

[116] A. Laio, J. VandeVondele, U. Rothlisberger, *A Hamiltonian electrostatic coupling scheme for hybrid Car-Parrinello molecular dynamics simulations*, The Journal of Chemical Physics. 116 (2002) 6941

[117] L. Ramos, E. Degoli, G. Cantele, S. Ossicini, D. Ninno, J. FurthmÃ¼ller, et al., *Optical absorption spectra of doped and codoped Si nanocrystallites*, Physical Review B. 78 (2008)

[118] A.J. Cohen, P. Mori-Sanchez, W. Yang, *Challenges for density functional theory*, Chem. Rev. 112 (2012) 289.

[119] P.J. Rossky, J.D. Doll, H.L. Friedman, *Brownian dynamics as smart Monte Carlo simulation, The Journal of Chemical Physics.* 69 (1978) 4628

[120] R. Chen, H. Guo, *Effect of spectral range on convergence in Lanczos algorithm*, a numerical study, Chemical Physics Letters. 369 (2003) 650

[121] H.-G. Yu, S.C. Smith, *The calculation of vibrational eigenstates by MINRES filter diagonalization*, Berichte Der Bunsengesellschaft/Physical Chemistry Chemical Physics. 101 (1997) 400

[122] C. Reichardt, *Solvatochromic Dyes as Solvent Polarity Indicators*, Chem. Rev. 94 (1994) 2319

[123] M. Petersilka, U.J. Gossmann, E.K.U. Gross, *Excitation Energies from Time-Dependent Density-Functional Theory*, Phys. Rev. Lett. 76 (1996) 1212.

[124] J.D. Doll, D.R. Dion, *Generalized Langevin equation approach for atom/solid-surface scattering: Numerical techniques for Gaussian generalized Langevin dynamics*, The Journal of Chemical Physics. 65 (1976) 3762

[125] D.L. Ermak, *A computer simulation of charged particles in solution. I. Technique and equilibrium properties*, The Journal of Chemical Physics. 62 (1975) 4189

[126] W. Kohn, L.J. Sham, *Self-Consistent Equations Including Exchange and Correlation Effects*, Phys. Rev. 140 (1965) A1133

[127] M. Yoshihiro, K. Emiko, N. Yoshinobu, *Molecular Simulation for Exploring the Color Stability of Anthocyanins Dyes*, Nihon Shimyureshon Gakkai Taikai Happyo Ronbunshu

[128] A. Dreuw, J.L. Weisman, M. Head-Gordon, *Long-range charge-transfer excited states in time-dependent density functional theory require non-local exchange*, The Journal of Chemical Physics. 119 (2003) 2943

[129] M.E. Tuckerman, D. Marx, M. Parrinello, *The nature and transport mechanism of hydrated hydroxide ions in aqueous solution*, Nature. 417 (2002) 925

[130] T.S. van Erp, E.J. Meijer, *Ab initio molecular dynamics study of aqueous solvation of ethanol and ethylene*, The Journal of Chemical Physics. 118 (2003) 8831.

[131] M. Allesch, F.C. Lightstone, E. Schwegler, G. Galli, *First principles and classical molecular dynamics simulations of solvated benzene*, The Journal of Chemical Physics. 128 (2008) 014501

[132] J. Darias-Martin, M. Carrillo, E. Diaz, R.B. Boulton, *Enhancement of red wine colour by pre-fermentation addition of copigments*, Food Chemistry. 73 (2001) 217.

[133] J. Darias-Martin, B. Martin-Luis, M. Carrillo-Lopez, R. Lamuela-Raventos, C. Diaz-Romero, R. Boulton, *Effect of Caffeic Acid on the Color of Red Wine*, J. Agric. Food Chem. 50 (2002) 2062

[134] M. Born, K. Huang, *Dynamical theory of crystal lattices*, Clarendon press, Oxford University Press, Oxford; New York, 1988.

[135] J. He, *ABSORPTION, EXCRETION, AND TRANSFORMATION OF INDIVIDUAL ANTHOCYANINS IN RATS*, Thesis, 2004

[136] J.B. Harborne, *Phytochemical Methods A Guide to Modern Techniques of Plant Analysis*, Springer, 1998.

[137] A. Mostafazadeh, J. Math. Phys. 43 (2002) 3944

[138] Brouillard, R.; Dubois, J. E. J. Am. Chem. Soc. 1977, 99, 1359.